ELASTODYNAIMC SYSTEMS: ORNITHOPTERS AND POWER HARVESTING

A Dissertation

Presented to the Faculty of the Graduate School

of Cornell University

In Partial Fulfillment of the Requirements for the Degree of

Doctor of Philosophy

by

John Maxfred Dietl

January 2011

ELASTODYNAMIC SYSTEMS: ORNITHOPTERS AND POWER HARVESTING

John Maxfred Dietl, Ph. D.

Cornell University 2011

Ornithopters are air vehicles that fly using flapping wings as lift and propulsion. The study of ornithopter flight dynamics is complicated by time-varying aerodynamics and no dynamic steady state. Using quasi-steady aerodynamics, a Newton-Euler dynamic model of ornithopter flight is utilized to study ornithopter stability and flight dynamics. Floquet analysis is used to analyze these periodic steady flight regimes. This model is then used to analyze and synthesize stabilizing controllers for forward flight and hovering flight. A novel controller is a discrete-time periodic linear quadratic regulator, useful for steady periodic flight dynamics. The model is exploited further to analyze and optimize a nonsteady maneuver: to connect forward flight to hovering flight midflight. Finally, an ornithoptic dirigible is designed and constructed in order to study flapping-wing flight dynamics without requiring the wings to provide lift. The blimp's dynamic modes are observed using a motion capture system. Energy harvesting using cantilevered piezoelectric bimorph vibrators has potential to generate power for long-endurance, low power devices. The geometry of these bimorph vibrators is modeled using Euler-Bernoulli vibration models and the width profile is optimized to produce the highest power transduction. It is found that beams tapering toward the tip are capable of withstanding higher strain, and thus can be subject to stronger vibration at a smaller mass. The Timoshenko model of piezoelectric beam vibration is then derived and compared to the Euler-Bernoulli model and found to be more accurate at higher frequencies and at lower length-to-width ratios.

BIOGRAPHICAL SKETCH

John Dietl was born in Rochester, New York, in 1982. He graduated from Webster High School in Webster, New York, in 2000 and received a Bachelor's of Science in Mechanical Engineering from the University at Buffalo in 2004.

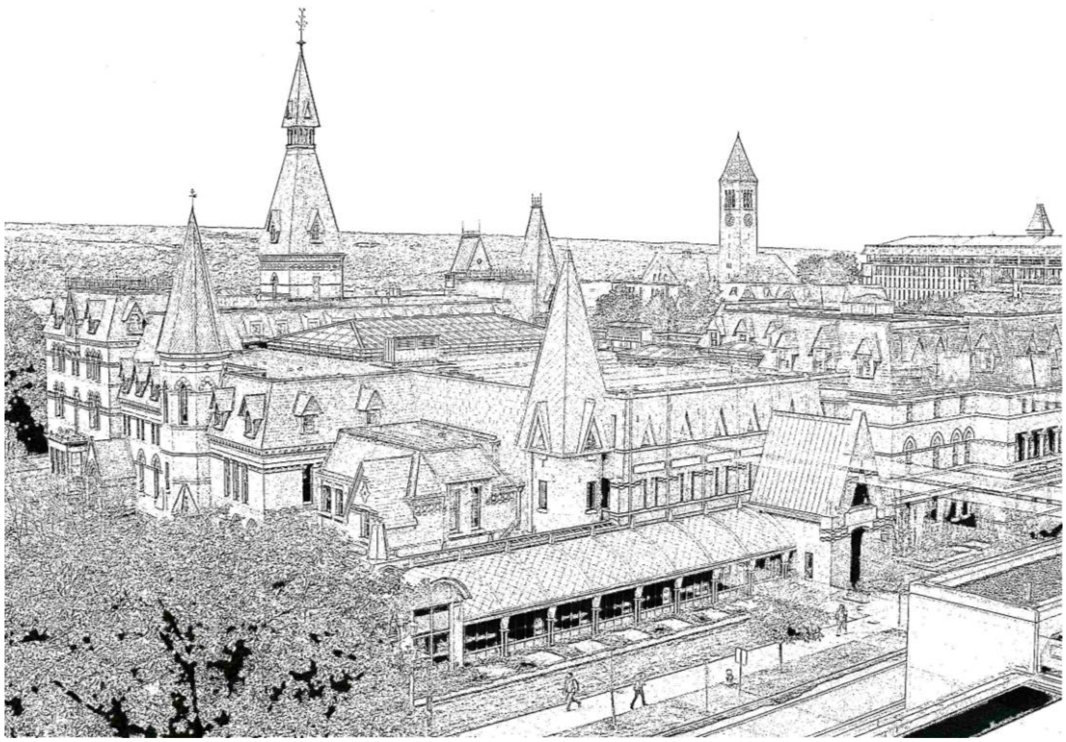

ACKNOWLEDGMENTS

First, I would like to give thanks to my advisor, Prof. Ephrahim Garcia, the architect of so much educational excellence. Second, I would like to thank those fellow graduate students in Prof. Garcia's lab who have helped me throughout my time at Cornell, especially Adam Wickenheiser, Justin Manzo, and Timothy Reissman. I also would like to thank those students who helped directly with my research: Thomas Hermann, Tim Reissman, Eric Wolff, and Adam Wickenheiser. I thank the AFRL at Wright-Patterson Air Force Base for use of its flight test facilities and the assistance of its staff and officers. I acknowledge the financial support from the Sibley School of Mechanical and Aerospace Engineering, the Cornell IGERT Fellowship in Nonlinear Systems (and Prof. Guckenheimer), and the National Defense Science and Engineering Graduate Fellowship. Thanks also to Marcia Sawyer for helping me navigate a confusing graduate school career. Finally, I would like to give my thanks to my parents, who have supported me all these years.

TABLE OF CONTENTS

CHAPTER 5

BEAM SHAPE OPTIMIZATION FOR POWER HARVESTING

CHAPTER 6

A TIMOSHENKO BEAM MODEL FOR CANTILEVERED PIEZOELECTRIC ENERGY HARVESTERS

CHAPTER 7

SUMMARY

LIST OF FIGURES

LIST OF TABLES

CHAPTER 1

STABILITY IN ORNITHOPTER LONGITUDINAL FLIGHT DYNAMICS[1]

1. Introduction

Practical ornithopter designs have long eluded the aerospace engineering profession as engineers have systematically improved performance in other aerodynamic regimes. The design of flapping-wing vehicles has progressed however, leaving a rich history of improvement and imagination. Leonardo da Vinci provided an early impetus to powered flight, misleading engineers for centuries from the simpler fixed wing design that has proven practical. Alphonse Penaud's rubber-band powered model showed the possibility of powered ornithopter construction[1]. After the Wright Brothers' famous flights, ornithopter research was mostly abandoned in favor of the more promising fixed-wing designs. Certain inventors such as Alexander Lippisch and Percival Spencer [1] however continued developing models for manned and unmanned flight. Cox, et al., worked on piezoelectrically actuated ornithopters with novel control schemes [2]. Finally, DeLaurier successfully built a piloted ornithopter and it flew for 14 seconds in 2006 [3].

A major obstacle to these pursuits has been the counterintuitive aerodynamic behavior of air around moving wings. Wagner [4] and Theodorsen [5] provided an early

[1] From Dietl, J. M., and Garcia. E. "Stability in Ornithopter Longitudinal Flight Dynamics," *Journal of Guidance, Control, and Dynamics*, 31(4), July-August 2008, pp 1157-1162; Reprinted with permission of the American Institute of Aeronautics and Astronautics.

mechanism for fixed wings in flutter which has been applied by Jones [6] and DeLaurier [7] to accelerating wings. DeLaurier expanded this to cover the root-flapping wings of an ornithopter. That particular characterization is not difficult to implement for practical computation, and it was compared to actual flapping models with success [7, 8]. Whether these methods, based on potential flow, are applicable for MAV-sized vehicles is undetermined however.

Entomologists and their cohorts working along a different vein have produced aerodynamic models for insect flight. Weis-Fogh and Jensen [9] applied quasi-steady analysis to analyze hovering insects and produced estimates of the lift and drag coefficients of insect wings. Ellington [10] produced a seminal review of insect-flight aerodynamics, mainly using this quasi-steady viewpoint, but with disturbingly high lift coefficients [11]. Computers became sufficiently powerful during the 1990s to allow two-dimensional time-dependent simulation of oscillating airfoils, led by Wang [12] and Russel and Wang [13]. Several 3D approaches have also been attempted, albeit with a deficiency in accuracy requiring excessive computing time [12]. During this same time experiments with mechanical wings have been developed to confirm these computational results for a hawkmoth and a fruit fly [14], providing helpful visualization as well. Finally, Wang et al.[15] provided a quasi-steady approximation to their numerical simulations that will be further outlined in this paper.

The problem this paper addresses is that of designing a flapping-wing micro-air-vehicle: particularly we want to know how it will fly. There exists little literature that provides a practical outline of the ornithopter design process which includes predicting such things as vehicle configuration, power requirements, stress-strain analysis for the wings and internal structures, proper wing kinematics for maneuvering, actuator selection, and control system design. Here we concentrate on dynamically modeling ornithopter flight as a function of selected vehicle geometry, control surface deflections, and wing kinematics. The authors have developed a coupled vehicle dynamics/aerodynamics model for longitudinal flight, which is then used to analyze flight dynamics patterns for predetermined wing kinematics functions, and is used to study trim states for sustained forward flight. Similar to the work of Taylor et al. [16] this work studies the stability of flapping wing vehicles, but not through linear time-invariant dynamics or nonlinear time-periodic equations of motion, but using standard Newtonian dynamics with distributed aerodynamic forces on a set of kinematic linkages.

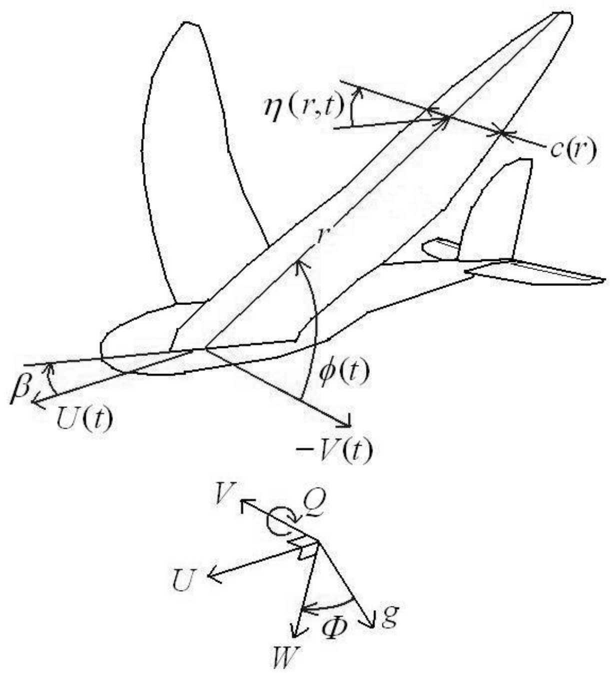

Figure 1.1 - Ornithopter Prototype Schematic. The ornithopter for our study has 2 flapping wings and standard vertical and horizontal stabilizers. The ornithopter simulated by the authors has a wingspan of 0.72 *m*. The vehicle's mass of 0.12 *kg*, with each wing 0.0079 *kg*.

2. Modeling

To design ornithopter features to provide enough lift to overcome weight and to produce enough thrust to overcome drag, the authors have modeled a standard ornithopter configuration consisting of a fuselage, a pair of symmetric wings, and a standard airplane empennage (Figure 1.1). The empennage contains control authority over the rudder and elevator, but there are no ailerons on the wings (the longitudinal assumption makes this moot, but this will be more significant with further analyses, as DeLaurier's ornithopter relies on yaw-roll coupling in place of ailerons).

The wings are attached to the fuselage via a hinged joint, allowing two rotational degrees of freedom (Figure 1.1). The first, and most prominent, is the vertical plunging (or heaving) of the wings $\phi(t)$. This is the characteristic oscillating dihedral motion of avian forward flight, requiring the most energy of all the controlled motions. All other kinematics on the ornithopter are referred to this oscillatory motion and its phase. The second degree of freedom is a wing twist about the quarter-chord line $\eta(r,t)$. It is noted in the literature that this oscillating motion is approximately 90° out of phase from plunging [7]. These motions are given as follows:

$$\phi(t) = C_h \cos(\omega\, t) + \phi_0 \tag{1}$$

$$\eta(r,t) = C_t \frac{r}{R} \cos\left(\omega\ t + \phi_{\eta_0}\right) \tag{2}$$

where ω is in rad/sec. Realistic wing structures for flapping flight are flexible and respond aeroelastically to the fluid forces and to their own inertial loads. In birds this is quite dramatic as the feathers perform gross shape change due to their flexibility and the supporting structure's flexibility. Our ornithopter wing model assumes that the wings are rigid except for predefined twisting and plunging angles.

Fluid dynamics around the vehicle are a different issue. As mentioned earlier, full computational fluid dynamic simulations of the time-dependent three-dimensional Navier-Stokes equations is not practical for vehicle dynamics simulation. Impracticalities include unknown fluid initial conditions and boundary conditions, unknown required resolution to realize the salient features of the flow, and of course the enormous scaling difficulties with three-dimensional flow field discretization. Thus, simplifications are in order. Since two-dimensional CFD simulations have shown veracity to robotic flapping experiments [14], the authors have adopted calculations relying on wing sections rather than the entire wing. This is similar to the methods of DeLaurier [7] for larger models. This must be further simplified however if computations are to be rapid enough to enable the analysis of vehicle dynamics. A set of algebraic formulas for forces on an airfoil, designed to match the general behavior of the 2D CFD results, are thus employed as derived by Wang et al. [15]. This method sacrifices precision for computability, but this is warranted by our application: generation and analysis of ornithopter flight trajectories.

Force formulas are derived from three main modes: circulation, added mass, and viscous drag. Circulation for flapping wings is approximated as such (from Andersen et. al. [17]):

$$\Gamma(r) = -2C_L c(r)\frac{uv}{|\boldsymbol{v}|} + 2C_R c(r)^2 \dot{\eta} \tag{3}$$

The first of the two terms is the translation-induced circulation, the general mechanism for lift generation in fixed-wing aircraft. The second term, absent from standard fixed-wing aircraft aerodynamics, depends on rotation rate, and is derived from the lift on a zero angle-of-attack pitching plate [17].

Added mass is a term that compensates for the acceleration of the mass of the air near the airfoil, an effective additional inertial load affecting the total force on the wing. Had this been a time-dependent simulation of the Navier-Stokes equations, this term would not exist as a separate term but would be embedded in the momentum of the general fluid motion. Quasi-steady approximations, however, require corrections to adhere to the true unsteady flow patterns.

Finally, the viscous drag force is the most intuitive force among these outlined here. It estimates the effect of the viscous boundary layer, but also separated pressure-driven drag:

$$d\boldsymbol{F}_v = \rho r c(r)|\boldsymbol{v}|\left\{C_D(0)\cos^2\alpha + C_D(\pi/2)\sin^2\alpha\right\}dr\begin{bmatrix} u \\ v \end{bmatrix} \tag{4}$$

Wang[11] gives the forces on the airfoil as these:

$$dF_x = \left\{\left(\frac{m_w c(r)}{\bar{c}} + m_{22}\right)\frac{r}{R}v\dot{\eta} - \rho r v\Gamma - m_{11}\frac{r}{R}\dot{u}\right\}dr - dF_{v_x} \tag{5}$$

$$dF_y = \left\{-\left(\frac{m_w c(r)}{\bar{c}} + m_{11}\right)\frac{r}{R}u\dot{\eta} + \rho r u\Gamma - m_{22}\frac{r}{R}\dot{v}\right\}dr - dF_{v_y} \tag{6}$$

$$d\tau = \left\{(m_{11} - m_{22})\frac{r}{R}vu - \frac{I_a}{R}\ddot{\eta} + \frac{c(r)}{4}\rho v\Gamma\right\}dr - d\tau_v \tag{7}$$

These equations can then be compared with those of DeLaurier [7] in simulation thus providing confidence in their correlation to larger scale aircraft; at the intermediary between insect flight and a human-piloted ornithopter the models largely agree. The simulation is run with a given set of sinusoidal wing kinematics and a given steady air velocity and the resulting total lift is shown in Figure 1.2. In this instance, the force equations act on the ornithopter whose fuselage is constrained rigidly in space as though it we resting on a sting in a wind tunnel.

The differences in the simulated results arise from the differences in modeling assumptions between the two methods. Wang's model, used herein, approximates the vortex shedding effects through empirical matching of a series of force coefficients. These originate in the study of unsteady flow features such as leading-edge vortex and spanwise flow which are found in insect wings. DeLaurier's model uses classical theoretical aerodynamics developed within the regime of piloted aircraft. It accounts for the unsteady vortex effects of flapping through Theodorsen functions, a result of applied potential theory to unsteady wing motions [6]. Opposed to Wang's insect motivated corrections, this uses the long studied aerodynamics of conventional aircraft and aeroelastic wings. In the actual calculations of forces from these models, however, many of the terms appear the same; there are components proportional to wing velocity, rotation rate, translational acceleration, and rotational acceleration in both.

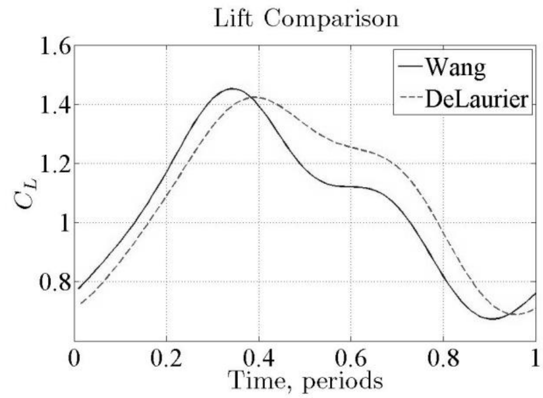

Figure 1.2 - Wang's method vs. Delaurier's method.

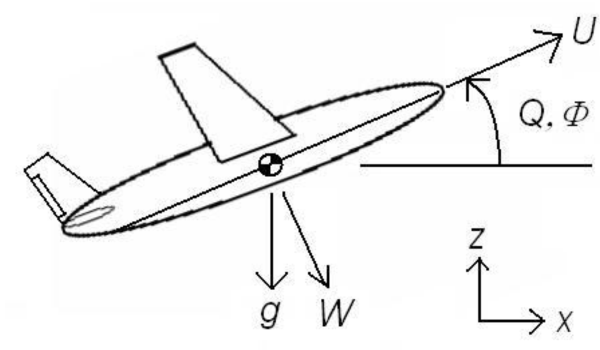

Figure 1.3 - Schematic of dynamic variables in the longitudinal plane.

Ornithopter trajectories are governed by the Newton-Euler equations of rigid body motion in the local frame:

$$\boldsymbol{F} = m\left.\frac{d\boldsymbol{v}_c}{dt}\right|_B + m(\boldsymbol{\omega}\times\boldsymbol{v}_c) \tag{8}$$

$$\boldsymbol{M} = \left.\frac{d\boldsymbol{H}}{dt}\right|_B + \boldsymbol{\omega}\times\boldsymbol{H} \tag{9}$$

The equations are simplified for longitudinal motion here:

$$\dot{U} = -QW - g\sin\Phi + F_x/m \tag{10}$$

$$\dot{W} = QU + g\cos\Phi + F_z/m \tag{11}$$

$$\dot{Q} = M_y/I_y \tag{12}$$

$$\dot{\Phi} = Q \tag{13}$$

$$\dot{x} = U\cos\Phi + W\sin\Phi \tag{14}$$

$$\dot{z} = U\sin\Phi - W\cos\Phi \tag{15}$$

where U, W, Q, and Φ are illustrated in Figure 1.3, and F_x, F_z, and M_y, include all aerodynamic forces and moments in the body frame of reference. These coordinates can be normalized using the following parameters: a characteristic length $l_0 = 2m/\rho S$, a characteristic velocity $V_0 = \sqrt{gl_0}$, a characteristic time $t_0 = \sqrt{l_0/g}$, and a characteristic rotation rate $\omega_0 = 2\pi/t_0$. These parameters are chosen due to their independence from kinematic variables like flapping frequency or amplitude. These expressions combined with the above aerodynamic formulas are easily implemented in software for simulation under given input kinematics (Figure 1.1). The authors use MATLAB [18] exclusively, as in previous work [19].

3. Trim Analysis

We want to find the trim state of the ornithopter as a function of its elevator angle, wing twist amplitude, plunging amplitude, and flapping frequency. Unfortunately, for ornithopters there is no state where U, W, Q, and Φ are constant in time, the usual definition of trim for a fixed-wing aircraft. Forces on an ornithopter can be periodic however, so we define ornithopter trim as a limit cycle with the same frequency as the flapping input.

A limit cycle [20] $\boldsymbol{x}^*(t)$ of a dynamic system (16) is an isolated periodic solution of the system's equations of motion:

$$\dot{\boldsymbol{x}} = \boldsymbol{f}(\boldsymbol{x}), \ \boldsymbol{x} \in R^n \tag{16}$$

$$\boldsymbol{x}(t+T) = \boldsymbol{x}(t), \ \forall t \tag{17}$$

Limit cycles are invariant; any trajectory starting on a limit cycle remains there for all time. Also, limit cycles are generally stable or unstable; trajectories starting near a limit cycle either approach the limit cycle trajectory or diverge from it. The typical method to quantify the stability of a limit cycle is to analyze the Poincaré map, a mapping of the intersection of the trajectory with a hyperplane transverse to the limit cycle:

$$\boldsymbol{x}(k+1) = P(\boldsymbol{x}(k)) \tag{18}$$

Selection of such a plane is not unique; the plane can intersect the limit cycle anywhere along the trajectory. Thus $\boldsymbol{x}(k)$ and $\boldsymbol{x}(t)$ represent the same state, but $\boldsymbol{x}(k)$ only occurs at discrete instants in time. In this mapping, a point near the limit cycle will map to another point on the hyperplane, and the point where the limit cycle intersects the plane is an equilibrium point $\boldsymbol{x}^*(k)$ in discrete time:

$$\mathbf{x}^*(k+1) = P(\mathbf{x}(k)) = \mathbf{x}^*(k) \tag{19}$$

and thus can be analyzed for stability. The Jacobian of the Poincaré map taken at the equilibrium is called the monodromy matrix, and its eigenvalues, called the Floquet multipliers, determine the linear stability of the limit cycle. Indeed, the monodromy matrix is the discrete-time state matrix in the linearization of the Poincaré map:

$$\{\boldsymbol{x}(k+1) - \boldsymbol{x}^*(k+1)\} = M\{\boldsymbol{x}(k) - \boldsymbol{x}^*(k)\} \tag{20}$$

The Floquet multipliers have interesting properties: 1.) they are independent of the hyperplane choice for the Poincaré map, since they are a property of the limit cycle, 2.) at least one Floquet multiplier, called the trivial multiplier, is identically 1. Notably, the eigenvector associated with the trivial multiplier points along the limit cycle trajectory. A limit cycle is stable if all its Floquet multipliers, save the trivial multiplier, have complex modulus less than 1.

The periodically-forced ornithopter system can be seen as an autonomous system if a set of differential equations can be found that integrate to the required forcing functions. The forcing functions are augmented to the state vector of the system and treated as dynamic states. Since for our ornithopter, the flapping is governed by sinusoids, finding their differential equations is trivial; they are a linear combination of sines and cosines in the form $\ddot{x} + \omega^2 x = 0$. Interestingly, the resulting monodromy matrix for the forced ornithopter system is in block form so the trivial multipliers associated with the forcing can be ignored in stability calculations. The block containing the interesting system properties, which is the block illustrated below, thus will not contain the trivial multiplier.

The monodromy matrix can be calculated from an initial value problem. The nonlinear system can be linearized about the limit cycle and a state transition matrix can be calculated as follows. Then the linearized system is:

$$\frac{d\{\boldsymbol{x}(t)-\boldsymbol{x}^*(t)\}}{dt}=\left[\left.\frac{\partial \boldsymbol{f}(\boldsymbol{x})}{\partial \boldsymbol{x}}\right|_{\boldsymbol{x}=\boldsymbol{x}^*(t)}\right]\{\boldsymbol{x}(t)-\boldsymbol{x}^*(t)\} \tag{21}$$

The solution to this linear time-varying ordinary differential equation is:

$$\{\mathbf{x}(t)-\mathbf{x}^*(t)\}=\mathbf{\Phi}(t,t_0)\{\mathbf{x}(t_0)-\mathbf{x}^*(t_0)\} \tag{22}$$

where $\boldsymbol{\Phi}(t,t_0)$ is the state transition matrix, the solution of the differential equation:

$$\frac{d\mathbf{\Phi}(t,t_0)}{dt}=\left[\left.\frac{\partial \mathbf{f}(\mathbf{x})}{\partial \mathbf{x}}\right|_{\mathbf{x}=\mathbf{x}^*(t)}\right]\mathbf{\Phi}(t,t_0),\ \mathbf{\Phi}(t_0,t_0)=I \tag{23}$$

If $(t-t_0)$ equals the period of flapping, then the state transition matrix equals the monodromy matrix. Thus the monodromy matrix can be calculated through numerical integration of this initial value problem. The challenge is to calculate the limit-cycle trajectory and its Jacobian. State transition matrices have the semi-group property:

$$\boldsymbol{\Phi}(t_2,t_0)=\boldsymbol{\Phi}(t_2,t_1)\boldsymbol{\Phi}(t_1,t_0) \tag{24}$$

which allows the monodromy matrix to be expressed as a product of state transition matrices of the system around subsections of the limit cycle. This becomes valuable for the multiple-shooting method described here.

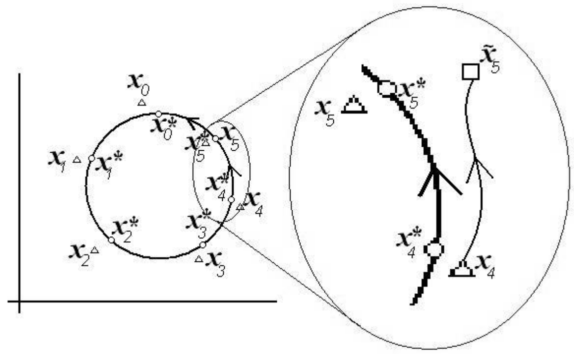

Figure 1.4 - Schematic of multiple shooting algorithm. Points in state space are guessed, and the equations of motion are integrated from each guess to the next point in time.

The limit cycle is broken into a series of segments (Figure 1.4) in time delineated by a set of time points and coordinates [21]:

$$0 < t_1 < t_2 < \cdots < t_{m-1} < T \tag{25}$$

$$\{\boldsymbol{x}(0), \boldsymbol{x}(t_1), \ldots, \boldsymbol{x}(t_{m-1}), \boldsymbol{x}(t_m)\} = \{\boldsymbol{x}_0, \boldsymbol{x}_1, \ldots, \boldsymbol{x}_{m-1}, \boldsymbol{x}_m\} \tag{26}$$

and let the numerical solution of the dynamic system between time points be denoted as

$$\{\tilde{\boldsymbol{x}}_1, \tilde{\boldsymbol{x}}_2, \ldots, \tilde{\boldsymbol{x}}_{m-1}, \tilde{\boldsymbol{x}}_m\} \tag{27}$$

then the periodicity of the limit cycle is enforced by the system of equations,

$$\begin{cases} \tilde{\mathbf{x}}_1 - \mathbf{x}_1 = 0 \\ \tilde{\mathbf{x}}_2 - \mathbf{x}_2 = 0 \\ \quad\vdots \\ \tilde{\mathbf{x}}_m - \mathbf{x}_m = 0 \\ \mathbf{x}_m - \mathbf{x}_0 = 0 \end{cases} \tag{28}$$

which are satisfied when $\mathbf{x}_i = \mathbf{x}_i^*$ and these equations can be solved using Newton's method. Knowing that the integrated trajectory termini $\tilde{\mathbf{x}}_i$ depend on the guess of the initial condition $\mathbf{x}_{i-1}$ only, and the guesses $\mathbf{x}_i$ depend only on themselves, the iterated equations become:

$$\begin{bmatrix} \frac{\partial \tilde{\mathbf{x}}_1}{\partial \mathbf{x}_0}, & -I, & 0, & \cdots & 0, & 0 \\ 0, & \frac{\partial \tilde{\mathbf{x}}_2}{\partial \mathbf{x}_1}, & -I, & \cdots & 0, & 0 \\ \vdots & \vdots & \vdots & \ddots & \vdots & \vdots \\ 0, & 0, & 0, & \cdots & \frac{\partial \tilde{\mathbf{x}}_m}{\partial \tilde{\mathbf{x}}_{m-1}}, & -I \\ -I, & 0, & 0, & \cdots & 0, & I \end{bmatrix} \begin{bmatrix} \Delta \mathbf{x}_0 \\ \Delta \mathbf{x}_1 \\ \Delta \mathbf{x}_2 \\ \vdots \\ \Delta \mathbf{x}_{m-1} \\ \Delta \mathbf{x}_m \end{bmatrix} = -\begin{bmatrix} \tilde{\mathbf{x}}_1 - \mathbf{x}_1 \\ \tilde{\mathbf{x}}_2 - \mathbf{x}_2 \\ \vdots \\ \tilde{\mathbf{x}}_m - \mathbf{x}_m \\ \mathbf{x}_m - \mathbf{x}_0 \end{bmatrix} \tag{29}$$

where the Jacobians $\frac{\partial \tilde{\mathbf{x}}_i}{\partial \mathbf{x}_{i-1}}$ are the state transition matrices $\mathbf{\Phi}(t_{i-1},t_i)=M(i-1)$, calculated about the guessed trajectories. When the guessed trajectories are correct, they connect to form the limit cycle and the Jacobians can combine to form the state transition matrix for the entire circuit:

$$\mathbf{\Phi}(t_m, t_{m-1})\mathbf{\Phi}(t_{m-1}, t_{m-2})\cdots\mathbf{\Phi}(t_2, t_1)\mathbf{\Phi}(t_1, t_0) = \mathbf{\Phi}(t_m, t_0) = M \tag{30}$$

where M is the aforementioned monodromy matrix for the circuit. Also note that monodromy matrices for each point calculated in the multiple-shooting algorithm can as easily be calculated by changing the order of multiplication. Thus we have produced a method for linearizing and analyzing the system's internal dynamics, but the next step is to study the effect of parameter changes on those dynamics.

General nonlinear systems of the form (31) can be linearized around a nominal control input $\mathbf{u}$ at any time step (as in Eq. (32)):

$$\dot{\mathbf{x}} = \mathbf{f}(\mathbf{x}, \mathbf{u}) \tag{31}$$

$$\mathbf{x}(k+1) = M(k)\mathbf{x}(k) + G(k)\mathbf{u}(k) \tag{32}$$

where $G(k) = \tilde{G}(t_{k+1})$, the input matrix, is the solution to this initial value problem:

$$\frac{d\tilde{G}(t)}{dt} = \left[\left. \frac{\partial \mathbf{f}(t, \mathbf{x}, \mathbf{u})}{\partial \mathbf{x}} \right|_{\mathbf{x}(t), \mathbf{u}(t)} \right] \tilde{G}(t) + \left[\left. \frac{\partial \mathbf{f}(t, \mathbf{x}, \mathbf{u})}{\partial \mathbf{u}} \right|_{\mathbf{x}(t), \mathbf{u}(t)} \right], \tilde{G}(t_k) = 0 \tag{33}$$

which can be solved numerically, and $\tilde{G}(t)$ is a dummy integration variable. (Or if in discrete-time $\mathbf{x}(k+1) = \mathbf{f}\{\mathbf{x}(k), \mathbf{u}(k)\}$ then $G(k) = \partial \mathbf{f}\{\mathbf{x}(k), \mathbf{u}(k)\} / \partial \mathbf{u}(k)$.) What this means is that the general nonlinear controlled system (31) can be analyzed using the tools of control theory for linear discrete-time systems. Of particular interest is to apply that theory to design a feedback controller to stabilize the system; that is to create a rule for parameter changes that makes the system stable. The additional property of periodicity in the trajectory is advantageous; the input matrices become periodic:

$$G(k+m) = G(k) \tag{34}$$

and all controller algorithms can be computed a priori.

Another challenge is calculation of the Jacobians $\left. \frac{\partial \boldsymbol{f}(t, \boldsymbol{x}, \boldsymbol{u})}{\partial \boldsymbol{x}} \right|_{\boldsymbol{x}(t), \boldsymbol{u}(t)}$ and $\left. \frac{\partial \boldsymbol{f}(t, \boldsymbol{x}, \boldsymbol{u})}{\partial \boldsymbol{u}} \right|_{\boldsymbol{x}(t), \boldsymbol{u}(t)}$. The underlying equations are difficult to write out, and the symbolic rendition of their derivatives is practically impossible to set down. One solution to this is to use finite-difference differentiation, but this operation's error is unknown. An alternative is automatic differentiation, a method that computes derivatives of a function while the function's value is computed. One particular implementation for MATLAB, ADMAT [22], creates a new class of variable with 2 components: the functional value and its derivative. As MATLAB runs through the order of operations upon the first component, a running derivative for each operation is computed and combined into the second component using a table of derivatives for each basic MATLAB function and the chain rule of differentiation. This produces derivative values to machine precision. For example, if given this function:

$$f(x) = x\sin(\omega x + \phi), \tag{35}$$

the order of operations would be as in Table 1.1. Thus automatic differentiation calculates the derivative simultaneously with the function value.

Table 1.1. Automatic differentiation example

Operation Number	Function	Derivative
1	$x_1 = \omega * x + \varphi$	$x_1' = \omega$
2	$x_2 = \sin(x_1)$	$x_2' = x_1' * \cos x_1$
3	$x_3 = x * x_2$	$x_3' = x_2 + x * x_2'$
4	$f(x) = x_3$	$df(x)/dx = x_3'$

4. Dynamic Analysis on an Ornithopter

Using the above methodologies we will now analyze the flight dynamics of an ornithopter. Through trial and error, several limit cycles were found in these analyses, with one eventually selected for further analysis. The same limit cycle will be used in the following control design section to produce a stable trim for ornithopter flight. The first item of interest is the convergence of the multiple shooting algorithm outlined in Eqs. (25-29). Figure 1.5 shows, that for this example, the Newton method converges quadratically in as few as 4 iterations, to produce a precise list of points on the limit cycle. Other examples show similar convergence rates, depending on the initial condition.

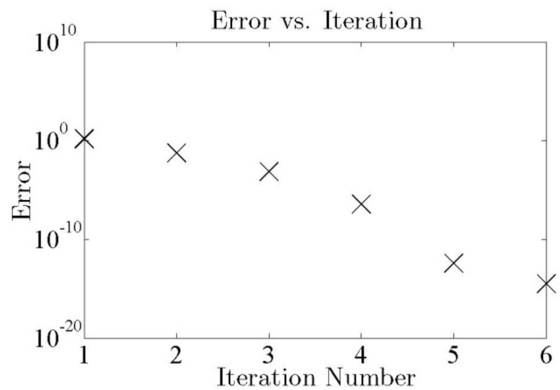

Figure 1.5 - Multiple shooting convergence. The error is defined as the 2-norm of the right side of Eq. (27).

The limit cycle illustrated here (Figure 1.6) is the example used here for stability analysis and control design. It represents a near straight and level trajectory (Figure 1.7). The monodromy matrix for this limit cycle, as calculated using Eq. (30), is:

$$M = \begin{bmatrix} 1.0565 & -0.16208 & -0.29621 & -2.0939 \\ -0.37531 & 0.33912 & 0.63510 & 0.34042 \\ -0.34225 & 0.55420 & 1.1198 & 0.15016 \\ -0.039648 & 0.079971 & 0.20947 & 1.0105 \end{bmatrix} \tag{36}$$

where its discrete-time eigenvalues are

$$\lambda = 1.9782,\ 0.014836,\ 0.76642 \pm 0.36764i \tag{37}$$

hence the system is unstable (Figure 1.8).

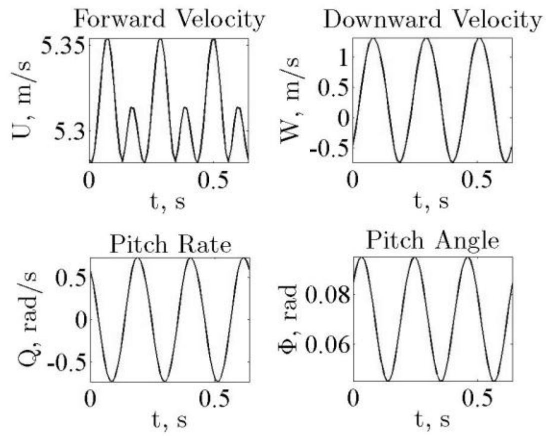

Figure 1.6 - Limit cycle illustration.

a)

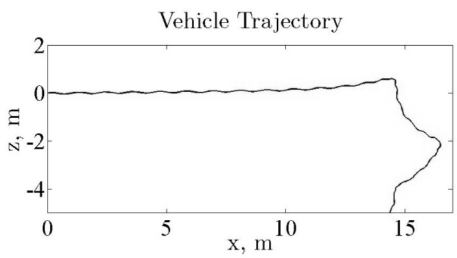

b)

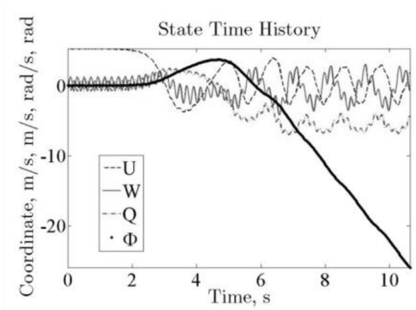

Figure 1.7 - a) Flight trajectory in limit cycle. b) State trajectories during the same flight. Note the trajectory diverges after 2*s*. At that time, the vehicle pitches up, *U* drops drastically, and 2.5*s* later, the vehicle begins a downward pitching tumble (as indicated by the pitch angle).

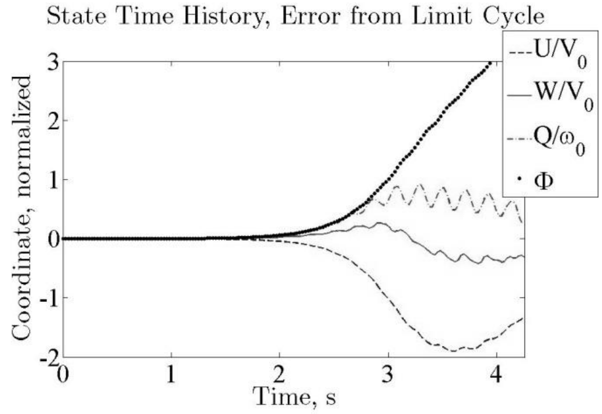

Figure 1.8 - Error dynamics for a slightly perturbed unstable ornithopter. The velocity coordinates are normalized by the characteristic velocity V_0, and the pitch rate is normalized by the characteristic rotation rate ω_0. The pitch angle is already dimensionless.

Figure 1.6 presents the dynamic states of the ornithopter during 3 periods of one limit cycle. These are the trim values for each state, from which the unstable system would diverge. Figures 7 and 8 are results from one simulation: Figure 1.7a shows the longitudinal trajectory of the ornithopter in free flight and Figure 1.7b shows the values of the states during the flight. Figure 1.8 shows the deviation of the ornithopter's dynamic states from their trim values on the limit cycle as the ornithopter diverges. The ornithopter pitches up near the 2*s* mark, enters a pitching tumble, and the vehicle begins to dive. This is all caused by the instability in the system, which is addressed in the next section using feedback control.

Modal analysis provides further illustration of the system. The unstable eigenvalue $\lambda_1 = 1.9782$ has the eigenvector $v_1 = [-0.68, 0.42, 0.57, 0.19]^T$, meaning that this mode excites all the states with a similar magnitude. The stable real eigenvalue $\lambda_2 = 0.014844$ has the eigenvector $v_2 = [0.060, 0.90, -0.43, 0.022]^T$, which has a disproportionate effect on W and Q, similar to the short period mode without oscillation. It has a time constant of 0.0505*s*. Finally the stable complex eigenvalues $\lambda_{3,4} = 0.76644 \pm 0.36764i$ has eigenvectors $v_{3,4} = [0.83, 0.067 \pm 0.17i, 0.43 \pm 0.25i, 0.052 \mp 0.19i]^T$, having a disproportionate effect on U and Q, which is similar to a traditional Phugoid mode with a damping ratio of 0.34 and a natural frequency of 2.16 *rad/s*. The settling time for this mode ($t_s = 4/\zeta\omega_n$) is 5.42*s*.

5. Conclusion

We have constructed equations of motion for an ornithopter with a periodic wing motions but with no periodicity explicitly included in the vehicle states. The aerodynamics is a function of the vehicle states, and the states themselves are governed by nonlinear differential equations. Unlike nonlinear time periodic models, the root solving method discovered a periodic motion in the ornithopter's states without a priori estimates of the vehicle's trim velocities, or even proof of their existence.

Limit cycles are merely a feature of the phase space in ornithopter flight dynamics that need to be found, but when found herald powerful implications. First, they represent the only analog to a dynamic equilibrium in this nonautonomous system; with flapping wings there is no constant force and only a trivial case would maintain constant states in the system. Second, limit cycles are well understood in the theory of nonlinear dynamics and their properties describe much about the surrounding phase space such as domains of attraction. Third, finding numerical approximation of the limit cycles to computer precision allows for a study of the system's stability with the same precision as calculating the eigenvalues of the jacobian of an equilibrium point. Thus, in this analysis the estimation of the system’s eigenvalues is independent of the flapping frequency and amplitude, which figure largely in averaging methods. The least precise part of the dynamic analysis is now the aerodynamic model.

This sets a foundation for linear discrete-time regulation of ornithopter flight without resorting to averaging methods, while the discrete-time system is amenable to computer manipulation. Additionally, the Floquet algorithm provides a starting point for continuation methods to find other trim points. This will allow engineers to estimate the flight envelope of proposed ornithopter designs and to compare with other available technologies. In addition, it can help evaluate performance, efficiency, and maneuverability. More development is still required to attain these ends, but the present analysis is a starting point for calculating ornithopter performance. Future possibilities are to use this methodology as a basis to solve for optimal kinematics for low-power trajectories, high-speed trajectories, and unsteady maneuvers such as takeoff, landing, and lateral movements.

REFERENCES

[1] DeLaurier, J. D., and Harris, J. M., “A Study of Mechanical Flapping-Wing Flight,” *Aeronautical Journal*, Vol. 97, Oct. 1993, pp. 277-286.

[2] Cox, A., Monopoli, D., Cveticanin, D., Goldfarb, M., and Garcia, E., “The Development of Elastodynamic Components for Piezoelectrically Actuated Flapping Micro-Air Vehicles,” *Journal of Intelligent Material Systems and Structures*, Vol. 13, No. 9, 2002, pp. 611-615.

[3] Black, D., “It Flies! Aviation History is Made by the ‘Flapper’,” *Toronto Star*, 9 July 2006, pp. A03.

[4] Wagner, H., “Über die Entstehung des dynamischen Auftriebes von Tragflügein,” Z. f. a. M. M., Bd. 5, Heft 1 Feb. 1925, S. 17-35.

[5] Theodorsen, T., “General Theory of Aerodynamic Instability and the Mechanism of Flutter,” NACA Technical Report No. 496, 1935.

[6] Jones, R. T., “The Unsteady Lift of a Wing of Finite Aspect Ratio,” NACA Technical Report No. 681, 1940.

[7] DeLaurier, J. D., “An Aerodynamic Model for Flapping-Wing Flight,” *Aeronautical Journal*, April, 1993, pp. 125-130.

[8] DeLaurier, J. D., “The Development and Testing of an Efficient Ornithopter Wing,” *Aeronautical Journal*, May 1993, pp. 153-162.

[9] Weis-Fogh, T., and Jensen, M., “Biology and Physics of Locust Flight: I. Basic Principles in Insect Flight. a Critical Review,” *Proceedings of the Royal Society B,*. Vol. 239, 1956, pp. 415-458.

[10] Ellington, C. P., “The Aerodynamics of Hovering Insect Flight” *Philosophical Transactions of the Royal Society B.* Vol. 305, 1984, pp. 1-181.

[11] Wang, Z. J., “Dissecting Insect Flight,” *Annual Review of Fluid Mechanics,* Vol. 37, 2005, pp. 183-210.

[12] Wang, Z. J., “Two Dimensional Mechanism for Insect Hovering” , *Physical Review Letters*, Vol. 85, No. 10, 2000, pp. 2216-2219.

[13] Russell, D., and Wang, Z. J., “A Cartesian Grid Method for Modeling Multiple Moving Irregular Objects in 2D Incompressible Viscous Flow” *Journal of Computational Physics*, Vol. 191, No. 1, 2003, pp. 177-205.

[14] Dickinson, M. H., Lehmann, F. O., and Sane S. P., “Wing rotation and the aerodynamic basis of insect flight” *Science,* Vol. 284, No. 5422, 1999, pp. 1954-1960.

[15] Wang, Z.J., Birch, J., and Dickinson, M., "Unsteady Forces and Vorticity Field in Hovering Flight: Two Dimensional Computations vs Robotic Wing Experiments", *Journal of Experimental Biology*, Vol. 207, No. 3, 2004, pp. 449-460.

[16] Taylor, G. K., Bomphrey, R. J., and Hoen, J., “Insect Flight Dynamics and Control,” *44th AIAA Aerospace Sciences Meeting and Exhibit*, AIAA 2006-32, AIAA, January 9-12, 2006, Reno, NV, USA.

[17] Andersen, A., Pesavento, U., and Wang, Z.J., “Analysis of Transitions Between Fluttering, Tumbling and Steady Descent of Falling Cards,” *Journal of Fluid Mechanics*, Vol. 541, 2005, pp. 91-104.

[18] MATLAB, Software Package, Ver. 7.2.0.232, Copyright 1984-2007, The MathWorks, Inc.

[19] Dietl, J. M., and Garcia, E., "Kinematic Variation and Modeling for Design in Ornithoptic Flight", *ASME International Mechanical Engineering Congress and Exposition*, IMECE2005-82035, ASME, November 5-11, 2005, Orlando, FL, USA.

[20] Strogatz, S. H., *Nonlinear Dynamics and Chaos: With Applicatioins to Physics, Biology, Chemistry, and Engineering*, Westview Press-Perseus Books Publishing, Cambridge, MA, 1994, Chaps. 7-8.

[21] Lust, K., "Improved Numerical Floquet Multipliers," *International Journal of Bifurcation and Chaos,* Vol. 11, No. 9, 2000, pp. 2389-2410.

[22] Coleman, T. F., and Verma, A., "ADMIT-1: Automatic Differentiation and MATLAB Interface Toolbox," *ACM Transactions on Mathematical Software*, Vol. 26, No. 1, 2000, pp. 150-175.

This chapter originally appeared as:

Dietl, J. M., and Garcia. E. "Stability in Ornithopter Longitudinal Flight Dynamics," *Journal of Guidance, Control, and Dynamics*, 31(4), July-August 2008, pp 1157-1162.

CHAPTER 2

ORNITHOPTER CONTROL WITH PERIODIC INFINITE HORIZON CONTROLLERS[1]

1. Abstract

Ornithopters, unmanned-air-vehicles flying using flapping wings to generate thrust, are analyzed for forward flight and hovering trajectories. The authors have used Newton's method to generate the desired trajectories with a multiple-shooting parameterization of the periodic flight conditions inherent in flapping flight. The resulting trajectories are analyzed for stability, and linearized models of the dynamics are generated for control design. Several controllers are tested, all of which were capable of stabilizing the unstable limit cycles of ornithopter flight. Among these controllers are: proportional-derivative controller; continuous-time state feedback linear quadratic regulator; state feedback periodic, discrete-time, time-varying, linear quadratic regulator; and sensor feedback, periodic, discrete-time, time-varying linear quadratic Gaussian regulator.

2. Introduction

In this time of increased need for unmanned air vehicles with new capabilities for intelligence, surveillance, and reconnaissance, ornithopter flight presents an appealing design strategy. However, the nonlinear dynamics and 4-dimensional aerodynamics of

[1] From Dietl, J. M. and Garcia, E., "Ornithopter Control with Periodic Infinite Horizon Controllers," (In Preparation)

ornithopter flight have long vexed researchers. Until recently, ornithopter research has concentrated on vehicle design, aerodynamics, and flight control, each of which is a necessary but insufficient basis for vehicle design and operation.

Since antiquity, engineers and enthusiasts have designed flapping-wing air vehicles [1], but only recently have these designs approached practical value. DeLaurier's *Mentor* project [2] and piloted ornithopter [3] projects have proven fruitful in their design objectives: *Mentor'*s, to create a hover-capable micro air vehicle, the piloted ornithopter's, to create a ornithopter capable of carrying a person. Neither serves the ISR objective optimally, however, where the vehicle requires long endurance, bio-mimicry, and extreme maneuverability. *Mentor* used clap-fling aerodynamics to produce the thrust required to balance its weight, as do certain hovering insects, but this proved costly in energy and in power consumption. Cox et al [4] designed a piezoelectric-actuated ornithopter that, although incapable of producing enough lift for hover, showed the importance of tuning the wings' natural frequencies of vibration with the flapping frequency. Avadhanula et al. [5] developed a wing-flapping mechanism for an insect-like wing, capable of lifting a 100 mg machine. In addition, researchers have been using computational design strategies—specifically genetic programming—to design ornithopters with passive stability [6-8].

Flapping wing aerodynamics arose in the 1920s to combat the problem of wing flutter in fixed-wing aircraft. Theodorsen [9] and Jones [10] provided a theoretical basis for the later work of DeLaurier [11] regarding his piloted (manned) ornithopter project. Another thread in the flapping-wing aerodynamics field came from studies of insect flight, at much lower Reynolds numbers than that of the fluttering-wing aircraft studied by NACA. Researchers such as Weis-Foch [12], Ellington [13], Dickinson et al. [14], and Wang [15] developed a coherent quasi-steady analysis of flapping flight aerodynamics, which later proved useful for simulation and control design [16]. Weis-Foch confirmed the hypothesis that quasi-steady aerodynamics can generally explain hovering insect flight. Ellington scrutinized the quasi-steady model, showing more of its weaknesses in describing hovering flight in light of better measurements of insect wing kinematics. Dickinson et al. incorporated wing rotations into the kinematics, describing how those rotations affect circulation and wake capture, and resolved the problems in Ellington's study. Wang et al. observed these effects in 2-D computational fluid dynamics, and produced formulas to calculate vorticity effects on an insect wing.

The accomplishments of the ornithopter control design community are still limited. There are some results however. Taylor et al. [17] performed dynamic analysis on insect flight based on data experimentally generated by real insects. They measured control derivatives for a linear-time-invariant and nonlinear time-periodic approximations of the insects' dynamics, and used this to develop conditions for stability and paradigms for control.

Open loop simulations have been conducted on vehicles such as the *Mentor* project [2] and Project Ornithopter's piloted ornithopter [3]. Schenato et al. [18] modeled an insect sized ornithopter and used averaging theory to produce controllers for flight stabilization. One specific shortcoming of averaging methods is their inapplicability to systems where the input periodicity has frequency on the same order as the system's dynamics; that is, the flapping frequency is not much higher than the natural frequencies and modes of the vehicle's flight dynamics. To account for this, the authors have applied Floquet analysis to ornithopter flight with arbitrary input parameters [16. 19]. For hovering flight however, it is important to analyze the stability of the ornithopter's position as well as its velocities.

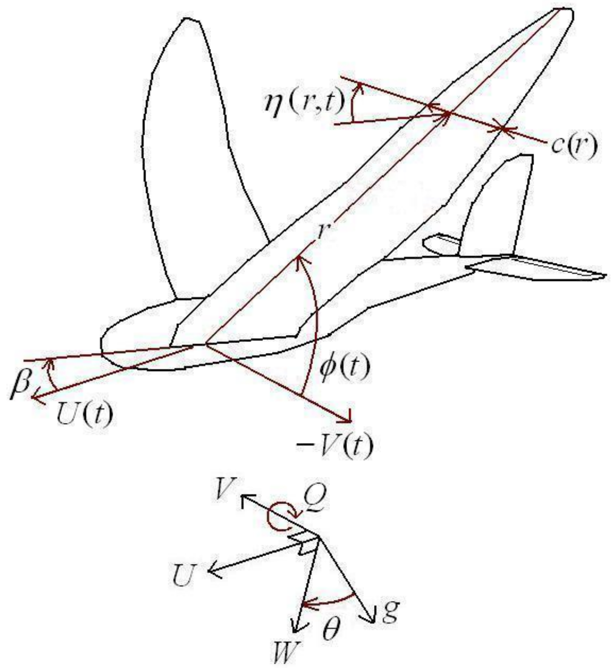

Figure 2.1 - Ornithopter schematic.

In this paper, the authors explore stabilization strategies based on the linear Floquet analysis. First, the Floquet analysis provides an accurate determination of the system's discrete-time eigenvalues, which determine stability. In a manner akin to Poincaré Mapping, this is done at a sampling time equal to the flapping frequency (this analysis cannot be performed at any higher frequency). Secondly, from the Floquet calculations, the resulting matrices can be used to create linear models of the system: an approximate continuous model or a computationally-dependent exact discrete-time model. We propose to use these models in control development to effect stability and trajectory tracking. We will then analyze the designed control laws for a prototype model (Figure 2.1).

One of the greater potential advantages of ornithopters is their ability to be adapted for multiple flight regimes. Since birds adapt for multiple types of flight, particularly steady forward flight and vertical takeoff and landing, the advantages of such capabilities in a MAV are clear. The typical disadvantage of highly maneuverable aircraft is near-instability; the instability helps the pilot change trajectory rapidly, but the system requires a highly trained pilot or a sophisticated controller. The proposed discrete-time control laws have not appeared in the ornithopter control literature, and we believe these periodic discrete-time laws (with their higher frequency actuation than once per flapping cycle) can be quite useful for increasing the stability of ornithopters designed with high maneuverability in mind.

3. Modeling

The ornithopter modeled in this paper and in previous work [16], is a fuselage with a standard empennage (horizontal and vertical stabilizers complete with deflecting control surfaces), and one pair of flapping wings. The wings are affixed to the fuselage so that the quarter-chord line of the wing coincides with the fuselage's center of mass. Each wing rotates (or heaves or plunges) and angle $\phi(t)$ about its root chord axis. Additionally, the wing twists about its quarter chord line an angle $\eta(r,t)$ distributed continuously along the span of the wing. The twist angle is defined as a linear distribution; there is zero twist at the root and maximum twist at the tip.

The authors use the methods outlined in previous work [19] to generate trim trajectories with acceptable limits on control input. Quasi-steady aerodynamics are the underlying forcing for these developments, but it is conceivable that with more computing power it would be possible to attempt this analysis with more sophisticated computational fluid dynamics software (accounting for unsteady and spatially dependent effects). Nonetheless, the aerodynamics are calculated through algebraic formulas which are easy to differentiate—this becomes necessary for calculations of the Jacobians used in control work. The aerodynamics formulas (explained with more detail in Dietl and Garcia [19] and Berman and Wang [20]) are these:

$$\Gamma(r) = -2C_L c(r)\frac{uv}{|\mathbf{v}|} + 2C_R c(r)^2 \dot{\eta} \tag{1}$$

$$d\mathbf{F}_v = \rho r c(r)|\mathbf{v}|\{C_D(0)\cos^2\alpha + C_D(\pi/2)\sin^2\alpha\}dr\begin{bmatrix} u \\ v \end{bmatrix} \tag{2}$$

$$dF_u = \left\{\left(\frac{m_w c(r)}{\bar{c}} + m_{22}\right)\frac{r}{R}v\dot{\eta} - \rho r v\Gamma - m_{11}\frac{r}{R}\dot{u}\right\}dr - dF_{v_u} \tag{3}$$

$$dF_y = \left\{-\left(\frac{m_w c(r)}{\bar{c}} + m_{11}\right)\frac{r}{R}u\dot{\eta} + \rho r u\Gamma - m_{22}\frac{r}{R}\dot{v}\right\}dr - dF_{v_y} \tag{4}$$

$$d\tau = \left\{(m_{11} - m_{22})\frac{r^2}{R}vu - I_a\frac{\ddot{\eta}}{R} + \frac{c(r)}{4}\rho v\Gamma\right\}dr - d\tau_v \tag{5}$$

The air-vehicle dynamics are affected by the reaction forces generated by the aerodynamics of flapping wings and tail-elevator action. These are the governing equations of a vehicle in flight:

$$\mathbf{F} = m\left.\frac{d\mathbf{v}_c}{dt}\right|_B + m(\boldsymbol{\omega} \times \mathbf{v}_c) \tag{6}$$

$$\mathbf{M} = \left.\frac{d\mathbf{H}}{dt}\right|_B + \boldsymbol{\omega} \times \mathbf{H} \tag{7}$$

The equations of motion for longitudinal vehicle dynamics are the Newton-Euler equations of motion for a rigid body with certain variables set to zero leaving 6 nontrivial equations for the motion of the fuselage:

$$\dot{U} = -QW - g\sin\theta + F_U(t)/m \tag{8}$$

$$\dot{W} = QU + g\cos\theta + F_W(t)/m \tag{9}$$

$$\dot{Q} = M(t)/I_y \tag{10}$$

$$\dot{\theta} = Q \tag{11}$$

$$\dot{x} = U\cos\theta + W\sin\theta \tag{12}$$

$$\dot{z} = U\sin\theta - W\cos\theta \tag{13}$$

where the functions $F_U(t)$, $F_W(t)$, and $M(t)$, contain the summation of all the forces and moments in their respective direction [16].

4. Stability and Floquet Analysis

This paper is solely concerned with steady-state trajectories: the vehicle is either hovering in one place or traveling forward with a constant speed and rate of climb; that is to say, in a stable dynamic equilibrium. The trick, however, is that ornithopters, through periodic aerodynamic forcing (flapping), cannot reach a truly steady state. Since the vehicle is a free body subject to oscillating forces (aerodynamic and mechanical), it is reasonable to expect that in a steady flight the velocities and pitch to oscillate as well. We thus define ornithopter trim to be a periodic trajectory with an unchanging average speed and rate of climb:

$$\dot{\mathbf{x}} = \mathbf{f}(\mathbf{x}),\ \mathbf{x} \in R^n \tag{14}$$

$$\mathbf{x}(t+T) = \mathbf{x}(t),\ \forall t \tag{15}$$

Trim is achieved through controlling various parameters so that there exists such a limit cycle in the phase space of the vehicle's dynamical system.

To calculate the required open-loop control parameters to produce a limit cycle with the desired speed and rate of climb condition, the authors use a multiple shooting root-finding algorithm [16]. First, a period of time T is assumed, equal to the period of flapping, that was determined from studying the prototype. Thus m times over that time span are chosen, over which the periodicity and speed conditions can be applied:

$$t_0 = 0 < t_1 < \cdots < t_{m-1} < t_m = T \tag{16}$$

For each time point t_i the dynamic states of the vehicle are guessed, which represent the vehicle's velocity and pitch angle at the various points throughout the cycle:

$$\mathbf{x}_{i_g} = \left\lfloor U_{i_g}, W_{i_g}, Q_{i_g}, \theta_{i_g} \right\rfloor^T, \tag{17}$$

and the steady-state. Additionally, open-loop control parameters are chosen to affect the trajectory. In this study, the elevator deflection δe and the wing plunging amplitude C_h are chosen because they have a strong effect on the trajectory (the elevator has a greater effect on pitch control, the plunging amplitude has a greater effect on velocity).

$$\mathbf{u}_g = \left[\delta e_g, C_h\right]^T . \tag{18}$$

Other control parameters that are not used in this step are the flapping frequency and the twisting amplitude. Flapping frequency is not used because it requires a different algorithm (one that does not depend explicitly on the time of integration) to solve for the limit cycle. Twisting amplitude is not used because it produces implausibly large twisting amplitudes. It is also possible to use non-constant elevator angle and plunging amplitude by parametrizing these motions, but this is eschewed for the sake of simplicity.

Once the initial conditions and control parameters are chosen, the equations of motion are integrated from each guessed state at each time point to the next time point:

$$\tilde{\mathbf{x}}_{i+1}(t_{i+1}) = \int_{t_i}^{t_{i+1}} \dot{\mathbf{x}}(t, \mathbf{x}, \mathbf{u})dt,\ \tilde{\mathbf{x}}_{i+1}(t_i) = \mathbf{x}_{i_g} . \tag{19}$$

We can now express the periodicity, continuity, speed, and rate of climb conditions formulaically:

$$\begin{cases} \tilde{\mathbf{x}}_1 - \mathbf{x}_{1_g} = \mathbf{0} \\ \tilde{\mathbf{x}}_2 - \mathbf{x}_{2_g} = \mathbf{0} \\ \vdots \\ \tilde{\mathbf{x}}_m - \mathbf{x}_{m_g} = \mathbf{0} \\ \mathbf{x}_{m_g} - \mathbf{x}_{0_g} = \mathbf{0} \\ x(T) - \bar{\dot{x}}T = 0 \\ z(T) - \bar{\dot{z}}T = 0 \end{cases} \tag{20}$$

where the equations for $x(T)$ and $z(T)$ represent the average speed and climb rate of the vehicle, and the remaining equations represent the periodicity and continuity of the desired dynamic trajectory. These equations are nonlinear, so that the authors choose Newton iteration to solve for the unknown variables.

The Jacobian of (20) with respect to $\mathbf{x}_{i_g}$ and $\mathbf{u}_g$ must be calculated to perform the Newton iteration.

$$\begin{bmatrix} \begin{Bmatrix} \frac{\partial \tilde{\mathbf{x}}_1}{\partial \mathbf{x}_0} & -\mathbf{I} & & & \\ & \frac{\partial \tilde{\mathbf{x}}_2}{\partial \mathbf{x}_1} & -\mathbf{I} & & \\ & & \ddots & \ddots & \\ & & & \frac{\partial \tilde{\mathbf{x}}_m}{\partial \mathbf{x}_{m-1}} & -\mathbf{I} \\ -\mathbf{I} & & & & \mathbf{I} \end{Bmatrix} & \begin{Bmatrix} \frac{\partial \tilde{\mathbf{x}}_1}{\partial \mathbf{u}} \\ \frac{\partial \tilde{\mathbf{x}}_2}{\partial \mathbf{u}} \\ \vdots \\ \frac{\partial \tilde{\mathbf{x}}_m}{\partial \mathbf{u}} \\ \mathbf{0} \end{Bmatrix} \\ \begin{Bmatrix} \frac{\partial x(T)}{\partial \mathbf{x}_0} & \frac{\partial x(T)}{\partial \mathbf{x}_1} & \cdots & \frac{\partial x(T)}{\partial \mathbf{x}_{m-1}} & 0 \\ \frac{\partial z(T)}{\partial \mathbf{x}_0} & \frac{\partial z(T)}{\partial \mathbf{x}_1} & \cdots & \frac{\partial z(T)}{\partial \mathbf{x}_{m-1}} & 0 \end{Bmatrix} & \begin{Bmatrix} \frac{\partial x(T)}{\partial \mathbf{u}} \\ \frac{\partial z(T)}{\partial \mathbf{u}} \end{Bmatrix} \end{bmatrix} \begin{bmatrix} \Delta \mathbf{x}_0 \\ \Delta \mathbf{x}_1 \\ \vdots \\ \Delta \mathbf{x}_{m-1} \\ \Delta \mathbf{x}_m \\ \Delta \mathbf{u} \end{bmatrix} = - \begin{bmatrix} \tilde{\mathbf{x}}_1 - \mathbf{x}_1 \\ \tilde{\mathbf{x}}_2 - \mathbf{x}_2 \\ \vdots \\ \tilde{\mathbf{x}}_m - \mathbf{x}_m \\ \mathbf{x}_m - \mathbf{x}_0 \\ x(T) - \bar{\dot{x}}T \\ z(T) - \bar{\dot{z}}T \end{bmatrix} \tag{21}$$

These Jacobians $\frac{\partial \tilde{\mathbf{x}}_i}{\partial \mathbf{x}_j}$ are calculated through integrating the Jacobians of the dynamic equations of motion with respect to $\mathbf{x}_{i_g}$ and $\mathbf{u}_g$ separately. The following differential equations are integrated from the time t_{i-1} to t_i.

$$\frac{d}{dt}\left(\frac{\partial \tilde{\mathbf{x}}_i(t)}{\partial \mathbf{x}_{i-1}}\right) = \left[\left.\frac{\partial \mathbf{f}(\mathbf{x})}{\partial \mathbf{x}}\right|_{\mathbf{x}=\mathbf{x}^*(t)}\right]\left(\frac{\partial \tilde{\mathbf{x}}_i(t)}{\partial \mathbf{x}_{i-1}}\right), \ \frac{\partial \tilde{\mathbf{x}}_i(t_{i-1})}{\partial \mathbf{x}_{i-1}} = I \tag{22}$$

$$\frac{d}{dt}\left(\frac{\partial x(T,t)}{\partial \mathbf{x}_{i-1}}\right) = \left[\left.\frac{\partial \dot{x}(\mathbf{x})}{\partial \mathbf{x}}\right|_{\mathbf{x}=\mathbf{x}^*(t)}\right]\left(\frac{\partial \mathbf{x}(t)}{\partial \mathbf{x}_{i-1}}\right), \ \frac{\partial x(T,t_{i-1})}{\partial \mathbf{x}_{i-1}} = \mathbf{0} \tag{23}$$

$$\frac{d}{dt}\left(\frac{\partial \tilde{\mathbf{x}}_i(t)}{\partial \mathbf{u}}\right)=\left[\left.\frac{\partial \mathbf{f}(\mathbf{x})}{\partial \mathbf{x}}\right|_{\mathbf{x}=\mathbf{x}^*(t)}\right]\left(\frac{\partial \tilde{\mathbf{x}}_i(t)}{\partial \mathbf{u}}\right)+\left.\frac{\partial \mathbf{f}(\mathbf{x})}{\partial \mathbf{u}}\right|_{\mathbf{x}=\mathbf{x}^*(t)},\ \frac{\partial \tilde{\mathbf{x}}_i(t_{i-1})}{\partial \mathbf{u}}=\mathbf{0} \tag{24}$$

$$\frac{d}{dt}\left(\frac{\partial x(T,t)}{\partial \mathbf{u}}\right)=\left[\left.\frac{\partial \dot{x}(T,t)}{\partial \mathbf{x}}\right|_{\mathbf{x}=\mathbf{x}^*(t)}\right]\left(\frac{\partial \tilde{\mathbf{x}}(t)}{\partial \mathbf{u}}\right),\ \frac{\partial x(T,0)}{\partial \mathbf{u}}=\mathbf{0} \tag{25}$$

Each of the Jacobians in (21) are the solutions of the above equations at the endpoint of integration. After sufficiently iterating (21), the result gives a list of points on the desired limit cycle and a list of control offsets.

If we look at the limit cycle as a discrete-time system, that is to look at its Poincaré map:

$$\mathbf{x}(k+1)=\mathbf{P}(\mathbf{x}(k)) \tag{26}$$

then we can analyze it for stability. The Jacobian of the Poincaré map $\mathbf{M}$ is called the Monodromy matrix:

$$\mathbf{M}=\frac{\partial \mathbf{P}}{\partial \mathbf{x}(k)}, \tag{27}$$

and it is related to the previously calculated Jacobians in (22):

$$\frac{\partial \tilde{\mathbf{x}}_m(t)}{\partial \mathbf{x}_{m-1}}\frac{\partial \tilde{\mathbf{x}}_{m-1}(t)}{\partial \mathbf{x}_{m-2}}\cdots\frac{\partial \tilde{\mathbf{x}}_2(t)}{\partial \mathbf{x}_1}\frac{\partial \tilde{\mathbf{x}}_1(t)}{\partial \mathbf{x}_0}=\mathbf{M} \tag{28}$$

When the modulus of all the eigenvalues of **M** are less than or equal to 1, then the system is stable.

5. Open-Loop Simulation Results

To illustrate the feedback control concepts that follow, two unstable trajectories are analyzed here, one in hovering flight and the other in forward flight.

5.1. Hovering Flight

In the first step, to find a hovering trim, the simulation converged to a limit cycle in the dynamic states *U, W, Q,* and θ (Figure 2.2a) and the vehicle trajectory *x* and *z* (Figure 2.2b, 2.3). This is the base (reference) trajectory, which the controller will attempt to follow. This limit cycle is unstable (Figure 2.3); the Newton method calculation cannot select whether it finds a stable result. Thus the limit cycle will need a compensating controller. Some control specialists object to the term 'limit cycle' as applied to unstable orbits. But since these are the chief concern of the paper, and that the term 'isolated periodic orbit' is awkward, the authors will call such unstable cycles 'limit cycles' for lack of a better term.

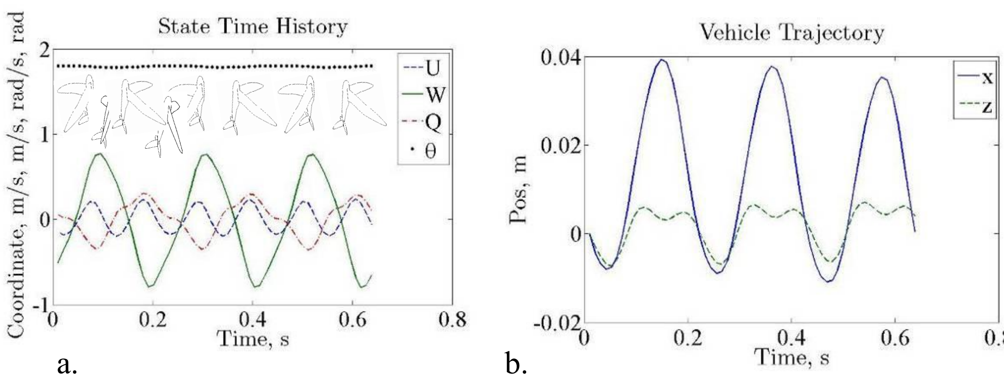

Figure 2.2 - a. A limit cycle in the dynamic states. b. The vehicle's trajectory.

The stability of the limit cycle can be determined by its Floquet multipliers, the eigenvalues of the limit cycle's Monodromy matrix **M**. The Monodromy matrix can be determined numerically through an initial value problem. Given an arbitrary dynamic system:

$$\dot{\mathbf{x}} = \mathbf{f}(\mathbf{x}), \tag{29}$$

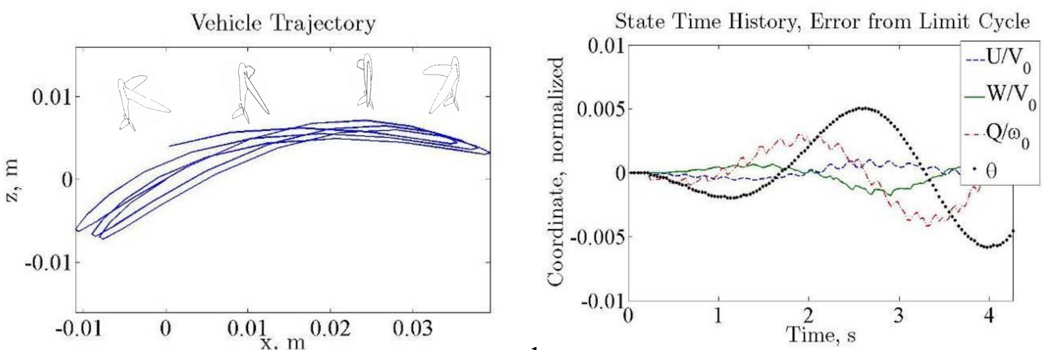

Figure 2.3 - a. Ornithopter c.g. trajectory during a divergence from an unstable limit cycle. b. Error from the desired trajectory.

with closed orbit $\mathbf{x}^*(t)$ of period T, the Monodromy matrix is the solution at time T of the differential equation:

$$\frac{d\mathbf{M}(t)}{dt} = \left.\frac{\partial \mathbf{f}(\mathbf{x})}{\partial \mathbf{x}}\right|_{\mathbf{x}=\mathbf{x}^*(t)} \mathbf{M}(t), \mathbf{M}(0) = \mathbf{I} \tag{30}$$

For our hovering trajectory, the Monodromy matrix can be used to analyze the dynamic modes. In this example we have computed:

$$\mathbf{M} = \begin{bmatrix} .73 & -.076 & .049 & .15 & 0 & 0 \\ -.027 & .22 & -.018 & -.96 & 0 & 0 \\ -.10 & .43 & .90 & -.59 & 0 & 0 \\ -.022 & .054 & .20 & .94 & 0 & 0 \\ -.063 & .12 & .00032 & -.16 & 1 & 0 \\ .17 & -.0018 & .021 & .018 & 0 & 1 \end{bmatrix} \tag{31}$$

with eigenvalues $\lambda = 0.95 \mp 0.48i, 1, 1, 0.73, 0.16$, thus the system is unstable (Figure 4).

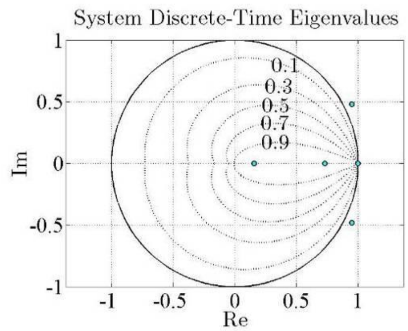

Figure 2.4 - Floquet multipliers are plotted in the z-plane.

The complex-conjugate eigenvalues $\lambda = 0.95 \mp 0.48i$ have magnitude 1.06, and are thus unstable. This pair's eigenvector is:

$$\mathbf{v}_{1,2} = \begin{bmatrix} -.11 \pm .13i & .15 \mp .37i & .79 & .056 \pm .35i & .22 \pm .057i & -.058 \mp .011 \end{bmatrix}^T, \quad (32)$$

which indicates stronger excitation in the downward velocity *W* and in pitch rate *Q*. The resulting oscillations grow without bound. This is illustrated in Figure 2.3b. The errors are expressed in terms of states normalized [21] by characteristic a characteristic length $l_0 = 2m/\rho S$, a characteristic velocity $V_0 = \sqrt{gl_0}$, and a characteristic rotation rate $\omega_0 = 2\pi\sqrt{g/l_0}$.

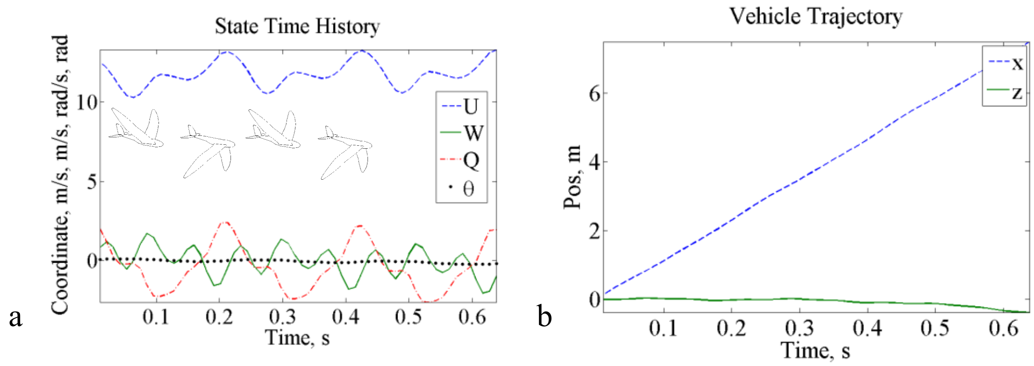

Figure 2.5 - Forward Flight a. Dynamic and b. c.g. Trajectory.

5.2. Forward Flight

Similar results are obtained for the forward flight case. In Figures 2.5 and 2.6 the open loop dynamic trajectory is shown, both in the dynamic states (U, W, Q, and θ) and in the position states of the vehicle c.g. Note that in the forward flight case, the vehicle's pitch θ is near zero and the only component not near zero is the forward velocity U. This is how intuition would assume forward flight would take place: as is common in larger birds and airplanes. The system's Floquet multipliers are shown in Figure 2.7, demonstrating the instability.

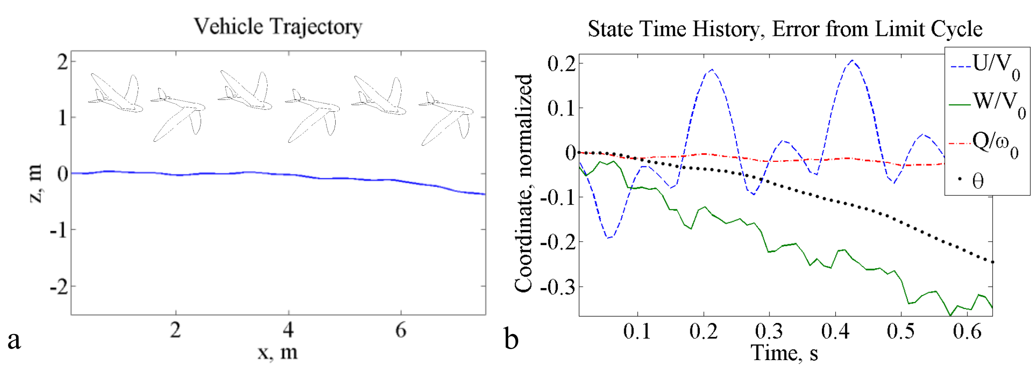

Figure 2.6 - Divergence of Forward Trajectory due to Instability.

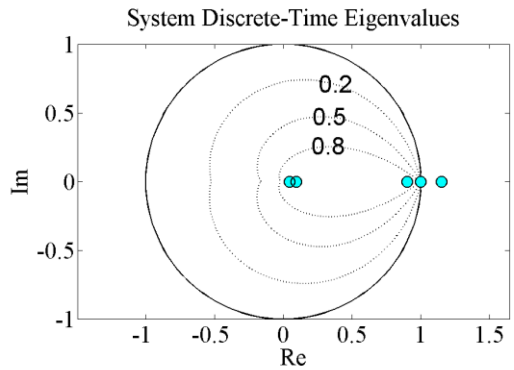

Figure 2.7 - The open-loop poles of the ornithopter in forward flight.

6. Closed Loop Control

To stabilize the limit cycle trajectories is the goal of feedback control in ornithopter flight. The literature concerning feedback control systems is replete with methods for controlling time-invariant systems, but time-varying nonlinear systems have a lesser pedigree. Fortunately for ornithopter flight the trim conditions—though time-varying—are periodic. By linearizing the system about those trajectories, it is possible to take advantage of the properties of periodic systems to develop control laws that are either time-invariant or periodic, but that do not require specific time horizon calculations (as in the general time-varying linear quadratic regulator) or extensive look-up tables for every plausible combination of dynamic states.

Linearization of the dynamic system is the first step toward designing a control system, as it facilitates analysis and computation of control laws. One method for linearizing the ornithopter equations of motion is shown in the following section. Using this linearization it is possible to develop many sorts of control laws, and in this paper three control designs will be limned.

The first control design is a classical proportional-derivative (PD) controller, designed through the root locus method. The second concept is a discrete-time periodic linear quadratic regulator (D-PLQR). This time-varying controller has sufficient bandwidth to stabilize the system (a time-invariant discrete-time controller at the flapping frequency does not satisfy the Nyquist criterion), and its control law is optimized for the time-varying nature of the system's dynamics. The final concept is a discrete-time periodic linear quadratic Gaussian regulator (D-PLQG), a D-PLQR controller utilizing a periodic discrete-time Kalman filter.

6.1. Linearization

To facilitate control design, it is useful to have a linearized system. Since there is no steady-state operating point, we linearize the system dynamically about the limit cycle $\mathbf{x}^*(t)$. In general, an appropriate linearization of a time-varying nonlinear system is in the form of a first-order linear time-varying system of difference equations. At first, the reference trajectory must be discretized [$\mathbf{x}^*(k) = \mathbf{x}^*(t_k)$, $\mathbf{u}^*(k) = \mathbf{u}^*(t_k)$]. For simplicity, the variables $\mathbf{x}(k) = \mathbf{x}_{actual}(k)\text{-}\mathbf{x}^*(k)$] and $\mathbf{u}(k) = \mathbf{u}_{actual}(k)\text{-}\mathbf{u}^*(k)$] are defined. Then, the linearized equations of error from that trajectory are:

$$\mathbf{x}(k+1) = \mathbf{F}_k \mathbf{x}(k) + \mathbf{\Gamma}_k \mathbf{u}(k) \tag{29}$$

The matrices $\mathbf{F}_k$ and $\mathbf{\Gamma}_k$ are time-varying state transition and control matrices from time t_k to time t_{k+1}. To calculate these matrices, the Jacobians of the nonlinear system of equations from time k to time k+1 are integrated thusly:

$$\frac{d\mathbf{F}_k(t)}{dt} = \left.\frac{\partial \mathbf{f}(\mathbf{x},\mathbf{u})}{\partial \mathbf{x}}\right|_{\mathbf{x}=\mathbf{x}^*(t)} \mathbf{F}_k(t), \quad \mathbf{F}_k(0) = \mathbf{I} \tag{30}$$

$$\frac{d\mathbf{\Gamma}_k(t)}{dt} = \left.\frac{\partial \mathbf{f}(\mathbf{x},\mathbf{u})}{\partial \mathbf{x}}\right|_{\mathbf{x}=\mathbf{x}^*(t)} \mathbf{\Gamma}_k(t) + \left.\frac{\partial \mathbf{f}(\mathbf{x},\mathbf{u})}{\partial \mathbf{u}}\right|_{\mathbf{x}=\mathbf{x}^*(t)}, \quad \mathbf{\Gamma}_k(0) = \mathbf{0} \tag{31}$$

Then, $\mathbf{F}_k$ and $\mathbf{\Gamma}_k$ are the matrix solutions of (30) and (31) respectively at time t_{k+1}. This procedure can be done for any nonlinear system, but for this particular case it is fit to make the intervals of discretization to be fractions of the limit cycle's period. If each sampling time is equal to the flapping period T, then $\mathbf{F}_k$ is time invariant and equal to the Monodromy matrix. If the sampling time is some fraction of T, then there is a collection of system matrices, periodic in T. Thus, if the period is divided into 10 samples, then there are 10 unique matrices $\mathbf{F}_k$ (and $\mathbf{\Gamma}_k$), with k equaling 1 through 10. In this way, a controller can be developed with sufficient bandwidth for the motion generated by flapping.

The time invariant case is interesting because the system in discrete-time can be converted back to a continuous-time system using the Tustin[19a] transformation, thus allowing design of classical controllers for continuous time systems. These controllers act at a high enough frequency to satisfy the Nyquist criterion but allow for simplified implementation.

The discrete system can thus be put in this form:

$$\dot{\mathbf{x}}(t) = \mathbf{A}\mathbf{x}(t) + \mathbf{B}\mathbf{u}(t) \tag{32}$$

where

$$\mathbf{A} = \frac{1}{T}\log_e(\mathbf{F}) \tag{33}$$

and

$$\mathbf{B} = \left(\int_0^T e^{\mathbf{A}\lambda} d\lambda \right)^{-1} \mathbf{\Gamma} \tag{34}$$

where λ is a dummy integration variable, and $\mathbf{F}$ (= $\mathbf{F}_k$) and $\mathbf{\Gamma}$ (= $\mathbf{\Gamma}_k$) (for all k) are taken from (30) and (31) when integrated for exactly one flapping period.

6.2. Classical Control

To begin, the authors apply classical control methods to ornithopter stabilization. The approach here is to use a single-input-single-output (SISO) controller, controlling the pitch of the vehicle by means of the elevator. We shall show that with this method we can stabilize the vehicle through an increased effective pitch damping.

The controller used here is a proportional-derivative controller. The pitch sensor data is fed back into the controller where the controller produces a control gain equal to a weighted sum of the errors in the pitch and pitch rate of the vehicle.

$$\delta e(t) = -K_{\Theta}[\theta(t) - \theta_0(t)] - K_Q[Q(t) - Q_0(t)] \tag{35}$$

$\theta_0(t)$ and $Q_0(t)$ are periodic reference trajectories of the pitch rate and pitch, where and K_θ and K_Q are the proportional and derivative control gains. These periodic reference trajectories must be calculated prior to operating the controller (illustrated in Figures 2.2a and 2.5a), and they must be stored in the controller's memory. As it is impossible to store a continuous function in computer memory, the reference trajectories are approximated by a third-order spline function to ensure the continuous differentiability of the functions.

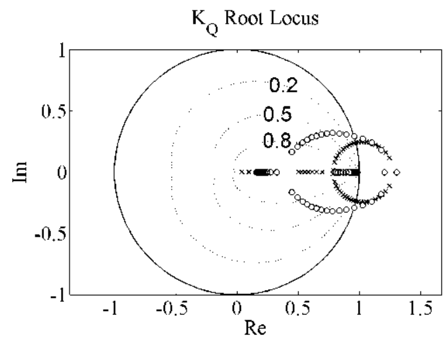

Figure 2.8 - Closed-loop K_Q root locus of the ornithopter in forward flight ‘x’ and hovering ‘o’ with PD control.

The work of PD control design is to select appropriate control gains. Using the nonlinear model of ornithopter flight and the Floquet analysis outlined in the above section, a root locus method was used to study the system’s pole movements under this control law. As Figure 2.8 shows, the Floquet multipliers cross over the unit circle in the *z*-plane when an appropriate value of the derivative control gain K_Q is used.

6.3. Simulation of Ornithopter Flight with PD Control

The ornithopter was simulated flying using the PD controller, and the dynamic modes were observed (Figure 2.9). In both hovering flight and forward flight the system achieved stability.

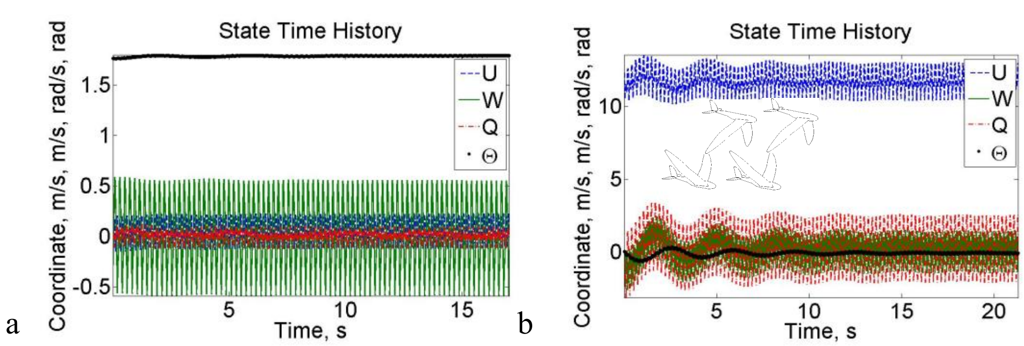

Figure 2.9 - a. Hovering and b. forward trajectories of the ornithopter.

During the flapping cycle, the vehicle's dynamics are constantly changing. This can be illustrated using a diagram of the system's continuous-time poles and zeros during an open-loop flapping cycle (Figure 2.10). During this cycle, the poles and zeros move around the complex plane; they travel around the complex plane in an orbit with period equal to the flapping period. The poles exist on both sides of the imaginary axis, with some crossing that axis during the cycle (Figure 2.10*a*). This implies that the system's dynamic modes, and the ways the system responds to perturbations, are not constant. However, it does not imply that the dynamic modes change from stable to unstable; in a time-varying system, the continuous-time poles themselves do not determine stability (but the Monodromy matrix does)!

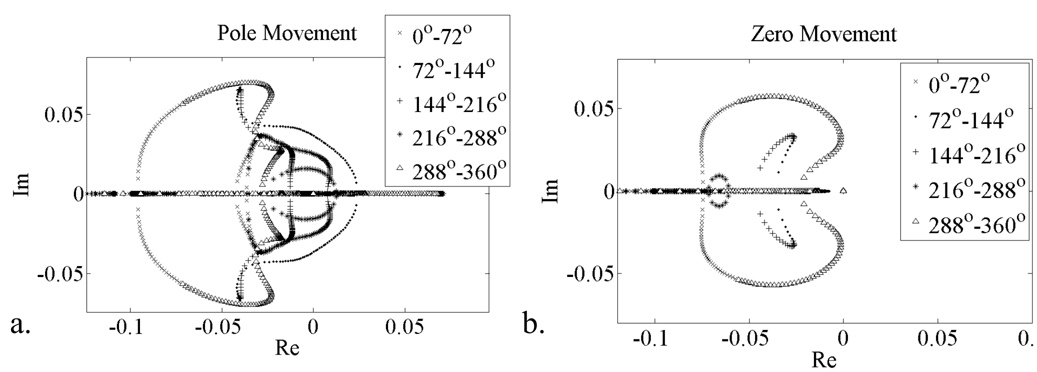

Figure 2.10 - Open-loop pole (a.) and zero (b.) movement during forward flight. The legend shows the ranges of flapping phase angle.

What this does indicate though, is that any constant-gain controller could provide beneficial (stabilizing) action during parts of the cycle and adverse action during other parts of the cycle. Thus it is important to choose a control law that stabilizes the system more than it destabilizes the system on average.

Additionally, this suggests that a constant-gain controller cannot drive the system to equilibrium (here defined as tracking the desired trajectory exactly), because during phases with adverse control action the controller will drive the system away from that equilibrium. The result is a control action that alternately drives the system toward the desired equilibrium and then away from it. If the control law is designed skillfully, however, it will drive the system to a new equilibrium (a new limit cycle) as close to the intended equilibrium as possible, but still with a discernible error from the desired open-loop limit cycle.

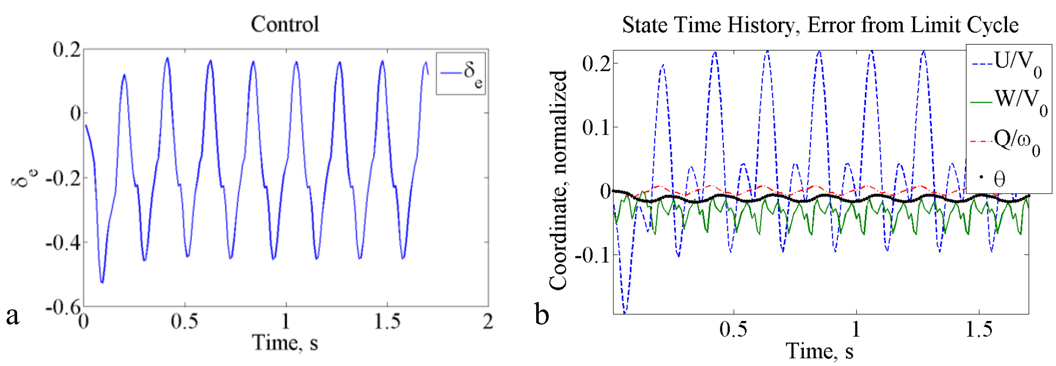

Figure 2.11 - a. PD Control action to stabilize forward flight. b. Dynamic states error from original limit cycle.

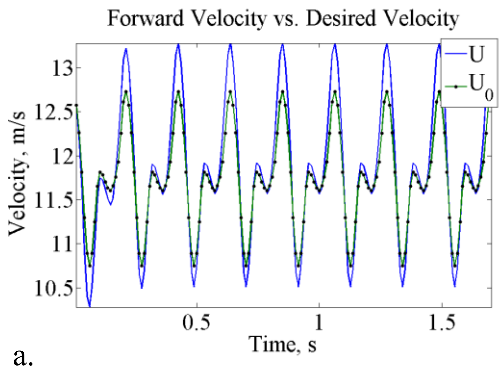

a.

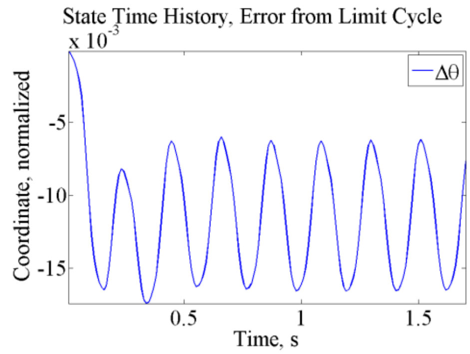

b.

Figure 2.12 - Error in the controlled limit cycle. a. Forward Velocity vs. Desired Forward Velocity, b. Error in the Vehicle Pitch (normalized to radians).

As we shall see, the PD controller exhibits this behavior. Although driving the vehicle to stability, it does not drive the vehicle to the original equilibrium, which would have been the expected behavior of a stabilizing PD controller on a time-invariant system (Figure 11). This effect is more pronounced in the velocity states (Figure 12a), but the error in the pitch is also nonzero (Figure 12b). This also happens in hover.

6.4. Discrete-time Periodic Linear Quadratic Regulator (D-PLQR)

Continuous-time control, through analog electronics or approximated with high-speed computers, is the standard and simplest control strategy. It is relatively easy to design, analyze, and implement. However, it is usually designed for a time-invariant plant, using the a priori information about the plant's dynamic response. Ornithopters have time-dependent dynamics, but during a trim condition these dynamics are periodic. These dynamics can be averaged and used to design appropriate controllers.

Discrete time controllers are more amenable to time-varying dynamics in computer control, since the controller operates only at specific points in time during a trajectory. Only a finite number of control operations during each cycle are needed; at each point in time, the computer can utilize a unique control gain and reference trajectory point. Thus, the Discrete-time Periodic Linear Quadratic Regulator is proposed.

A linear quadratic regulator is a feedback control law that minimizes a quadratic cost function of the system states and control inputs [22]:

$$J = \frac{1}{2}\mathbf{x}^T(n)\mathbf{S}\,\mathbf{x}(n) + \frac{1}{2}\sum_{k=0}^{n-1}\left[\mathbf{x}^T(k)\mathbf{Q}\mathbf{x}(k) + \mathbf{u}^T(k)\mathbf{R}\mathbf{u}(k)\right] \tag{36}$$

This cost is minimized subject to the constraints of the system’s dynamics (29). The control law that minimizes this cost balances the error in the states during the flight with the amount of energy expended in control, weighted by the matrices **Q**, **R**, and **S**.

Control laws of this form are generally used for fixed-time-horizon controllers, or they are used for time-invariant plants. The advance proposed here is to generate a time-varying control law with no fixed time horizon. To regulate of a periodic trajectory, the cost is modified so that is an average cost per period. If there are *n* steps per flapping period, the amended cost is this:

$$J_n = \frac{1}{2}\sum_{k=0}^{n-1}\left[\mathbf{x}^T(k)\mathbf{Q}\mathbf{x}(k) + \mathbf{u}^T(k)\mathbf{R}\mathbf{u}(k)\right] \tag{37}$$

The solution to this problem gives a control gain **u**(*k*) in this form:

$$\mathbf{u}(k) = -\mathbf{K}_k\mathbf{x}(k) \tag{38}$$

where $\mathbf{K}_k$ is a time-varying, periodic gain matrix:

$$\mathbf{K}_k = \mathbf{R}^{-1}\mathbf{\Gamma}_k{}^T\mathbf{P}_k \tag{39}$$

It is calculated prior to implementing control on the vehicle, it is proportional to the solution $\mathbf{P}_k$ of the discrete-time, time varying Riccati equation:

$$\mathbf{P}_k = \mathbf{Q} + \mathbf{F}_k{}^T\mathbf{P}_{k+1}\mathbf{F}_k - \mathbf{F}_k{}^T\mathbf{P}_{k+1}\mathbf{\Gamma}_k\left[\mathbf{R} + \mathbf{\Gamma}_k{}^T\mathbf{P}_{k+1}\mathbf{\Gamma}_k\right]^{-1}\mathbf{\Gamma}_k{}^T\mathbf{P}_{k+1}\mathbf{F}_k \tag{40}$$

The periodic time varying matrix, $\mathbf{P}_k$, needs to be calculated over one flapping period. Note that this equation is evaluated backwards in time, but it can be easily executed for systems with periodic coefficients. The following substitutions can be used to make equation (40) periodic by replacing the original time varying system matrices with periodic system matrices (i.e. the index *k* only goes from 0 to n-1 where the index *j* increases ad infinitum).

$$\mathbf{F}_k = \mathbf{F}_j,\ \mathbf{\Gamma}_k = \mathbf{\Gamma}_j,\ \mathbf{P}_k = \mathbf{P}_j\ \mathbf{K}_k = \mathbf{K}_j, \tag{41}$$

$$k \equiv j(\text{mod } n),\ j = 1,\ ...,\ n\text{-}1 \tag{42}$$

One further property of this recursive equation is that it is guaranteed to converge to a set or periodic gains if the system is controllable (a property that can be determined from the system's controllability matrix). Thus, the controller gains can be computed with the following algorithm:

1) Select a positive-definite matrix $\mathbf{P}_{k_0}$ as an initial condition.
2) Calculate $\mathbf{P}_k$ from (40)
3) Continue iterating through (40) until $\mathbf{P}_k$ is sufficiently close to $\mathbf{P}_{k+n}$ and store $\mathbf{P}_1$ through $\mathbf{P}_{n-1}$.
4) Calculate $\mathbf{K}_1$ through $\mathbf{K}_{n-1}$ using (39) and store in memory.

5) Implement the control law $\mathbf{u}(k) = -\mathbf{K}_j\mathbf{x}(k)$ for all k.

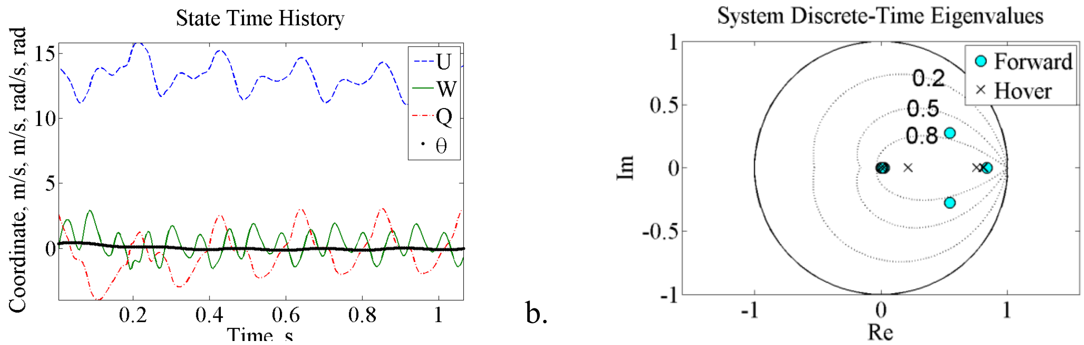

Figure 2.13 - a. State Trajectories (Forward) and b. Pole Movement for System Under P-DLQR control.

6.5. Simulation of Ornithopter Flight with D-PLQR Control

With the gains for the discrete-time controller calculated, the system can now be stabilized.

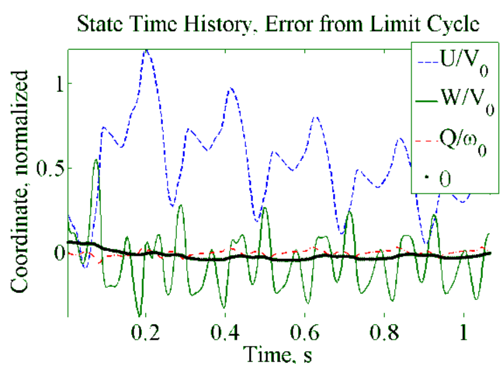

Figure 2.14 - Error in states [x(t)-x*(t)] under P-DLQR in forward flight.

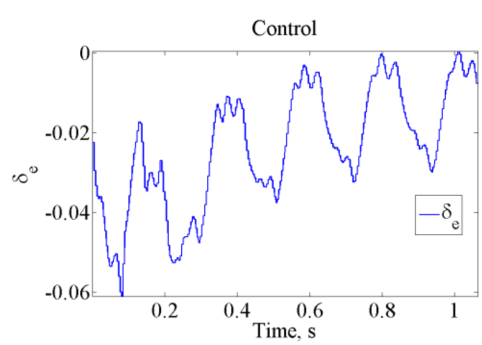

Figure 2.15 - Control Effort under P-DLQR.

Figure 2.13a shows a stabilized trajectory. As can be seen in Figure 2.13b, the ornithopter's flight is again stabilized under this discrete-time controller. This controller has lower gain than the PD controller, and thus it has a slower recovery time. Figure 2.14 shows the system's stabilized trajectory for hovering flight. The value of this low gain can be seen in Figure 2.15, however, as the control effort is not large when there are no disturbances. The PD controller with constant gains (Figure 2.12b) had larger errors without the presence of disturbances.

6.6. Discrete-time Periodic Linear Quadratic Gaussian Regulator (D-PLQG)

One application of interest is to apply the D-PLQR controller to a system with sensor feedback. Since D-PLQR assumes perfect state feedback it is an unrealistic controller for ornithopters, on which it is difficult to measure certain states. This modification to the D-PLQR controller uses as its input the sensor output from the system. Therefore, a Kalman Filter converts this non-ideal sensor signal to useful error signals for the D-PLQR gain matrix to affect. Kalman filters have been well established in engineering literature (see for instances Bar-Shalom et al. [23]), and they have been used as part of the Linear Quadratic Gaussian (LQG) controller. This periodic discrete-time controller extends the use of LQG controllers to periodic systems.

The control input is proportional to the estimated state errors instead of a known state error as before. Thus:

$$\mathbf{u}(k+1) = -\mathbf{K}(k+1)\hat{\mathbf{x}}(k+1) \tag{43}$$

where $\hat{\mathbf{x}}(k)$ is the estimate of the states' errors. It is computed through the below recursive algorithm (with details in [23]).

$$\hat{\mathbf{x}}(k+1) = \bar{\mathbf{x}}(k+1) + \mathbf{W}(k)\left[\mathbf{y}(k+1) - \mathbf{C}\bar{\mathbf{x}}(k+1)\right] \tag{44}$$

and

$$\bar{\mathbf{x}}(k+1) = \mathbf{F}(k)\hat{\mathbf{x}}(k) + \mathbf{\Gamma}(k)\mathbf{u}(k) \tag{45}$$

$$\mathbf{y}(k) = \mathbf{C}\mathbf{x}(k) + \mathbf{w}(k) \tag{46}$$

where **C** is the sensor matrix, **w** is sensor noise, and **W**(*k*) is a periodic matrix of Kalman gains solved through recursion:

$$\overline{\mathbf{P}}(k+1) = \mathbf{F}(k)\mathbf{P}(k)\mathbf{F}^T(k) + \mathbf{Q}(k) \tag{47}$$

$$\mathbf{S}(k+1) = \mathbf{C}\overline{\mathbf{P}}(k+1)\mathbf{C}^T + \mathbf{R}(k+1) \tag{48}$$

$$\mathbf{W}(k+1) = \overline{\mathbf{P}}(k+1)\mathbf{C}^T\mathbf{S}^{-1}(k+1) \tag{49}$$

$$\mathbf{P}(k+1) = \overline{\mathbf{P}}(k+1) - \mathbf{W}(k+1)\mathbf{S}(k+1)\mathbf{W}^T(k+1) \tag{50}$$

where **Q**(*k*) and **R**(*k*) are noise covariance matrices. When these equations are iterated as the equations for the Periodic gain (38-42) a periodic filter gain **W**(*k*) can be stored as **K**(*k*) is stored for the P-DLQR.

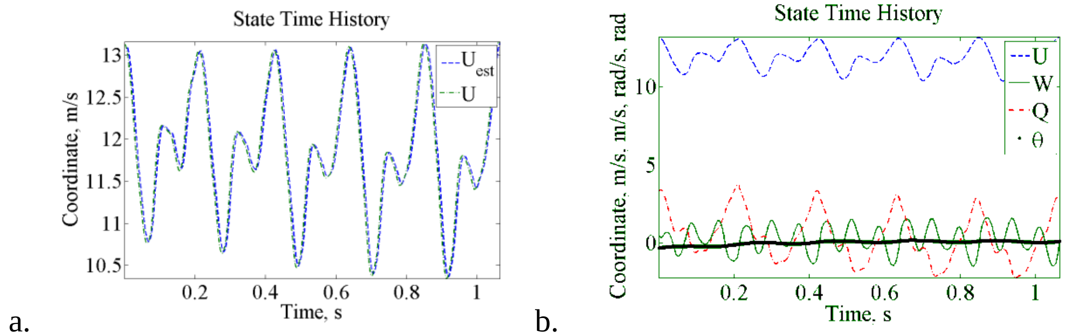

Figure 2.16 - a. State trajectories under P-DLQG. b. Forward velocity and estimated forward velocity.

6.7. Control With Sensor Feedback

This section discusses the results obtained from simulating the system with noisy sensor feedback utilizing a reliable sensor system (Figure 2.16). By incorporating noise, this provides a more realistic look at the challenge of controlling this aeronautic system. Also, this system uses a reduced set of sensors than full state feedback. For this case, the direct measurement of $W(t)$, the downward velocity, was eliminated.

Periodic DLQR is retained as the chosen control law, but with filtered sensor output as the controller's input. The sensor output is sent through a Kalman Filter , which attenuates the noise and estimates the states' true values. Linear quadratic Gaussian controllers are often not robust to modeling error, especially when underdamped. This system, however, is unstable, so care is required to design a controller that does not further destabilize the system. The simulation is not likely to suffer from errors due to mismodeled dynamics, but this would be a concern in an actual ornithopter. Also, the added trouble from removing known states and adding noise to the sensor readings can drive a system that is stable under state feedback to instability.

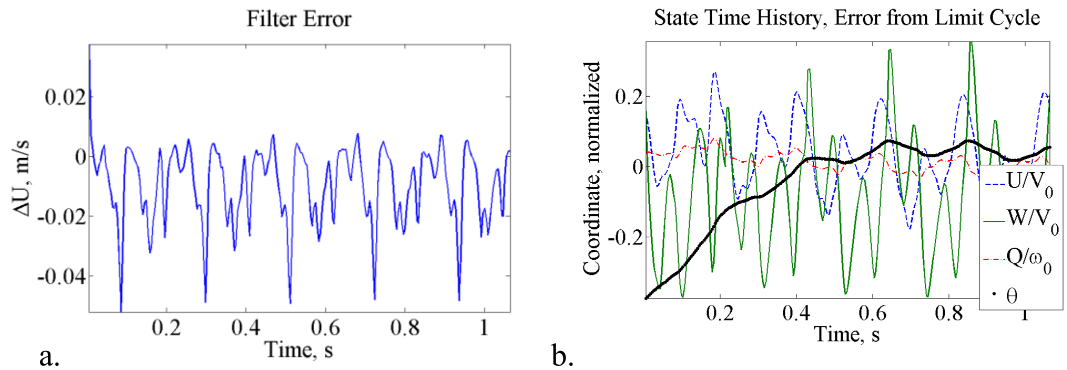

Figure 2.17 - a. Filter error during the simulated trajectory. b. State trajectory errors.

Figure 2.17 shows the errors in the estimator algorithm. A heuristic for control with estimators is that the controller should work better when the error in the estimated states is minimized. In this model, the sensors are modeled as direct measurements of the states of the system, so it is not very difficult to estimate the states. However, with noise added, the system can never achieve perfect equilibrium, again because the noise throws the control input away from equilibrium, and thus jarring the system. Notice also, that the unmeasured state *W* exhibits the most dramatic swings, since it is not directly subject to the control action.

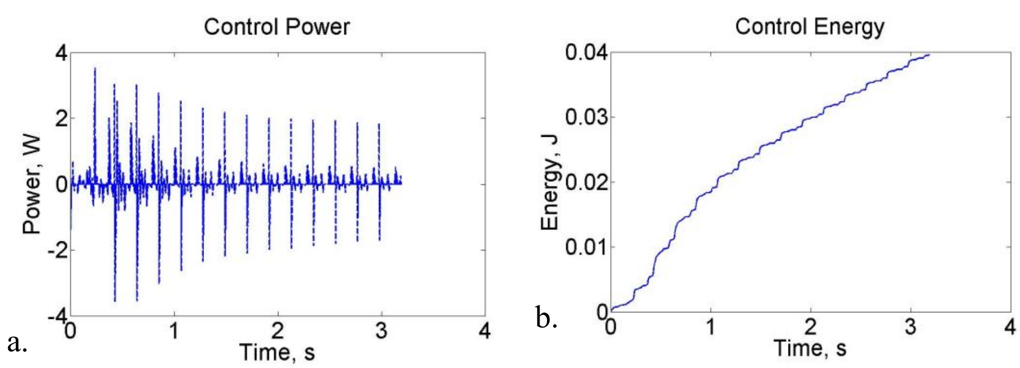

Figure 2.18 - Control effort required for stability under P-DLQG controller. a. Energy, b. Power.

The main results are that the system becomes stabilized, the control effort is not excessively large, and the system tracks the desired trajectory well.

7. Discussion of Results

7.1. Control Effort

The discrete-time LQR used the least amount of control energy of the three control strategies as implemented, but all controllers' efforts approached zero during the simulation. With noise applied to the system, however, the control effort approached a steady state, but due to disturbances, it did not settle to zero (Figure 2.18a). The power was calculated only at the controller sampling time; the zero-order hold control law only allows discrete-time motions of the controller. However, the energy expended is not excessive (Figure 2.18b).

7.2. Practical Implementation

The continuous controller has one great advantage, that it has constant gains. The problem is that the error signal must be calculated along the trajectory, thus some form of computer control is needed. The system must provide from memory the desired trajectory at all times—the actual implementation will settle for some high sampling rate—through some approximation of the calculated limit cycle, perhaps a spline or Fourier series. The spline used in simulation worked quite well.

The periodic discrete-time controller is a more natural fit for a computer controlled vehicle, but it provides some challenges of its own. The computer must store the required gain matrices and for each sampling time during the trajectory, and the system must maintain knowledge of the phase of the flapping stroke in order to select the correct gain. This requires accurate measurements of the phase of the flapping motion, memory recall, and rapid calculations by the controller.

8.Conclusion

These results are encouraging. First they show this ornithopter to be controllable in two useful flight regimes, those that would make an ornithopter valuable for ISR platform duties or for search and rescue missions. Presumably, this could be extended to other flight regimes including steady climbs and descents, and various turns. Second, the control energy required in the periodic DLQR is not excessive. This makes the system not extremely difficult to operate at these quasi-steady-state situations. The one problem with the control was the extreme throw of the elevators required to trim the vehicle in the two states, but this can be corrected easily through a larger control surface. It would be interesting to make a morphing vehicle, to have the entire horizontal tail surface swivel as a trim mechanism. (Since the elevator lift effect has been modeled linearly, the large deflections in the elevator could be converted to a proportionate small deflection in the larger surface without much difficulty.) This adds the benefit of allowing the control surface (the actual elevator) to have maximum throw in each direction for stabilization and this could segregate the open-loop and closed-loop control functions to different actuators.

REFERENCES

[1] Moon, F. C., 2007, *The Machines of Leonardo Da Vinci and Franz Reuleaux*, Springer, Dordrecht, The Netherlands, pp. 255-262.

[2] Zdunich, P., Bilyk, D., MacMaster, M., Loewen, D., Delaurier, J., Kornbluh, R., Low, T., Stanford, S., and Holeman, D., “Development and Testing of the *Mentor* Flapping-Wing Micro Air Vehicle,” *Journal of Aircraft*, 44(5), 1701-1711, (2007).

[3] DeLaurier, J. D., 1999, “The Development and Testing of a Full-Scale Piloted Ornithopter,” Canadian Aeronautics and Space Journal, **45(2)**, pp. 72-82.

[4] Cox, A., Monopoli, D., Cveticanin, D., Goldfarb, M., and Garcia, E., 2002, “The Development of Elastodynamic Components for Piezoelectrically Actuated Flapping Micro-Air Vehicles,” *Journal of Intelligent Material Systems and Structures*, **13**(9), 611-615.

[5] S. Avadhanula, R. J. Wood, E. Steltz, J. Yan and R. S. Fearing, “Lift Force Improvements for the Micromechanical Flying Insect” IEEE Int. Conf. on Intelligent Robots and Systems, Oct 28-30, 2003, Las Vegas NV.

[6] Richter, C., and Lipson, H. (2010) "Untethered Hovering Flapping Flight of a 3D-Printed Mechanical Insect", *12th Int. Conference on Artificial Life* (Alife XII), in press.

[7] van Breugel F., Regan W., Lipson H., (2008) "From Insects to Machines: A Passively Stable, Untethered Flapping-Hovering Micro Air Vehicle," *IEEE Robotics and Automation Magazine*, 15(4), pp. 68-74.

[8] van Breugel F., Teoh Z. E., Lipson H. (2007), "A Passively Stable Hovering Flapping Micro-Air Vehicle", in D. Floreano et al. (eds.), *Flying Insects and Robots*, pp 171-184, Springer.

[9] Theodorsen, T., “General Theory of Aerodynamic Instability and the Mechanism of Flutter,” NACA TR 496, 1935.

[10] Jones, R. T., “Unsteady Lift of a Wing of Finite Aspect Ratio,” NACA TR 681, 1940.

[11] DeLaurier, J. D., “Aerodynamic Model for Flapping-Wing Flight,” Aeronautical Journal, Vol. 97, No. 7, April 1993, pp. 125–130.

[12] Weis-Fogh, T., and Jensen, M., “Biology and Physics of Locust Flight, 1: Basic Principles in Insect Flight. A Critical Review,” Proceedings of the Royal Society of London, Series B: Biological Sciences, Vol. 239, No. 667, 1956, pp. 415–458. doi:10.1098/rstb.1956.0007

[13] Ellington, C. P., 1984, “The Aerodynamics of Hovering Insect Flight. I. The Quasi-Steady Analysis,” *Phil. Trans. R. Soc. Lond. B.* **305**, 1-15.

[14] Dickinson, M. H., Lehmann, F. O., and Sane, S. P., “Wing Rotation and the Aerodynamic Basis of Insect Flight,” Science, Vol. 284, No. 5422, 1999, pp. 1954–1960. doi:10.1126/science.284.5422.1954

[15] Wang, Z. J., 2005, “Dissecting Insect Flight,” *Annual Review of Fluid Mechanics*, **37**, 183-210.

[16] Dietl, J. M., and Garcia, E., 2008, “Stability in Ornithopter Longitudinal Flight Dynamics,” *Journal of Guidance, Control, and Dynamics*, **31**(4), pp. 1157-1162.

[17] Taylor, G. K., Bomphrey, R. J., and Hoen, J., “Insect Flight Dynamics and Control,” 44th AIAA Aerospace Sciences Meeting and Exhibit, AIAA 2006-32, Jan. 2006.

[18] Schenato, L, Deng, X., and Sastry, S., “Flapping Flight for Miomimetic Robotic Insects: Part II—Flight Control Design,” IEEE Transactions on Robotics, 22(4), 789-803, (2006).

[19] Dietl, J. M., and Garcia, E., 2007, "Ornithopter Flight Stabilization," Proc. SPIE **6525**, 65250K.

[20] G. Berman, and Z. J. Wang, "Energy-minimizing kinematics in hovering insect flight," J. Fluid Mech. 582, 153-168 (2007).

[21] Wickenheiser, A. M., and Garcia, E., "Optimization of Perching Maneuvers Through Vehicle Morphing," *Journal of Guidance, Control, and Dynamics*, **31**(4), pp. 815-823.

[22] Ogata, K., 1995, *Discrete-Time Control Systems 2nd Edition*, Pearson-Prentice Hall, pp. 566-596.

[23] Bar-Shalom, Y., Li, X. R., and Kirubarajan, T., 2001, *Estimation with Applications to Tracking and Navigation*, John Wiley and Sons Inc., pp. 200-212.

CHAPTER 3

ORNITHOPTER TRANSITION TRAJECTORY: DESIGN AND SIMULATION[1]

1. Abstract

Mesoscale ornithopters inhabit a niche in our vehicle technology; they are capable of both hovering and forward flight. The ability to achieve both of these flight regimes is valuable, and this can be done through clever control of vehicle parameters and by having sufficient actuation authority. The problem to transition between forward flight and hovering flight in an ornithopter is described. An ornithopter dynamic model based on quasi-steady aerodynamics and Newton-Euler rigid body dynamics is developed and shown to accurately describe the problem of interest. A brief exegesis on nonlinear dynamics and flight stability is used to develop stabilizing feedback controllers used to encourage the flight to remain within satisfactory errors of the desired trajectories. Then, feedback control is shown to allow stable transition between forward flight and hover. The optimal control problem to develop transition trajectories is then described and several optimal paths are calculated. These are shown to be amenable to stabilizing feedback control as well. It is concluded that the methods outlined in this paper will prove useful in the design of micro-air-vehicles with unique capabilities.

---

[1] From Dietl, J. M. and Garcia, E., "Ornithopter Transition Trajectory: Design and Simulation," submitted to *Aerospace Science and Technology*.

2. Introduction

Birds, in their vast diversity, are capable of soaring flight, aerobatics, hovering, vertical takeoff and landing, and flight regime optimization through morphing. For the first century of aircraft design fixed frame flight has achieved a plethora of aircraft [1]. Yet a rational approach to the design, analysis, and control of ornithopters is elusive, even though natural existence proofs surround us.

The Wright Brothers' airplane achieved—in addition to the first heavier than air manned flight—the first flight of a morphing aircraft. Subsequent rigid-winged airplanes, however, were the paradigm of a simpler—easier, faster, stronger, cheaper—vehicle design. Having nearly exhausted the design space of the rigid-winged and fixed-framed aircraft, engineers have returned their attention to morphing wing aircraft and ornithopters to fill the meso- and microscale unmanned air vehicle design void.

Ornithopters are aircraft that mimic birds by producing propulsion and lift through flapping wings. Engineers now attempt to exploit this peculiar structural topology to create new flight regimes. The totality of what flapping wings will enable the engineer to create is unknown, but engineers and biologists have been (for the last 25 or so) exploring the possibilities.

First, the main objective was to model the aerodynamics of flapping wings. This entailed studying bird and insect flight [2, 3], experiments with manmade wings and biological specimens [4-6], reevaluation of nearly-forgotten aerodynamics discoveries from the earlier 20th century [7, 8], and computer modeling at various levels of sophistication: from simple quasi-steady models to full-blown 4-dimensional computational fluid dynamics [9]. The challenges in modeling a 4-dimensional flow field are still incompletely resolved, and the modeling of flexible structures in this flow field complicates the matter as well. However, sufficient insight has been gained in order to study the effects of aerodynamics on flapping-wing flight [10].

Second, aerodynamics modeling allowed engineers to study flight itself. They can analyze the force balance on a flying bird, predict the accelerations generated by flapping maneuvers, and model flight trajectories in computer simulations [11]. Increasingly, engineers can analyze the stability of flight trajectories, design stabilizing feedback controllers, and optimize flapping motions for reduced power consumption [10, 12].

Third, the objective is to design a complete flight. Analyzing trajectories is a necessary step for this goal. But, what a bird knows instinctively, how to flap its wings (and control its tail) to move through the sky, engineers must discover through experiment, simulation, and design. Thus, using the tools of aerodynamic modeling, flight dynamics modeling, heuristic comparisons, control theory, and dynamic optimization, it is manifest that flight trajectories be generated [13].

Previous work has demonstrated how to design stable trim trajectories for flapping flight. [14, 15] The engineers realized that pure dynamic equilibrium was impossible for a flight vehicle with time-varying forcing, and thus developed the flight criterion that a trim condition be periodic (at the flapping frequency) [14]. This led to designs for forward flight and hovering flight. The next goal is to design a trajectory connecting these flight conditions: an ornithopter in forward flight can quickly assume a hovering trajectory and from that hovering trajectory resume forward flight at the desired speed.

This also builds on the work of engineers designing vertical takeoff and landing controllers for fixed-wing aircraft, especially for a vehicle using primarily passive aerodynamics (low thrust-to-weight) to slow the vehicle and to perch upon a designated location [16]. However, the ornithopter with capability for hover has a high thrust-to-weight ratio, so active thrust vectoring is encouraged for both takeoff and landing.

There will be two analyses presented here. First, an ornithopter will be simulated during an abrupt transition from stable forward flight to hovering flight. Starting at a designated time, the flapping control parameters will be changed from those of forward flight to those of a hovering flight. If the system is within the basin of attraction of the stable hovering trajectory, the system will be drawn toward a stable hover. The second analysis will be of a designed trajectory. This uses dynamic optimization to select a set of flapping control parameters to drive the system from forward flight to hovering flight.

3. Methodology

3.1. Vehicle Dynamics Model

All of the subsequent analyses are in reference to a single model ornithopter. This model has one pair of flapping wings and a tail with controllable elevator (Figure 3.1). This meso-scale ornithopter—with a 72.4 *cm* wingspan—is an ideal candidate ornithopter for the study of flight dynamics and flapping aerodynamics. It is large enough for models to be easily constructed and have a useful payload. It is small enough that it would not require an internal combustion engine, be dangerous to the operator, or be difficult to build. Also, it is on the scale of a bird of prey studied by March et al. [17].

The wings have 2 degrees of freedom: heaving, the main mode of flapping, and twisting, which controls the direction of thrust. These angles are governed by sinusoidal forcing functions of the same frequency. Along the span, the heaving angle is constant.

$$\phi(t) = C_h \cos(2\pi f t) + \phi_0 \tag{1}$$

The twisting angle is linearly distributed along the span; there is zero twist at the root (r = 0) and maximum twist at the tip (r = R) of the wing. Additionally, the twist angle has a phase offset from the heaving angle. This is typically 90° [5].

$$\eta(r,t) = C_t r \cos(2\pi f t + \phi_{\eta 0}) \tag{2}$$

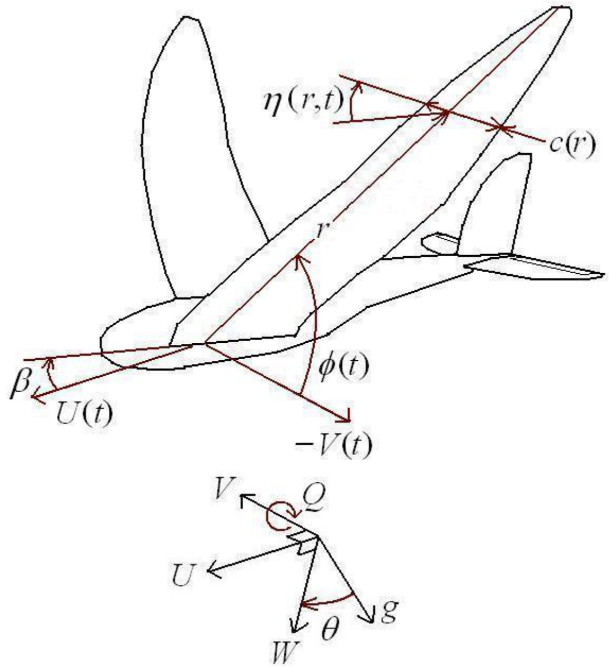

Figure 3.1 - Ornithopter Prototype Schematic. The ornithopter for our study has 2 flapping wings and standard vertical and horizontal stabilizers.

Along the span of the wings, the aerodynamic forces are calculated using quasi-steady approximations taken from Wang [9] and are the same used by the authors in previous works [14, 15]. Forces are calculated at each airfoil section and then integrated over the length of the wing to develop the resultant force on the vehicle. Quasi-steady force calculations are used rather than CFD analysis because the calculations are computationally tenable and reasonably accurate.

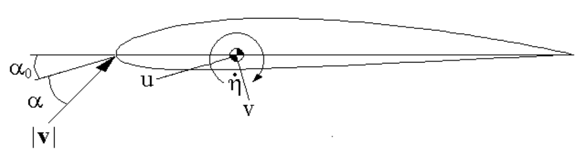

Figure 3.2 - Representative airfoil section with variables illustrated.

The circulation about an arbitrary reasonably flat section (Figure 3.2) is calculated based on the instantaneous velocity and rotation rate of the section in the fluid.

$$\Gamma(r) = -2C_L c(r)\frac{uv}{|\mathbf{v}|} + 2C_R c(r)^2 \dot{\eta} \tag{3}$$

The parasitic drag force includes two drag coefficients, one for zero angle attack and one for 90 degrees. These are blended appropriately using a sinusoidal mixing function.

$$d\mathbf{F}_v = \rho r c(r)|\mathbf{v}|\left\{C_D(0)\cos^2\alpha + C_D(\pi/2)\sin^2\alpha\right\}dr\begin{bmatrix} u \\ v \end{bmatrix} \tag{4}$$

This circulation is coupled with the parasitic drag and added mass to calculate total force on a section per unit span. Added mass terms account for accelerating the pockets of air around the wings. They are necessary in time-varying quasi-static aerodynamics calculations, which do not implicitly calculate the state of the fluid, but only follow the states of the moving structures.

$$dF_u = \left\{\left(\frac{m_w c(r)}{\bar{c}} + m_{22}\right)\frac{r}{R}v\dot{\eta} - \rho r v\Gamma - m_{11}\frac{r}{R}\dot{u}\right\}dr - dF_{v_u} \tag{5}$$

$$dF_y = \left\{-\left(\frac{m_w c(r)}{\bar{c}} + m_{11}\right)\frac{r}{R}u\dot{\eta} + \rho r u\Gamma - m_{22}\frac{r}{R}\dot{v}\right\}dr - dF_{v_y} \tag{6}$$

$$d\tau = \left\{(m_{11} - m_{22})\frac{r^2}{R}vu - I_a\frac{\ddot{\eta}}{R} + \frac{c(r)}{4}\rho v\Gamma\right\}dr - d\tau_v \tag{7}$$

The equations of motion for longitudinal vehicle dynamics are the Newton-Euler equations of motion for a rigid body.

$$\mathbf{F} = m\left.\frac{d\mathbf{v}_c}{dt}\right|_B + m(\boldsymbol{\omega} \times \mathbf{v}_c) \tag{8}$$

$$\mathbf{M} = \left.\frac{d\mathbf{H}}{dt}\right|_B + \boldsymbol{\omega} \times \mathbf{H} \tag{9}$$

The full 3 dimensional equations of rigid body motion can be simplified by constraining the vehicle longitudinally. This is acceptable for problems that only involve longitudinal variables such as the forward flight to hover maneuver. The longitudinal equations of motion of the fuselage are as follows:

$$\dot{U} = -QW - g\sin\theta + F_U(t)/m \tag{10}$$

$$\dot{W} = QU + g\cos\theta + F_W(t)/m \tag{11}$$

$$\dot{Q} = M(t)/I_y \tag{12}$$

$$\dot{\theta} = Q \tag{13}$$

$$\dot{x} = U\cos\theta + W\sin\theta \tag{14}$$

$$\dot{z} = U\sin\theta - W\cos\theta \tag{15}$$

The functions $F_U(t)$, $F_W(t)$, and $M(t)$, contain the summation of all the aerodynamic forces and moments of the wings and tail on the fuselage. This includes the inertial forces of the wings transmitted through the wing joints.

Using the above equations for the aerodynamics and equations of motion for the vehicle, it is possible to simulate the flight of the ornithopter with a computer. All the computations in this study were carried out in the MATLAB programming environment [18]. MATLAB's *ode45.m* Runge-Kutta algorithm was particularly helpful.

3.2. Steady Trajectory Generating Algorithm.

In order to connect forward flight and hovering flight trajectories, first it is necessary to study these trajectories individually. This involves calculating the required input parameters to effect each trajectory, analyzing the trajectories for stability, and stabilizing the trajectories through feedback control. That is, for hover and forward flight, controls must be chosen that trim the vehicle. Here follows a summary of methods applied in [14], [15], and [19] to accomplish these goals.

The authors employed a multiple shooting root-finding algorithm to calculate input parameters and initial conditions that produce a steady state in trim. Note that for flapping flight there is no steady state velocity or position, so trim is redefined for flapping flight to mean a periodic condition in the state variables. For generating a steady motion—straight and level, hover, or steady climb or descent—we have a defined distance traveled during each cycle.

The purpose of the following algorithm is to find a periodic trajectory in the phase space of flapping flight: it is basically a root-finding algorithm, analogous to finding a fixed point in a time-invariant system. This algorithm assumes that for each set of given input parameters there exists one periodic trajectory that satisfies the given flight conditions of speed and rate of climb.

The algorithm begins by dividing the flapping period $T=1/f$ into m intervals, and at the endpoints of the intervals m+1 state variable vectors are guessed:

$$t_0 = 0 < t_1 < \cdots < t_{m-1} < t_m = T \tag{16}$$

$$\mathbf{x}_{i_g} = \left[U_{i_g}, W_{i_g}, Q_{i_g}, \theta_{i_g}\right]^T \tag{17}$$

In addition, two control position variables **u** are guessed. Each control variable remains constant during the cycle; although it would be possible to make these periodic, it is difficult to quantify in practice. These variables will affect the limit cycle's position in phase space.

$$\mathbf{u}_g = \left[\delta e_g, C_t\right]^T \tag{18}$$

The equations of motion are then integrated from each guess to the next time step:

$$\tilde{\mathbf{x}}_{i+1}(t_{i+1}) = \int_{t_i}^{t_{i+1}} \dot{\mathbf{x}}(t, \mathbf{x}, \mathbf{u})dt,\ \tilde{\mathbf{x}}_{i+1}(t_i) = \mathbf{x}_{i_g} \tag{19}$$

The periodicity, continuity, and hovering conditions are equivalent to:

$$\begin{cases} \tilde{\mathbf{x}}_1 - \mathbf{x}_{1_g} = \mathbf{0} \\ \tilde{\mathbf{x}}_2 - \mathbf{x}_{2_g} = \mathbf{0} \\ \vdots \\ \tilde{\mathbf{x}}_m - \mathbf{x}_{m_g} = \mathbf{0} \\ \mathbf{x}_{m_g} - \mathbf{x}_{0_g} = \mathbf{0} \\ x(T) = TV \\ z(T) = 0 \end{cases} \tag{20}$$

and these conditions can be enforced by the root-finding algorithm. Note that the constraints are satisfied when the guessed parameters $\mathbf{x}_{i_g}$ equals the values of the integrated trajectories $\tilde{\mathbf{x}}_i$ at the appropriate time. These equations have been set for a set of constant altitude trajectories with varying speed *V*. By changing the desired speed, the algorithm will find values of the states and control variables that allow the vehicle to travel as desired.

4. Steady-State Trajectory Analysis

4.1. Hovering Flight

The hovering trajectory is computed first; as it is the goal of the transition trajectory, it ought to receive the greatest attention. Figure 3.3 shows the states of the vehicle over a few flapping cycles while in the hovering trajectory. These states are periodic. Note especially the pitch θ. Referring to Figure 3.1, the pitch oscillates about an average value near 2.1 *rad*. This means that the vehicle is nearly vertical as it hovers in the air, not very much unlike the posture of a person treading water. In this flight mode, the wings' stroke plane is nearly horizontal, directing all thrust downward, athwart the effect of gravity.

This does not work perfectly, however. The system is unstable, as Figures 3.4 and 3.5 testify. While the dynamic states appear periodic and stable, the position states quickly diverge from their initial conditions.

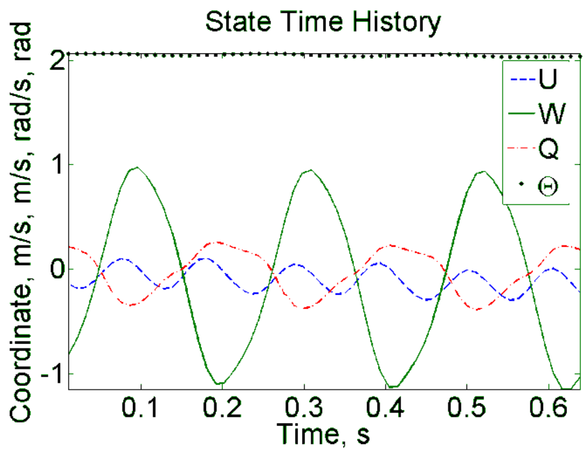

Figure 3.3 - Dynamic states of hovering limit cycle.

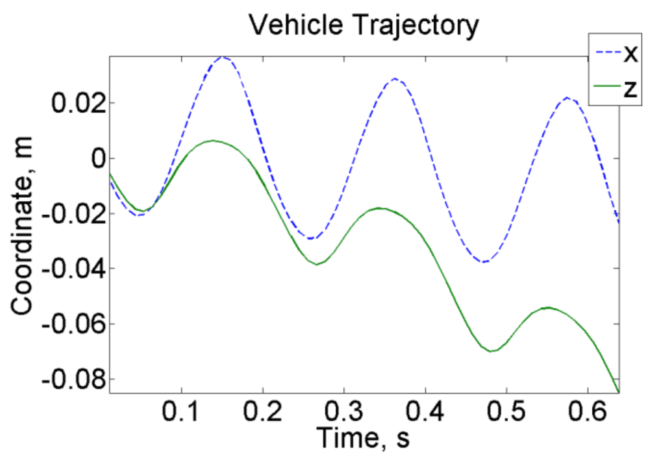

Figure 3.4 - The vehicle's hovering trajectory.

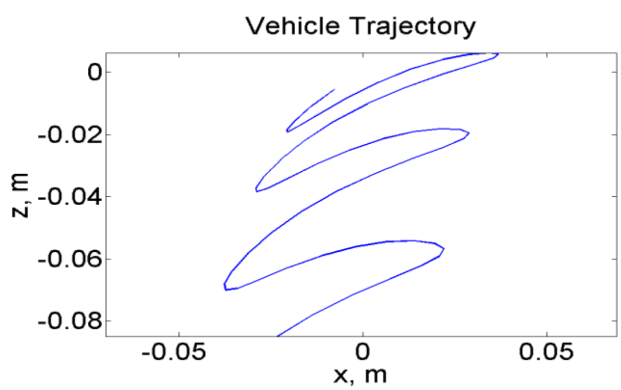

Figure 3.5 - Divergence from limit cycle due to instability.

The stability of the limit cycle can be determined by its Floquet multipliers, the eigenvalues of the limit cycle's Monodromy matrix **M**. The Monodromy matrix can be determined numerically through an initial value problem. Given an arbitrary dynamic system:

$$\dot{\mathbf{x}} = \mathbf{f}(\mathbf{x}) \tag{21}$$

with closed orbit $\mathbf{x}^*(t)$ of period T, the Monodromy matrix is the solution at time T of the differential equation:

$$\frac{d\mathbf{M}(t)}{dt} = \left.\frac{\partial \mathbf{f}(\mathbf{x})}{\partial \mathbf{x}}\right|_{\mathbf{x}=\mathbf{x}^*(t)} \mathbf{M}(t),\ \mathbf{M}(0) = \mathbf{I} \,. \tag{22}$$

For our hovering trajectory, the eigenvalues were computed to be:

$$\lambda = 1.25, \quad 0.777 \pm 0.342i, \quad 0.117 \,. \tag{23}$$

These are manifestly unstable. The effect of this instability is to drive the system away from its equilibrium. A main cause of this instability is that the vehicle is meant to be maneuverable. If it were extremely stable at hover, it would require much more control authority to drive it away from hover.

The errors are expressed in terms of states normalized by characteristic a characteristic length $l_0 = 2m/\rho S$, a characteristic velocity $V_0 = \sqrt{g l_0}$, and a characteristic rotation rate $\omega_0 = 2\pi\sqrt{g/l_0}$ [16].

4.2. Forward Flight

The forward flight trajectory behaves similarly. However, it is a limit cycle in only the states, but not in the positions. Figure 3.6 shows the dynamic states. In this case, the pitch of the vehicle is near horizontal, akin to the pitch of a fixed wing airplane. Indeed, the wings generate lift in the classical sense here, mainly affected by the forward motion. The flapping motion is relegated toward providing thrust, allowing the vehicle to overcome the dissipating drag forces.

The forward velocity *U* cycles about a steady positive value. These all achieve the effect of forward motion at 3 *m/s* can be observed in Figure 3.7.

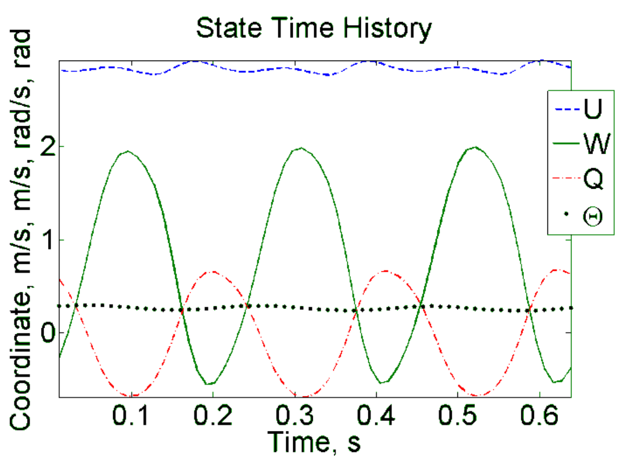

Figure 3.6 - Dynamic states during forward flight.

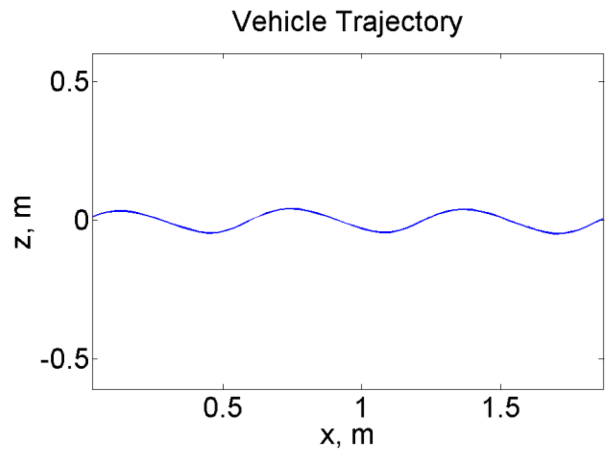

Figure 3.7 - Vehicle c.g. trajectory in forward flight.

4.3. Stabilization Strategies

For both hovering and forward flight, we have calculated a trim state. However, the Floquet analysis reveals that simply because the vehicle is trimmed it may not perform a desired trajectory without diverging. The calculated trim trajectories are not necessarily stable. Yet, once a trajectory of suitable speed and elevation is found it must be made stable. The Monodromy matrix of the limit cycle provides the appropriate measure of the limit cycle's stability, but if the cycle is unstable it must be controlled. Among the possible control strategies are continuous linear controllers, discrete-time linear controllers, and nonlinear controllers. For simplicity's sake we will concentrate on continuous linear feedback controllers.

To design a linear control law it is first necessary to create a linearized model of the dynamic system. The easiest is a linear-time-invariant model in state space:

$$\mathbf{x}(k+1) = \mathbf{F}\mathbf{x}(k) + \mathbf{\Gamma}\mathbf{u}(k), \tag{24}$$

where **F** is a system matrix in discrete time, **u** is the control vector, and **Γ** is the input matrix for the controls. The matrices can be found by integrating the following differential equations for one orbit of the limit cycle:

$$\frac{d\mathbf{F}(t)}{dt} = \left.\frac{\partial \mathbf{f}(\mathbf{x},\mathbf{u})}{\partial \mathbf{x}}\right|_{\mathbf{x}=\mathbf{x}^*(t)} \mathbf{F}(t),\ \mathbf{F}(0) = \mathbf{I} \tag{25}$$

and:

$$\frac{d\mathbf{\Gamma}(t)}{dt} = \left.\frac{\partial \mathbf{f}(\mathbf{x},\mathbf{u})}{\partial \mathbf{x}}\right|_{\mathbf{x}=\mathbf{x}^*(t)} \mathbf{\Gamma}(t) + \left.\frac{\partial \mathbf{f}(\mathbf{x},\mathbf{u})}{\partial \mathbf{u}}\right|_{\mathbf{x}=\mathbf{x}^*(t)},\ \mathbf{\Gamma}(0) = \mathbf{0}. \tag{26}$$

We then convert the system from discrete time to continuous time. The **F** matrix is the state transition matrix of the following system:

$$\dot{\mathbf{x}}(t) = \mathbf{A}\mathbf{x}(t) + \mathbf{B}\mathbf{u}(t) \tag{27}$$

$$\mathbf{F} = e^{\mathbf{A}T}, \tag{28}$$

Therefore, **A** can be computed using the matrix logarithm:

$$\mathbf{A} = \frac{1}{T}\log(\mathbf{F}), \tag{29}$$

Similarly, **B** is calculated from this transformation (assuming that the input **u** is a constant over each discretization interval, the zero-order hold approximation) [20]:

$$\mathbf{B} = \left(\int_0^T e^{\mathbf{A}\lambda} d\lambda\right)^{-1} \mathbf{\Gamma}, \tag{30}$$

where λ is a dummy integration variable. This is what MATLAB uses to convert discrete-time systems to continuous time. The continuous state space systems can be then converted to transfer functions for classical control design.

4.3.1. Proportional-Derivative Control

This controller effects the elevator deflection proportional to the pitch of the vehicle and its derivative *Q*.

$$\delta e(t) = -K_P \theta(t) - K_D Q(t) \tag{31}$$

This controller can enforce stability, but is incapable of tracking velocity.

4.3.2. Linear Quadratic Regulator

This controller uses the information fed back from all the dynamic states to enforce the flight requirements. Given a linear dynamic system (17) satisfying the criteria of controllability, (and observability), it can be stabilized using the linear quadratic regulator algorithm. The control law takes the form

$$\mathbf{u}(t) = -\mathbf{K}\mathbf{x}(t), \tag{32}$$

where

$$\mathbf{K} = \mathbf{R}^{-1}\mathbf{B}^T\mathbf{S} \tag{33}$$

and **S** satisfies the algebraic Riccati equation

$$\mathbf{A}^T\mathbf{S} + \mathbf{S}\mathbf{A} - \mathbf{S}\mathbf{B}\mathbf{R}^{-1}\mathbf{B}^T\mathbf{S} + \mathbf{Q} = \mathbf{0}. \tag{34}$$

Through feedback control, the eigenvalues can be moved into the unit circle, as can be seen in Figure 3.8. One problem with the feedback control, is that it is incapable of controlling position well. This is because the system cannot measure position reliably in an actual system (so position measurement is not attempted in this study), and because the system is time-varying. Unable to measure position, the system must integrate its velocity measurements to maintain position, and this operation has a steady state offset that prevents position tracking. Additionally, the time-varying nature of the system begs for a time-varying controller, as a time-invariant controller periodically applies control opposite of that which would drive the vehicle in the intended direction. The controller works on average, but there is a periodic error that manifests itself in a secular vehicle motion. Otherwise, it works fine.

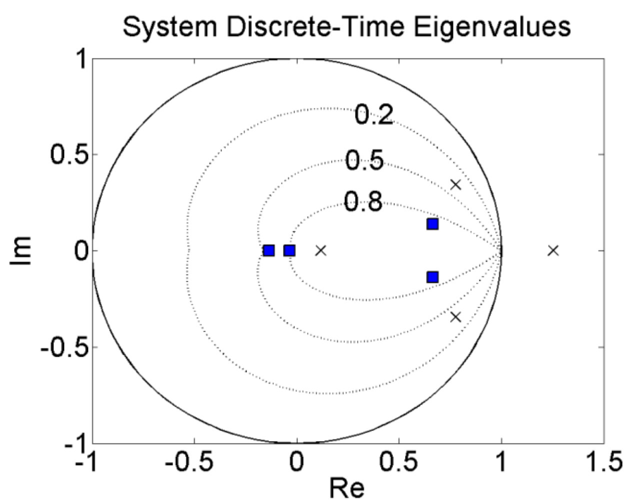

Figure 3.8 - Floquet multipliers are plotted in the z-plane, x-uncontrolled, boxes-controlled.

5. Transitional Trajectory Generation

The simplest method is to switch the control parameters from one trajectory's controller to another's. If the new trajectory's basin of attraction contains the states of the previous trajectory, the system will stabilize at the new trajectory. In essence, it will be sucked in. In order to accomplish this, certain continuity issues must be addressed.

The wingbeats must remain continuous and continuously differentiable to the third derivative. This is so that the jacobians of the trajectory can be calculated, which are a function of the wingbeats. This works by blending two wingbeats together using an appropriate mixing function. We use the mixing function described in [21], but adapted for the necessary derivative continuity.

An additional layer of control can be used in hover to stabilize the position states. When the hovering controller is activated, the altitude is fed into the controller to maintain position. The horizontal position, however, is not feasibly obtained, and thus it is not used.

A second method for generating a transitional trajectory can be used if the initial conditions are not within desired trajectory's basin of attraction. In this method, a set of intermediate stable trim trajectories are precalculated. The system is switched from one trajectory to another and allowed to settle before switching to another trajectory closer to the final desired trajectory.

5.1. Transition Trajectory Through Feedback Control

The first method to transition between forward flight and hover is by switching controllers abruptly and allowing the vehicle to settle to the new equilibrium. At a designated time, the vehicle's reference trajectory $\mathbf{x}^*(t)$ and feedback control law are switched from a forward flight trajectory to a hover trajectory. At the time $t=0^+$ an error between the actual trajectory $\mathbf{x}(0^+) = \mathbf{x}^*(t)_{forward}$ and the desired trajectory $\mathbf{x}^*(t)_{hover}$ begins. The error is equal to $\mathbf{x}^*(t)_{forward} - \mathbf{x}^*(t)_{hover}$. If this error lies within the basin of attraction of the control system, then the ornithopter should achieve a stable hovering flight.

In simulation, the system was capable of transitioning between the forward flight trajectory and the hover trajectory. Due to the robustness of the stabilizing controller, the system easily found the desired equilibrium from a high speed forward flight using nothing but a simple feedback control law. The speed abruptly decreased and settled to its near-still hover in a few seconds (Figure 3.9). Figure 3.10 shows the states of the vehicle converging to the desired hover. Note how the pitch Θ of the vehicle gradually increases so that the ornithopter moves from horizontal to nearly vertical during the maneuver. Also, the forward speed *U* dropped quickly. The system had a 1.01 *s* rise time, and it took 4.41 *s* to settle within 2% of the final value.

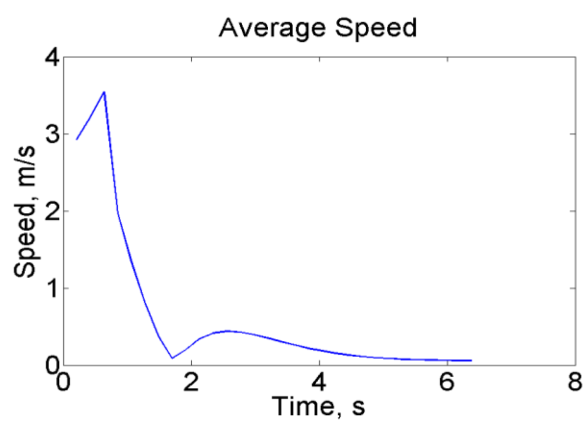

Figure 3.9 - Average vehicle speed during fast transition.

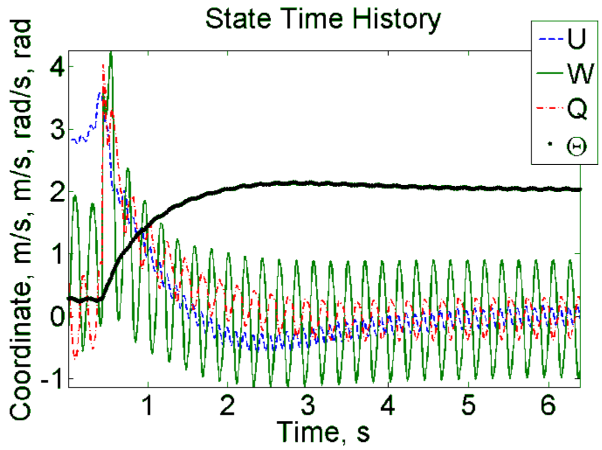

Figure 3.10 - Vehicle pitch during fast transition.

Figure 3.11 shows the position of the c.g. during the flight. During the transition, the vehicle moved 1.75 *m* horizontally, and 0.27 *m* downward, a total movement of 1.77 *m*. The altitude loss was minimal from where the maneuver began, so that the ornithopter would remain mere meters from where it was when the maneuver started. The hover feedback controller is switched on at point *a*. The immediately changes its course and by point *b* it is in a recognizable hover. This hovering trajectory continues to settle until the simulation is ended at point *c*.

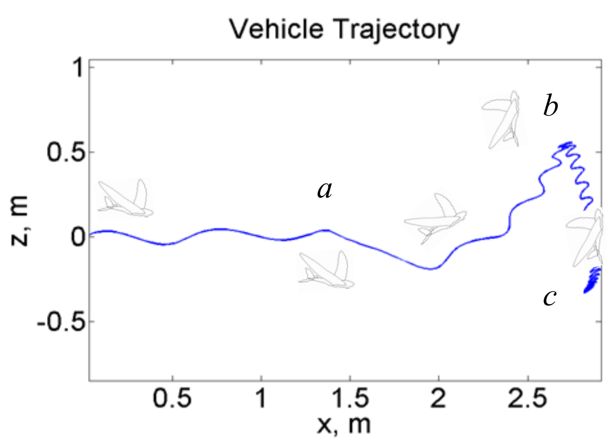

Figure 3.11 - Vehicle c.g. trajectory during feedback-controlled transition.

5.2. Optimal Path Planning

5.2.1. Optimization Problem Setup

The object of the path planning algorithm is to connect the two predetermined trajectories. Both trajectories (forward flight and hover) are limit cycles in the dynamic states x = [U, W, Q, θ]. Thus, during a forward flight trajectory, the states are periodic, e.g. $U(t + 1/f) = U(t)$. (A more complete discussion of the behavior of ornithopters in steady-state trajectories can be found in [14, 15]) During a transition between these limit cycles, however, the states are not periodic.

5.2.2. Fixed-Time Optimization

This work employs a discrete-time terminal constraint optimization. The terminal constraint for this problem is that the dynamic states of the vehicle must achieve a predetermined initial value for a hovering trajectory. Thus, with both initial and terminal constraints, the problem is to find control values that connect them while minimizing a cost function. The cost function employed here is to minimize the distance traveled during the transition.

$$J = a_1\left[x(t_f) - x(t_0)\right]^2 + a_2\left[z(t_f) - z(t_0)\right]^2 \tag{35}$$

The terminal constraint is to make the states of the vehicle equal to the states in the hovering limit cycle at the appropriate time: $\mathbf{x}_f = \mathbf{x}^*(0)_{hover}$. The terminal constraint is:

$$\psi\left[x(t_f)\right] = \mathbf{x}(t_f) - \mathbf{x}_f = 0 . \tag{36}$$

The terminal constraint is evaluated at a set final time. This is computationally simple.

In order to employ a discrete-time algorithm, it is necessary to discretize the system. Ornithopter flight is described by differential equations, but it is not a difficult matter to model the flight dynamics in the discrete domain over short time increments. The time of flight from $t_0 = 0$, until $t_f = N/f$ is divided into N time increments. For each period, a discrete-time mapping can be generated:

$$\mathbf{x}(i+1) = \mathbf{f}_d\left[\mathbf{x}(i), \mathbf{u}(i), i\right] \tag{37}$$

The discrete mapping is computed by integrating the system's nonlinear differential equations for the duration of time corresponding to the discrete interval:

$$\mathbf{f}_d\left[\mathbf{x}(i), \mathbf{u}(i), i\right] = \int_{t_i}^{t_{i+1}} \mathbf{f}\left[\mathbf{x}(t), \mathbf{u}(t), t\right] dt + \mathbf{x}(t_i) \,. \tag{38}$$

The control vector consists of the wing twisting amplitude $C_t(i)$ and elevator deflection $\delta_e(i)$.

$$\mathbf{u}(i) = \left[C_t(i), \delta_e(i)\right]^T \tag{39}$$

These controls are both zero order holds:

$$\mathbf{u}(t) = \mathbf{u}(i),\ t_i \le t < t_{i+1} \tag{40}$$

The initial condition is the states of the ornithopter at the end of a forward flight flapping cycle:

$$\mathbf{x}(0) = \mathbf{x}_0 \tag{41}$$

The solution for this optimization problem—Bryson names it *Discrete OPtimization with Constrains* (DOPC)—is detailed in [22]. It is a gradient search in the space of allowable controls during every step of the transition flight. Using the Jacobians of the discrete mapping, the algorithm can find the optimal path.

6. Optimization Result

6.1. Fixed-Time Optimization

Figure 3.12a limns three ornithopter trajectory solutions to the optimization problem with the transition starting at time t = 0 and position (x,z) = (0,0). Each has a different set final time (equal to the times of 3, 4, and 5 flapping periods). From the beginning of the transition to the end, the vehicle c.g. moves approximately 1 meter. At 3-period trajectory there is a greater altitude loss than at the other trajectories. Figure 3.12b shows the pitch angle and forward speed vs. time for those same trajectories. In each of these transitions, there is an abrupt pitch-up maneuver while the forward speed decreases quite rapidly (which is related to the pitch-up maneuver as the vehicle's forward speed vector also pitches up).

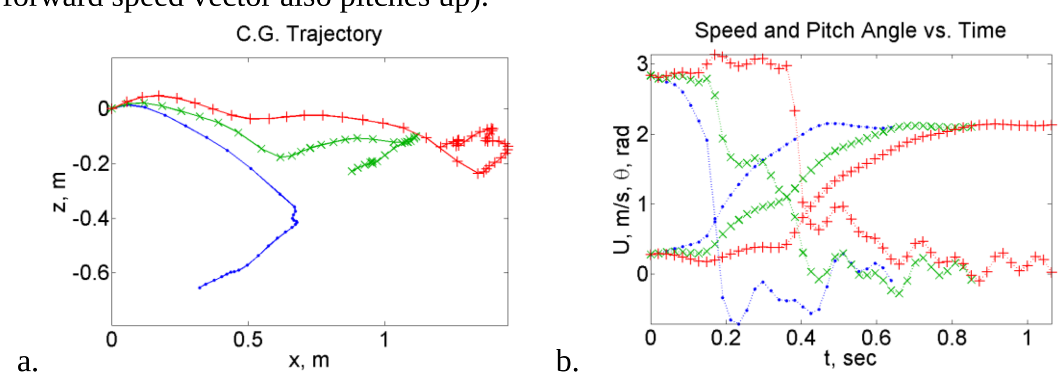

Figure 3.12 - a. C.G. trajectory and b. Forward speed and pitch angle of the ornithopter during optimal trajectories. • 3 flapping cycles, × 4 flapping cycles, + 5 flapping cycles.

6.2. Feedback Control and Optimal Trajectory

Here follows an example transition trajectory, achieved in a span of 2 flapping cycles. The trajectory was divided into 4 control operations per flapping cycle and The open-loop transition trajectory was generated using a MATLAB script. Figure 3.13a shows the dynamic states during the entire cycle. At first there is a stable forward-flight trajectory. At time $t \sim 2s$ the transition begins. In the two flapping cycles (which has the same frequency as the oscillations in the dynamic states before and after the transition) the pitch of the vehicle increases abruptly and the speed of the vehicle begins a steep decline. At the end of the transition, the hovering flight control mode is activated and the trajectory is stabilized.

The vehicle's c.g. trajectory is shown in Figure 3.13b. The trajectory begins at the origin and moves horizontally until the transition begins. During the motion, the vehicle abruptly changes direction and begins a stable trajectory centered around a point ~1.5*m* away from the beginning of the transition. The motion includes an abrupt pitch up motion with steep speed decline; it actually looks like a stalled pitch up maneuver. The vehicle, however, is not stalled because the flapping wings generate a

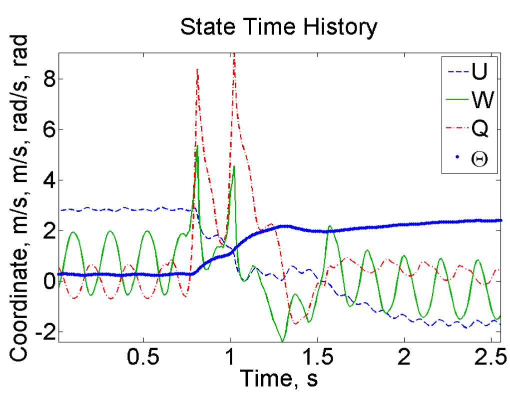

a.

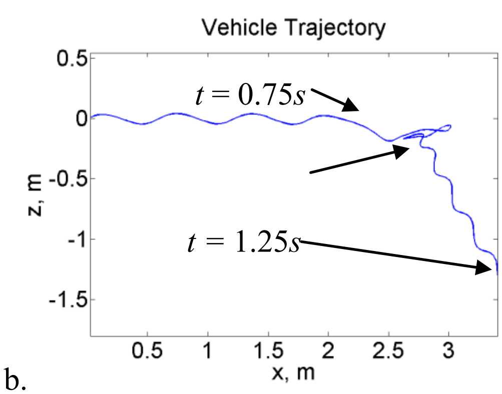

b.

Figure 3.13 - a. Vehicle states during the transition trajectory. b Vehicle c.g. trajectory during the transition flight.

new circulation pattern during every stroke, and the hovering trajectory is stabilized. The trajectory-generating algorithm penalized a drift in position during the transition, but there remains a finite slide.

Figure 3.14 shows the total speed of the vehicle during the transition flight. At first, during the transition, there is a small jump in speed, but this quickly decreases. At the termination of the transition, the speed settles to the low steady-state of the hovering limit cycle.

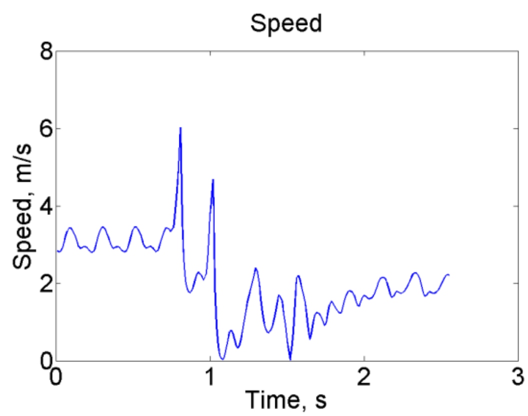

Figure 3.14 - Total speed during transition trajectory.

7. Conclusion

To design trajectories connecting two trim conditions is quite achievable. The ornithopter transition flight problem has been described and demonstrated in simulation, both using feedback control for flight stabilization and using a fixed-time horizon dynamic optimization. The optimal trajectories and the feedback controlled trajectories both featured a pitching up maneuver where the ornithopter slows in flight and changes its orientation in space from horizontal to vertical.

The design envelope for ornithopters has been effectively widened. With these design and analysis tools, ornithopter design is greatly helped and ornithopters can begin to achieve aerodynamic feats heretofore only glimpsed in the natural world.

REFERENCES

[1] A.M. Wickenheiser, E. Garcia, M. Waszak, Evaluation of bio-inspired morphing concepts with regard to aircraft dynamics and performance, *Proc. SPIE* **5390** (2004) 202-211.

[2] C.P. Ellington, The Aerodynamics of Hovering Insect Flight. I. The Quasi-Steady Analysis, *Phil. Trans. R. Soc. Lond. B.* **305** (1984) 1-15.

[3] C. Van den Berg, C.P. Ellington, The Three-Dimensional Leading-Edge Vortex of a 'Hovering' Model Hawkmoth, *Phil. Trans. R. Soc. Lond. B.* **352** (1997) 329-340.

[4] M.H. Dickinson, F.O. Lehmann, S.P. Sane, Wing Rotation and the Aerodynamic Basis of Insect Flight, *Science* **284(5422)** (1999) 1954-1960.

[5] J.D. DeLaurier, An Aerodynamic Model for Flapping-Wing Flight, *Aeronaut. J.* **April** (1993) 125-130.

[6] A. Cox, D. Monopoli, D. Cveticanin, M. Goldfarb, E. Garcia, The Development of Elastodynamic Components for Piezoelectrically Actuated Flapping Micro-Air Vehicles, *J. Intell. Mat. Syst. Str.* **13(9)** (2002) 611-615.

[7] T. Theodorsen, General Theory of Aerodynamic Instability and the Mechanism of Flutter, *NACA Technical Report* **496** (1935).

[8] R.T. Jones, The Unsteady Lift of a Wing of Finite Aspect Ratio, *NACA Technical Report* **681** (1940).

[9] Z.J. Wang, Dissecting Insect Flight, *Ann. Rev. Fluid Mech.* **37** (2005) 183-210.

[10] G. Berman, Z.J. Wang, Energy-minimizing kinematics in hovering insect flight, *J. Fluid Mech.* **582** (2007) 153-168.

[11] L. Schenato, X. Deng, S. Sastry, Flapping Flight for Miomimetic Robotic Insects: Part II—Flight Control Design, *IEEE T. Robot.* **22(4)** (2006) 789-803.

[12] G.K. Taylor, M. Bacic, R.J. Bomphrey, A.C. Carruthers, J. Gillies, S.M. Walker, A.L.R. Thomas, Insect Flight Dynamics and Control, *J. Exp. Biol.* **211** (2008) 258-266.

[13] P. Zdunich, D. Bilyk, M. MacMaster, D. Loewen, J. DeLaurier, R. Kornbluh, T. Low, S. Stanford, D. Holeman, Development and Testing of the Mentor Flapping-Wing Micro Air Vehicle, *J. Aircraft* **44(5)** (2007) 1701-1711.

[14] J.M. Dietl, E. Garcia, Stability in Ornithopter Longitudinal Flight Dynamics, *J. Guid. Contol Dynam.* **31(4)** (2008) 1157-1162.

[15] J.M. Dietl, E. Garcia, Stability in Hovering Ornithopter Flight," *Proc. SPIE* **6930** (2008) 69300N.

[16] A.M. Wickenheiser, E. Garcia, Optimization of Perching Maneuvers Through Vehicle Morphing, *J. Guid. Contol Dynam.* **31(4)** (2008) 815-823.

[17] March, C. Bradley, E. Garcia, Aerodynamic Properties of Avian Flight as a Function of Wing Shape, *ASME IMECE* **2005-83011** (2005).

[18] MATLAB, Software Package, Ver. 7.2.0.232, Copyright 1984-2007, The MathWorks, Inc.

[19] J.M. Dietl, E. Garcia, Ornithopter Flight Maneuver Control, ASME SMASIS2009, September 21-23, (2009) Oxnard, CA.

[20] K. Ogata, *Discrete-Time Control Systems, second ed.*, Pearson-Prentice Hall, Englewood Cliffs, New Jersey, 1995, pp. 315.

[21] J.H. Lee, M.S. Kim, Pseudo dynamic keyframe animation with motion blending on the configuration space of a moving mechanism, Proc. Pacific Graphics '95, Seoul, Korea, August 21-24 (1995) 118-132.

[22] A.E. Bryson, *Dynamic Optimization*, Addison-Wesley, Menlo Park, CA, 1999, pp. 93-102.

CHAPTER 4

DYNAMIC MODELING, TESTING, AND STABILITY ANALYSIS OF AN ORNITHOPTIC BLIMP[1]

1. Abstract

A flapping-wing blimp is designed and constructed from mylar plastic and balsa wood as a test platform for ornithopter aerodynamics and flight dynamics. The blimp, 2.3 meters long and with 420 gram mass, is propelled by flapping wings. Due to buoyancy the wings have no lift requirement so that the distinction between lift and propulsion can be analyzed in a flight platform. The blimp is tested using a Vicon motion tracking system and various initial conditions are tested. Test results are used to estimate parameters in a coupled quasi-steady aerodynamics/Newtonian flight dynamics model. This model is then analyzed using Floquet theory to determine dynamic modes and stability. It is concluded that the dynamic model is valid for a buoyant vehicle and that the vehicle's modes are akin to a fixed-wing aircraft.

2. Introduction

Flapping wings were the first successful aircraft design. Millions of years before the creation of the airplane, insects, pterosaurs, and birds had flown above their terrestrial cousins. Engineers, from the fabled Daedalus to Leonardo da Vinci [1], had attempted to duplicate the feats of biology with flapping wings for centuries before the first

---

[1]From Dietl, J. M., Herrmann, T. A., Reich, G., and Garcia, E., "Dynamic Modeling, Testing, and Stability Analysis of an Ornithoptic Blimp," submitted to the *Journal of Bionic Engineering*.

successful airplane flight by the Wright Brothers in 1903. Subsequent efforts at flight with flapping wings were largely abandoned by the burgeoning aerospace engineering industry in favor of the Wrights' fixed-wing design, which offered greater simplicity, ease of use, payload capacity, and speed. Nevertheless, ornithopters continued to be studied and built by hobbyists and aircraft designers throughout the twentieth century through trial and error. Recently, the demand for highly maneuverable micro air vehicles has driven a resurgent ornithopter research.

Flapping wing aerodynamics has been studied by several groups over the last three decades. A seminal contribution was from Ellington in his study of insect flight [2]. These papers used high speed flow visualization of a wing mounted to a rotor to document some of the aerodynamic peculiarities in flapping flight. Among these is the leading edge vortex (LEV), an unstable vortex which forms on the upper surface of a flapping wing. The LEV temporarily increases the total circulation around the wing section, thereby increasing the lift force. During each flapping motion a new LEV is formed and shed. Other aerodynamic effects found were some spanwise flow velocity, which may be responsible for vorticity intensification.

Later, Dickinson et al. [3] performed experiments on dimensionally similar insect wings using an oil-tank apparatus. This system allowed them to visualize the flow over flapping wings in on oscillatory motion and capture detailed force measurements. Wang developed a 2-D CFD model capable of capturing the LEV effect on those wings, and fit a quasi-steady model to the experimental data and CFD 'data' [3]. These models were subsequently used to model the flight of insects with 1 and 2 pairs of wings [5].

Much of the elements of flapping wing aerodynamics is derived from the work of engineers studying wing flutter in fixed-wing aircraft. Theodorsen [6] and Jones [7] developed aerodynamic theories to account for the unsteady motion of the wings. They were cited by DeLaurier [8] in his development of a full aerodynamic model for an ornithopter capable of carrying a human pilot. This vehicle was designed to accelerate on a runway and take off as a conventional fixed-wing airplane. Since the vehicle has a significant advance ratio (the ratio of forward velocity to wing flapping velocity), the angle of attack is not as extreme as that found in insect flight and the fluttering-wing adaptation of fixed-wing aerodynamics was determined to be appropriate.

In order to build a better ornithopter, it is necessary to understand the mechanisms of flapping flight. Flapping wings, through a complicated interaction between flexible structures and time-varying aerodynamics, produce both the lift and thrust necessary to sustain flight. Thus, flapping flight is difficult to understand. Even birds' evolutionary instinct could not help design a working ornithopter—in a human analog, we can barely make a robot walk in a way that resembles a human gait—but we can rely on science, mathematics, and engineering to design a working ornithopter. Among the tools of scientific analysis and engineering design is the process of reducing each problem to smaller elements so that the entirety of each element may be more totally understood. In a standard heavier-than-air ornithopter, it is not possible to segregate the lifting and thrusting functions of flapping wings. But a buoyant ornithopter does not have this problem.

This paper documents the design of such a flapping-wing blimp, and then the use of the blimp for aerodynamic modeling, flight testing, and dynamic analysis.

Figure 4.1 - The Cornell Ornithoptic Blimp.

3. Design and Construction

The Cornell Ornithoptic Blimp (Figure 4.1) is an electrically-powered, helium-filled dirigible, controlled entirely by flapping wings. Its length is 2.3 m, diameter 0.6 m. Each wing has length is 67 cm and maximum chord 14 cm. The vehicle's total mass is 420 g and each wing is 14 g. It is powered by a 3 cell Li-Po, 250 mAh battery and controlled through a radio transmitter at 2.4 GHz.

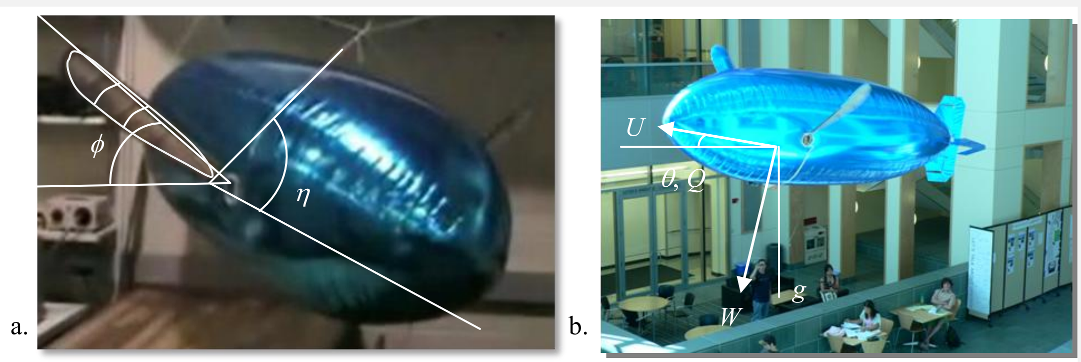

Figure 4.2 - Ornithopter variable diagrams. a. Wing angles, b. Dynamic variables.

The body of the blimp is a hollow mylar bag. It has no structural reinforcement except for the horizontal spar structure on which the wings are mounted. The electronics are taped to the bottom of the structure and the tail is attached to the rear.

The pair of wings flap symmetrically in 2 degrees of freedom: plunging (or heaving) $\phi(t)$ and the twisting $\eta(t)$ (Figure 4.2a). Although the interaction between the wing movement and the aerodynamic forces is complex, these two motions broadly correspond to two separate functions. The plunging motion's main function is to generate velocity while the twisting motion uses that velocity to produce vectored aerodynamic forces on the wing. Either of these motions acting alone would produce no thrust, but when working in concert can produce enough thrust (and lift) to control the vehicle.

$$\phi(t) = \mathrm{C_h} \cos(2\pi f t) + \phi_0 \tag{1}$$

$$\eta(r,t) = \mathrm{C_t} \cos(2\pi f t + \phi_{\eta 0}) \tag{2}$$

a. 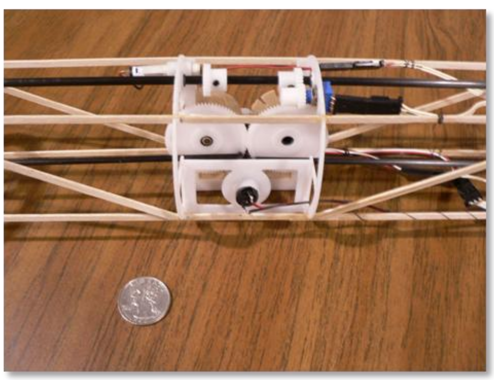 b. 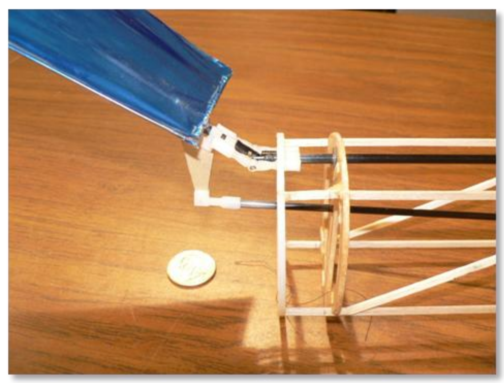

Figure 4.3 – a. Flapping mechanism. b. Joint connecting wing to central spar.

Plunging and twisting motions are produced by a mechanism in the central spar of the blimp (Figure 4.3a). The spar is constructed largely from balsa wood, but it contains several plastic components where precision and strength are emphasized. The moving parts are connected to those plastic parts. There is a central motor that drives the plunging motion, at a speed controlled by the radio transmitter. This motor drives a slider-crank mechanism that sweeps the wings. A second motor twists the shaft on which the wings are mounted. This motor is controlled by the microcontroller circuit, which is synchronized to the plunging motion with an optical encoder. The wings are attached to two shafts (Figure 4.3b). The lower shaft drives the plunging motion, moving outward and inward. The upper shaft drives the twisting motion and supports the wing joint. The wing attaches to the upper shaft through a universal joint, and the wing's shaft is constrained by a journal bearing affixed to a pin joint. This allows the shaft to transmit torque to the plunging wing without the system binding.

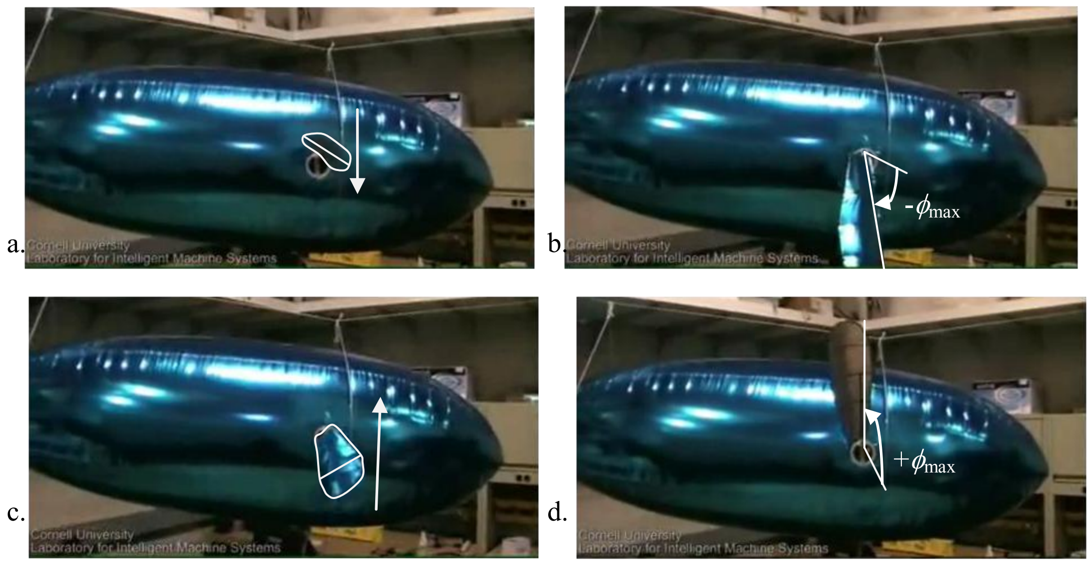

Figure 4.4 - Wing flapping motions for forward flight, with wings highlighted to indicate stroke direction. a. Downstroke, b. Bottom of stroke, c. Upstroke, d. Top of stroke

The central spar then generates a flapping motion that is conducive for forward motion. Figure 4.4 shows the basic pattern. During the downstroke (Figure 4.4a) the wing has a negative absolute angle of attack, but when combined with the downward plunge there is a positive lift. The lowered wing pitch also serves to direct the lift forward to create propulsion. At the bottom of the stroke, the wing twists toward a positive angle of attack (Figure 4.4b). On the upstroke (Figure 4.4c), the wing has a positive pitch angle in order to generate a lift on the bottom surface of the wing. This is called negative lift because it serves to pull the vehicle downward. The positive pitch angle also directs the lift forward. Finally, at the top of the stroke the wing twists downward again to begin another stroke (Figure 4d).

The flapping motion's frequency is controlled by the radio controller, and the twisting motion is synchronized using an Atmel ATmega32 microcontroller. The controller can be programmed with a variety of wing twisting amplitudes.

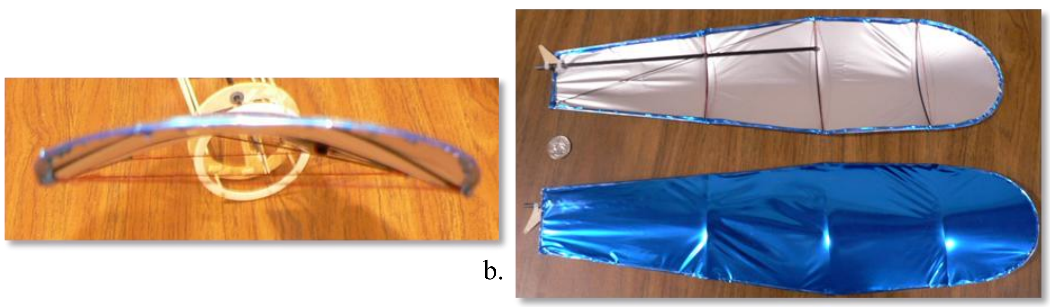

a. b.

Figure 4.5 - Cambered wings. a. End view. b. Top view.

Each wing is a cambered thin airfoil useful for low speed aerodynamics (Figure 4.5). They are connected to a rigid central spar that contains the flapping mechanisms, motors, and control sensors. These wings are not significantly flexible at the speed and frequency at which they are operated. This simplifies the analysis.

4. Dynamic Modeling

The vehicle's aerodynamics are well characterized by quasi-steady approximations to the forces on the wings and body. The quasi-steady model was chosen as the most convenient of several options: computational fluid dynamics, the vortex-panel method, and quasi-steady strips. Both of the other methods require more computational time, and their increased sophistication makes programming them more difficult. In the quasi-steady method formulas for lift and drag are validated to some experimental or computational information, but the validation is not repeated during flight simulation. To calculate the forces on the wings, each wing is divided into spanwise strips. Each strip's velocity, acceleration, rotation rate, and rotational acceleration are calculated in the local frame of reference. The aerodynamic forces on each strip are calculated in this frame of reference, and these forces are summed over the span of each wing to provide a resultant force from the wings. The manner of the quasi-steady aerodynamic model is also limned in [9] and [10].

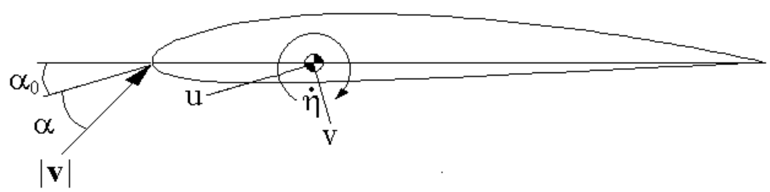

Figure 4.6 - Airfoil section showing aerodynamic variables.

Each strip has two calculated forces and a moment based on the aerodynamic velocities and accelerations (Figure 4.6):

$$dF_u(r,t) = \left\{ \left[\frac{\mathrm{m_w} c(r)}{\bar{c}} + \mathrm{m}_{22} \right] \frac{r}{\mathrm{R}} v\dot{\eta} - \rho r v \Gamma - \mathrm{m}_{11} \frac{r}{\mathrm{R}} \dot{u} \right\} dr - dF_{v_u}(r,t) \tag{3}$$

$$dF_y(r,t) = \left\{ -\left[\frac{\mathrm{m_w} c(r)}{\bar{c}} + \mathrm{m}_{11} \right] \frac{r}{\mathrm{R}} u\dot{\eta} + \rho r u \Gamma - \mathrm{m}_{22} \frac{r}{R} \dot{v} \right\} dr - dF_{v_y}(r,t) \tag{4}$$

$$d\tau(r,t) = \left[(\mathrm{m}_{11} - \mathrm{m}_{22}) \frac{r^2}{\mathrm{R}} vu - \mathrm{I_a} \frac{\ddot{\eta}}{\mathrm{R}} + \frac{c(r)}{4} \rho v \Gamma \right] dr - d\tau_v(r,t) \tag{5}$$

The drag forces, $d\boldsymbol{F}_v$ and moments $d\tau_v$ are computed as though the wings were a flat plate, where the drag coefficient is a mix of drag at zero angle of attack and 90 degree angle of attack. The terms m_{11} and m_{22} are added mass coefficients. They represent the temporary pocket of air mass that must be accelerated with each stroke of the wing. A more detailed simulation would require the air itself to be modeled as a number of increased dynamic states, requiring a differential equation to model the aerodynamics. However, this formulation assumes that the instantaneous velocities and accelerations of the wings are sufficient information on which to calculate forces.

$$d\mathbf{F}_v(r,t) = \rho r c(r)|\mathbf{v}|\{\mathrm{C_D}(0)\cos^2\alpha + \mathrm{C_D}(\pi/2)\sin^2\alpha\}dr\begin{bmatrix} u \\ v \end{bmatrix} \tag{6}$$

The circulation term Γ has two monomials. The first is a circulation proportional to the velocity of the airfoil. This term has analogs in the standard circulation term in a lifting line analysis. The second term is a circulation proportional to the rotation rate of the airfoil. This does not typically appear in the aerodynamics of fixed-wing aircraft, but it provides a good approximation of the effects of unsteady movements on an ornithopter wing [10].

$$\Gamma(r,t) = -2\mathrm{C_L}c(r)\frac{uv}{|\mathbf{v}|} + 2\mathrm{C_R}c(r)^2\dot{\eta} \tag{7}$$

Once the forces on the wings are rotated into the proper frame of reference, they can be summed over the entire wing length. These forces are applied to the vehicle dynamics equations, the Euler-Bernoulli equations of motion for rigid bodies.

$$\mathbf{F} = \mathrm{m}\left.\frac{d\mathbf{v}_c}{dt}\right|_B + \mathrm{m}(\boldsymbol{\omega}\times\mathbf{v}_c) \tag{8}$$

$$\mathbf{M} = \left.\frac{d\mathbf{H}}{dt}\right|_B + \boldsymbol{\omega} \times \mathbf{H} \tag{9}$$

The main concern of this study is the longitudinal dynamics of the blimp. Therefore, it simplifies matters to reduce the equations of motion to only the number needed for longitudinal dynamics. Thus the lateral position and velocity, the yaw and roll angles and their rates can be safely ignored. Equations (8) and (9) have twelve degrees of freedom, but in the longitudinal dynamics case can be reduced to four dynamic states and two positions.

The forward velocity in the body frame of reference is $U(t)$ (Figure 4.2b). This velocity is the velocity of the fuselage along the horizontal fuselage reference line. The downward velocity $W(t)$ is perpendicular to the forward velocity. The pitch angle $\theta(t)$ is the angle of the fuselage reference line above horizontal. Its derivative is the pitch rate $Q(t)$. The gravitational constant g is shown as a reference to the vertical direction.

The aerodynamic forces and moments on the vehicle are represented by the terms $F_U(t)$, $F_W(t)$, and $M(t)$, which include the coupled dynamic forces of the wings. The position of the vehicle is tracked by two further differential equations which integrated the velocity of the vehicle; $x(t)$ is the absolute position in the horizontal direction, and $z(t)$ is the position vertically.

$$\dot{U} = -QW - \mathrm{g}\sin\theta + F_U(t)/\mathrm{m} \tag{10}$$

$$\dot{W} = QU + \mathrm{g}\cos\theta + F_W(t)/\mathrm{m} \tag{11}$$

$$\dot{Q} = M(t)/\mathrm{I_y} \tag{12}$$

$$\dot{\theta} = Q \tag{13}$$

$$\dot{x} = U\cos\theta + W\sin\theta \tag{14}$$

$$\dot{z} = U\sin\theta - W\cos\theta \tag{15}$$

These are nonlinear equations of motion, due to the presence of rotational dynamics and the coupling to the aerodynamic forces. Because of the time-varying nature of the equations and their nonlinearity, numerical simulation provides the only known solution. This is accomplished using MATLAB software and its *ode45.m* Runge-Kutta algorithm. Another feature of these equations is that they implicitly contain their derivatives: that is, the accelerations are contained in the aerodynamic force equations, so that they must be solved algebraically for the accelerations before each time step. During a steady flight, all the terms except the secular x and z should become periodic. Since the other variables are not dependent on x and z in any way, they are free to drift.

5. Flight Testing

Flight tests were conducted at the μAviari, a micro air vehicle indoor testing facility at the Air Force Research Laboratory Air Vehicles Directorate. Part of this facility is a darkened room, large enough for forward flights on the order of tens of seconds, equipped with a Vicon motion capture system (Figure 4.7). The Vicon system used 53 cameras to sample the locations of reflective markers installed on the blimp body and flippers at approximately 50 Hz with 0.1mm resolution in space. Velocities are calculated through finite difference differentiation of filtered data. For each rigid body, the system must acquire at least four points to locate the vehicle's position and orientation. The system then uses the point date from those four points to store the position and orientation of the rigid body's reference point. Although there are redundant cameras in the test chamber, the marks can be obscured by moving objects (or the object itself), so it is reasonable to use more than four data locations. Each wing was also fitted with markers so that the wing motion variables could be reconstructed.

Since the markers each look identical to the sensing system, the system relies on them remaining in a rigid configuration to be able to recognize the rigid body they represent. This required the blimp to be refilled with helium every few minutes, since as it lost volume its shape changed enough to confuse the sensing system. Also, although it was anticipated that the reflective body of the blimp might interfere with the sensors, the Vicon system effectively recognized its markers.

Several types of dynamic tests were performed, including acceleration from standstill, deceleration from a velocity excitation, and pitch excitation (Figure 4.8). In the acceleration from standstill test, the blimp's flapping motion was activated at zero velocity and then released with no force. For the deceleration test, the blimp's flapping motion was activated and then released with more velocity than the blimp's trim velocity. In the pitch excitation test the blimp was accelerated to a steady forward velocity, at which point it was bumped from above (near the tail) to induce a pitch disturbance. For several seconds, the blimp would oscillate while continuing to fly forward.

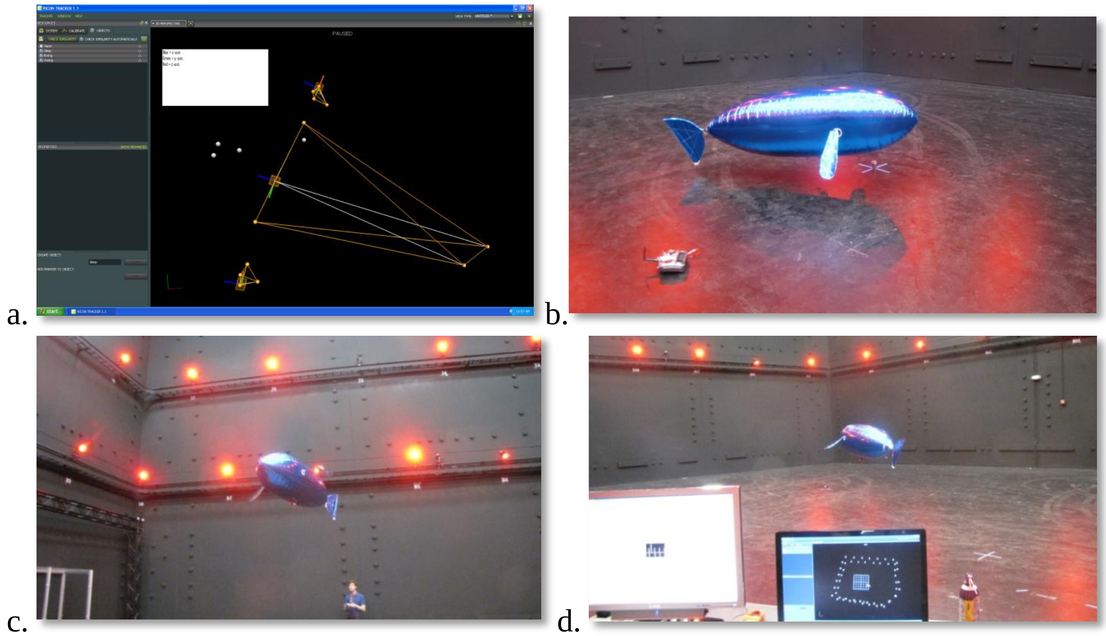

Figure 4.7. Flight testing at the AFRL μAviari. a. Monitor screen showing the rigid body tetrahedrons tracked by the Vicon system, b. The blimp on the ground with radio transmitter, c. The blimp in flight lit by the Vicon system, d. Computer monitors used for controlling the sensor system.

There were no tests concerning control surface disturbances, since the elevator was removed. The system was allowed to oscillate freely. Altitude was controlled by changing the mean wing twist angle, so that the direction of thrust could be controlled. This was done using the radio controller. However, there were no control perturbations during the dynamic tests.

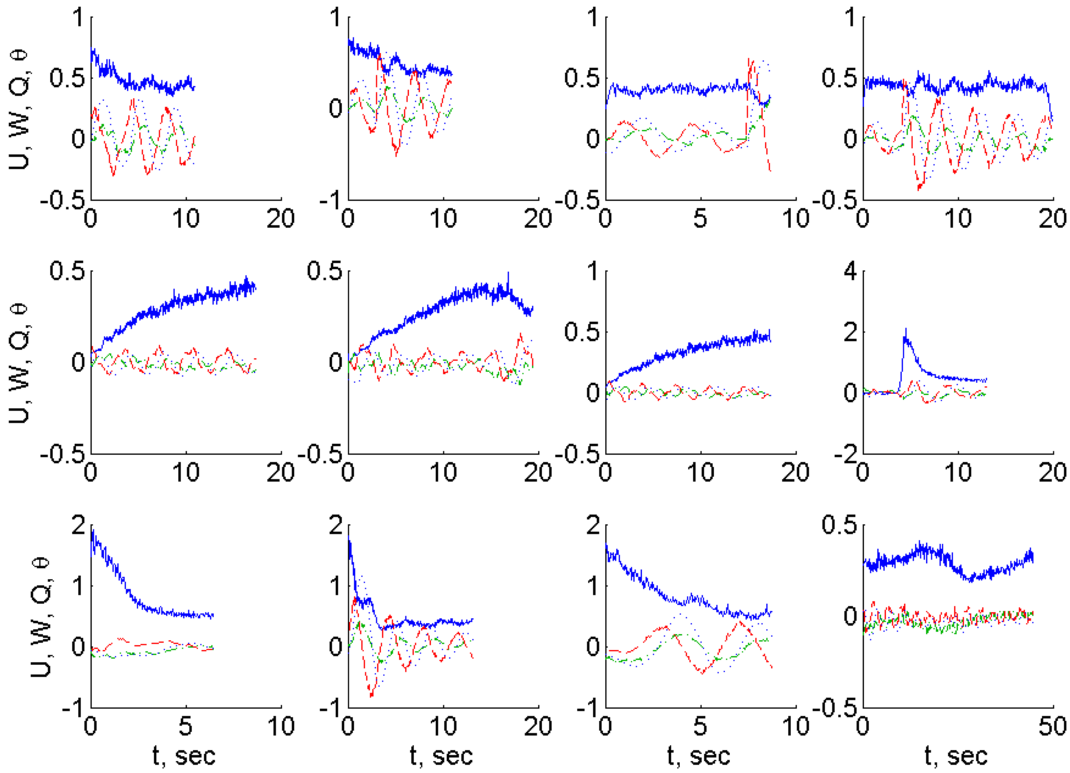

Figure 4.8 - Raw data from the Vicon system. Each chart shows the vehicle's dynamic states during one dynamic test. U (m/s) —— , W (m/s) -·-·-, Q (rad/s) - -, θ (rad) ····

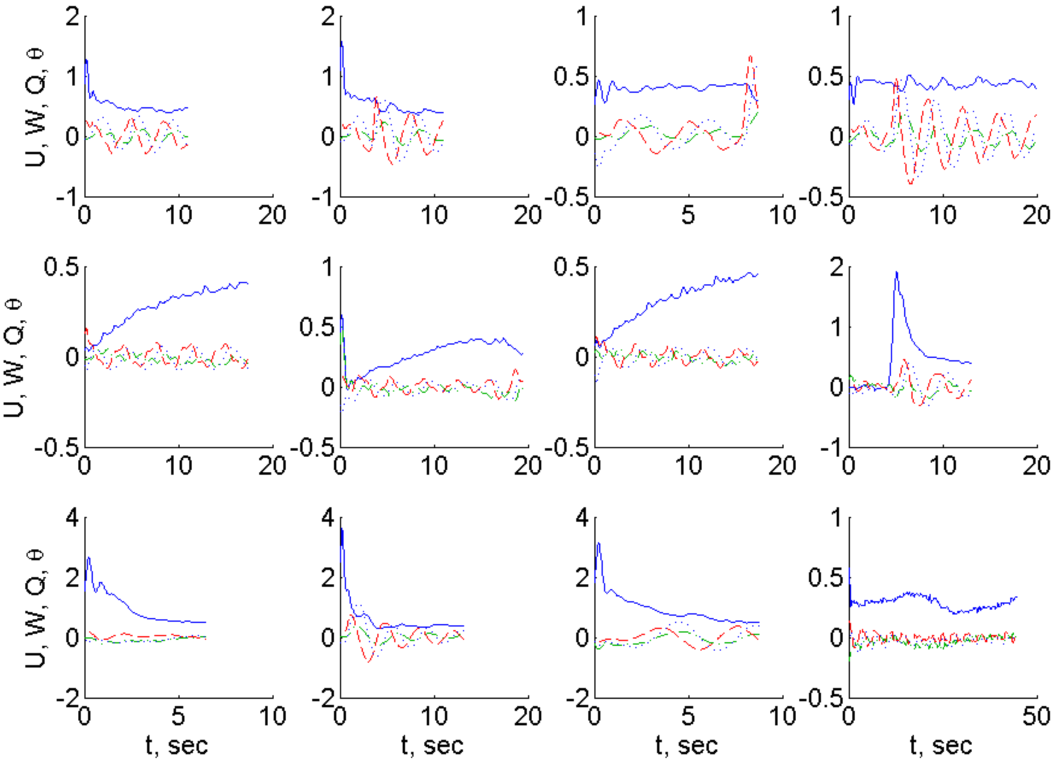

Figure 4.9 - Filtered Vicon data. Each chart shows the vehicle's dynamic states during a dynamic test. U (m/s) —— , W (m/s) ·—·—, Q (rad/s) - -, θ (rad) ····

6. Parameter Estimation

Using the flight dynamics data, it is possible to estimate the parameter values in equations (1-7). A nonlinear least squares estimator is used [11]. This method uses the filtered flight data (Figure 4.9) to iteratively improve the estimates of the unknown parameters. Through iteratively decreasing the error between the dynamic variables predicted over several time spans with varying initial conditions, the aerodynamic parameters can be more accurately ascertained.

Let the unknown parameters be collated into a vector $\mathbf{x}$, and let the current guess be $\mathbf{x}_i$. In our case, the unknown parameters are the vehicle's initial conditions at the beginning of each test and some unknown aerodynamic coefficients (such as m_{11}, m_{22}, and C_L). Using the current guess the simulation predicts the vehicle's time histories, $U(t,\mathbf{x}_i)$, $W(t,\mathbf{x}_i)$, $Q(t,\mathbf{x}_i)$, and $\theta(t,\mathbf{x}_i)$, for each test and these are collocated into a vector $\mathbf{h}(\mathbf{x}_i)$. The estimator cost is:

$$J = [\mathbf{z} - \mathbf{h}(\mathbf{x})]^T \mathbf{R}^{-1} [\mathbf{z} - \mathbf{h}(\mathbf{x})] \tag{16}$$

where $\boldsymbol{R}$ is a covariance matrix of the sensor noise. These simulated results are compared to the sensor readings $\boldsymbol{z}$. The guess is updated using the recursive formula (a Gauss-Newton solver to minimize the least-squares cost):

$$\mathbf{x}_{i+1} = \mathbf{x}_i + \left(\mathbf{J}_i^{\,T} \mathbf{R}^{-1} \mathbf{J}_i\right)^{-1} \mathbf{J}_i^{\,T} \mathbf{R}^{-1} [\mathbf{z} - \mathbf{h}(\mathbf{x}_i)] \tag{17}$$

where $\mathbf{J}_i$ is the Jacobian matrix of the measurement function with respect to the parameter vector $\mathbf{x}_i$.

Figure 4.10 shows the forward velocity U and pitch angle θ both from the test data and from the simulation. The velocity is shown filtered through an 8^{th} order Butterworth filter with a cutoff at 10 Hz to remove noise amplified by the finite difference differentiation. As the simulation is improved, several features of the simulated trajectory approach those seen in the data. Most prominently, the natural frequency and damping ratio of the pitching motion are well captured by the simulation. Forward velocity is harder to predict. The rocking motion of the vehicle is a somewhat straightforward dynamics problem. It is largely dependent only on the vehicle's geometry, mass, and moment of inertia, all of which are easily measured directly. Forward velocity is more thoroughly dependent on the flapping motion, including its subtleties in twist distribution, camber distribution, elastic deflection, and added mass parameters.

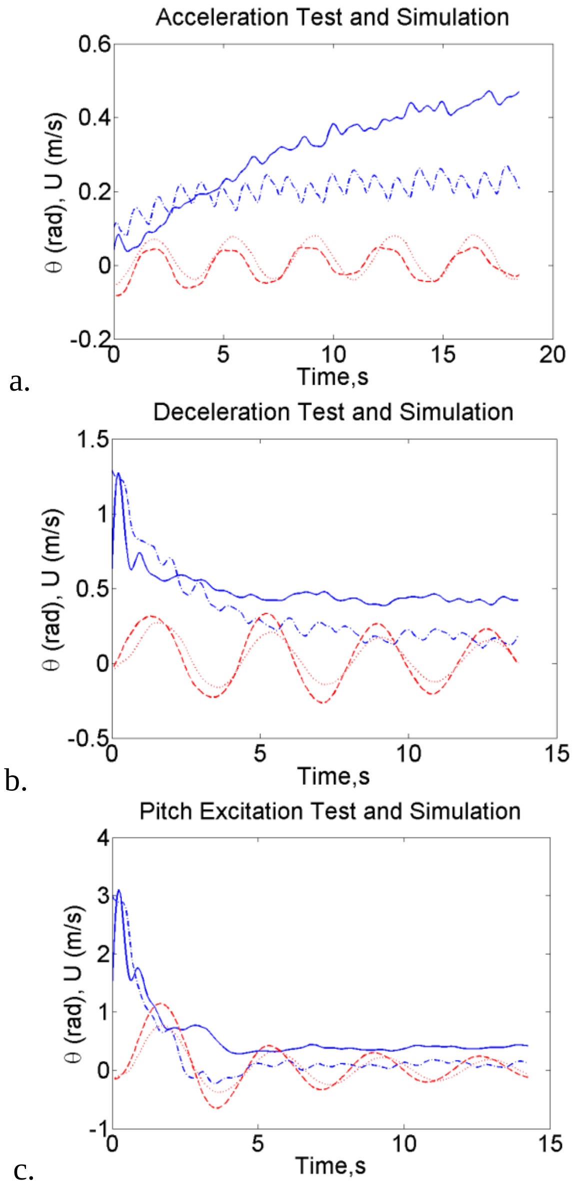

Figure 4.10 - Three plots showing the experimental data in 2 variables vs. the simulated outputs of those variables U (test) —, U (simulation) ·–·–, θ (test) – –, θ (simulation) ····. a. Acceleration test, b. Deceleration test, c. Pitch excitation test.

7. Analysis of the Dynamic System

Since the blimp has flapping wings, steady forward flight cannot be approximated as a steady state in dynamic variables. Oscillating forces on the wings cause the vehicle to experience periodic oscillations in its pitch and velocity. Therefore it is useful to analyze the flight as a limit cycle in the dynamic variables (velocity, pitch, and pitch rate), but not in the positional variables (horizontal and vertical distance). The analysis is helped by having foreknowledge of the limit cycle frequency, but some computational effort is required to produce a fuller trim analysis.

By defining trim as a limit cycle in the dynamic states, the system can be analyzed in the discrete-time domain. The Poincare map of the forward flight's limit cycle is a discrete-time mapping of the dynamic states from one period to the next (Figure 4.11). This mapping is time-invariant. By performing several mathematical operations, it is possible to construct a linearized model of trimmed flight, to analyze the system's stability, and to observe the dynamic modes [9].

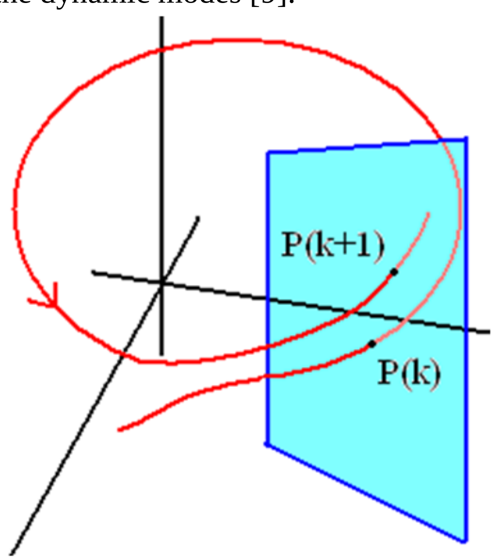

Figure 4.11 - A paradigmatic 3-dimensional phase space showing a plane which can be used to construct a Poincare map **P**.

For a general nonlinear system of ordinary differential equations

$$\dot{\mathbf{x}}(t) = \mathbf{f}[\mathbf{x}(t)], \mathbf{x} \in R^n \tag{18}$$

a limit cycle $\boldsymbol{x}^*(t)$ is a periodic solution of period T that satisfies (18). For the blimp, the dynamic state vector is $\mathbf{x} = [U, W, Q, \theta]^T$.

The Poincare map of the system is a discrete mapping of points on a constructed plane to other points on the plane the trajectories of the system intersect at a regular period. That is at each time $t_0 + kT, (k \in Z)$, the function

$$\mathbf{x}_a(k+1) = \mathbf{P}[\mathbf{x}_a(k)] \tag{19}$$

defines a Poincare map. An equilibrium of this map represents either a fixed point of the original system or a limit cycle:

$$\mathbf{x}_a*(k+1) = \mathbf{P}[\mathbf{x}_a*(k)] \tag{20}$$

Around this discrete-time fixed point, a linear system can be constructed:

$$[\mathbf{x}_a(k+1) - \mathbf{x}*] = \left.\frac{\partial \mathbf{P}(\mathbf{x})}{\partial \mathbf{x}}\right|_{\mathbf{x}*} [\mathbf{x}_a(k) - \mathbf{x}*] , \tag{21}$$

Which can be represented in a standard systems theory form as

$$\mathbf{x}(k+1) = \mathbf{F}\mathbf{x}(k), \tag{22}$$

where $\mathbf{x}(k) = \mathbf{x}_a(k) - \mathbf{x}^*$ for simplicity. The matrix $\mathbf{F}$ is a discrete-time system matrix, and for a steady flight it is unchanging in time. Had there been control variations during this study, a model with a control input matrix could be developed. This augmented model would allow for feedback controller design. Also, it could indicate controllability of the system so that impossible maneuvers could be avoided.

The eigenvalues and eigenvectors of **F** indicate the behavior of the dynamic modes of the system. Stability requires that all these eigenvalues have complex modulus less than 1. Eigenvalues on the real axis indicate non-oscillating modes, while complex-conjugate pair eigenvalues represent oscillating modes. The eigenvectors corresponding to these eigenvalues indicate the amplitude and phase relationships between the variables when the system is exhibiting behavior in one of these modes.

8. Results

The MATLAB simulation having sufficiently matched the test data, the linearized Poincare map can be calculated. For the four state variables, ignoring x and z since they have no effect on the system's dynamics, it gives eigenvectors in column vectors:

$$\mathbf{V} = \begin{bmatrix} 0.362\mathrm{e}^{-0.640i} & 0.362\mathrm{e}^{0.640i} & -0.931 & 0.475 \\ 0.221\mathrm{e}^{2.312i} & 0.221\mathrm{e}^{-2.312i} & 0.350 & 0.866 \\ 0.752 & 0.752 & 0.0378 & -0.146 \\ 0.504\mathrm{e}^{-1.626i} & 0.504\mathrm{e}^{1.626i} & -0.0924 & 0.0628 \end{bmatrix} \tag{21}$$

The associated eigenvalues are (Figure 4.12a):

$$\lambda_1 = 0.853\mathrm{e}^{1.701i}, \lambda_2 = 0.853\mathrm{e}^{-1.701i}, \lambda_3 = 0.175,\ \lambda_4 = 0.0765. \tag{22}$$

The two real eigenvalues and their eigenvectors represent non-oscillating decaying modes. Motions in each of these modes decay quite quickly. The slower of the two, λ_3=0.175, decays to less than a fifth of its amplitude during each flapping cycle. Thus any initial conditions with a deviation strongly in the [-0.931, 0.350, 0.0378, -0.0924]^T

direction are likely not to disrupt the vehicle much. This indicates that the vehicle quickly achieves its cruising speed when disrupted. This is possibly caused by the drag on the vehicle being more important than momentum; the large wetted surface area has a large effect on the vehicle's relatively small mass.

The other real eigenvalue $\lambda_4 = 0.0765$, which decay about twice as quickly as λ_3, also have a strong effect on the velocity of the vehicle. The only main difference is that the velocities are in phase. Thus, in this case, if the vehicle were disturbed by an increased forward and downward velocity, the velocity disturbance would decay monotonically. If however, the vehicle were disturbed in forward and upward velocity, the decay would not be quite as fast. A smaller difference is that λ_4's mode has a noticable disturbance in pitch rate. The asymmetry between these modes may be due to the asymmetry in the vehicle's geometry.

The complex conjugate pair of eigenvalues is more interesting. This one describes the characteristic rocking motion of the blimp during all of the tests. Its value, $\lambda = -0.110 \mp 0.846i$, indicates a slowly decaying vibration of 1.72 rad/sec (or 0.275 *Hz*). The excitation is strongest in the pitch rate and pitch directions: $\boldsymbol{v} = \left[0.362e^{-0.640i}, 0.221e^{2.312i}, 0.752, 0.504e^{-1.626i}\right]^T$. But there is significant oscillation in the velocity as well; also, the oscillations in *U* and *W* are nearly completely out of phase with each other (2.951 radians). The damping ratio of this mode is 0.0933.

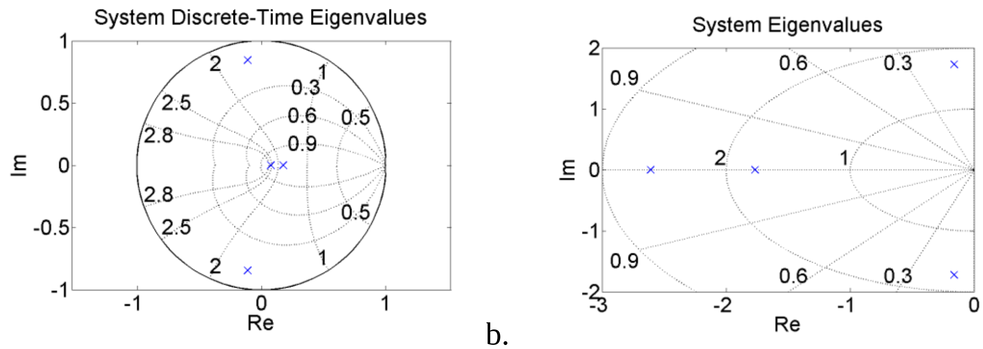

a. b.

Figure 4.12 - Eigenvalues a. plotted in the *z*-plane, b. transformed to the *s*-plane.

When transformed to continuous-time dynamics the eigenvalues all reside on the left-half plane (Figure 4.12b). The oscillatory mode seems to resemble a phugoid-like mode in that it primarily appears in the pitch and velocity, and it is so lightly damped. The system thus resembles an airplane with no short period mode. There are, however, nonlinear vibrations caused by the wing flapping motion. These vibrations at the flapping frequency are not considered under Floquet analysis since they are the baseline motion and not perturbations.

9. Conclusion

The ornithoptic blimp flew well within the test facility and allowed collection of flapping-wing data. This capability is added to that for stationary wing flapping devices mounted to load cells. Those devices can be used in a wind tunnel or in quiescent air, but they do not allow the coupling between aerodynamics and vehicle dynamics that is so interesting here. Heavier-than-air ornithopters also could be used for aerodynamics and flight dynamics analysis, but their higher speed makes data collection more difficult at resolutions where aerodynamic effects can be observed. With the blimp, it was possible to evaluate flight performance at time and size scales within the grasp of available sensors. It was shown that quasi-steady aerodynamic analysis can be applied to flapping-wing vehicles, accurately capturing dynamic modal effects of forward flight. Flight dynamics with disturbed initial conditions could be simulated without much difficulty. The Floquet analysis confirmed that the nonlinear dynamical system behaved like a perturbed linear system when the disturbance was not too large. Also, this validated the methods of limit cycle analysis to real engineered systems and bodes well toward their future application to other periodic flight dynamic systems such as helicopters and heavier-than-air ornithopters. This may also have application to windmills (both conventional and with flapping wings) and to vibrating power harvesting structures. The ornithoptic blimp is a vehicle designed as a test platform for ornithopter flight dynamics. It is also a buoyant vehicle capable of carrying a payload such as a camera or microphone. This design may be improved for higher payload by reducing the weight of some of the components (especially the electronics). This payload capacity, combined with the blimp's low power consumption when loitering, allows for several applications, including long-time surveillance, event observation, or for hobbyists. Further improvements to the design will increase its flight time endurance and its maneuverability.

REFERENCES

[1] Moon, F. C. *The Machines of Leonardo Da Vinci and Franz Reuleaux*, Springer, Dordrecht, The Netherlands, 2007, 255-262.

[2] Ellington, C. P. The Aerodynamics of Hovering Insect Flight. I. The Quasi-Steady Analysis. *Phil. Trans. R. Soc. Lond. B.*, 1984, **305**, 1-15.

[3] Dickinson, M. H., Lehmann, F. O., and Sane, S. P. Wing Rotation and the Aerodynamic Basis of Insect Flight. *Science*, 1999, **284**(5422), 1954-1960.

[4] Wang, Z. J. Dissecting Insect Flight. *Annual Review of Fluid Mechanics*, 2005, **37**, 183-210.

[5] Wang, Z. J. **Dragonfly Flight.** *Physics Today*, 2008, October, 74-75.

[6] Theodorsen, T. General Theory of Aerodynamic Instability and the Mechanism of Flutter. *NACA Technical Report*, 1935, No. 496.

[7] Jones, R. T. The Unsteady Lift of a Wing of Finite Aspect Ratio. *NACA Technical Report*, 1940, No. 681.

[8] DeLaurier, J. D. An Aerodynamic Model for Flapping-Wing Flight. *Aeronautical Journal*, 1993, April, 125-130.

[9] Dietl, J. M., and Garcia, E. Stability in Ornithopter Longitudinal Flight Dynamics. *Journal of Guidance, Control, and Dynamics*, 2008, **31**(4), 1157-1162.

[10] Berman, G. and Wang, Z. J. Energy-minimizing kinematics in hovering insect flight. *J. Fluid Mech.*, 2007, **582**, 153-168.

[11] Bar-Shalom, Y., Li, X. R., and Kirubarajan, T. *Estimation with Applications to Tracking and Navigation*, John Wiley and Sons Inc., New York, 2001, 138-140.

CHAPTER 5

BEAM SHAPE OPTIMIZATION FOR POWER HARVESTING[1]

1. Abstract

A problem in piezoelectric bimorph energy harvesting is to generate the most power with limits in system mass. The authors propose a new approach: to change the shape of the beam to concentrate the strain in sections of the beam where it can contribute the most to transduction. A vibration model of beams with non-uniform width is developed and validated with shaker table tests. Three beams with different shapes are tested over a wide band, encompassing the lowest two modes of vibration. An optimal beam shape is calculated using a heuristic optimization code and the attributes of this optimal beam are discussed. Then, beam shapes are optimized to allow for increased base excitation and constrained by maximum root strain. Finally, the tip mass-to-beam mass ratio is studied parametrically, correlating increased transduction with increased beam mass.

2. Introduction

There are classes of problems where miniaturization and mass reduction are critical. One such application is the development of functional electronics to be carried by

---

[1] From Dietl, J. M., and Garcia, E., "Beam Shape Optimization for Power Harvesting," *Journal of Intelligent Material Systems and Structures*, Vol. 21, April 2010, pp. 633-646; Reprinted with permission of Sage Publications.

animals. A project is currently under way to implant cybernetics in insects [1]. These electronic implants contain sensors for collecting data and navigation, communications devices for data transfer and for delivering instructions, and actuators (mainly sonic pulses) to control the insect's flight [2]. Minimizing power supply weight is mandatory for the insect to fly unencumbered. Thus power harvesting may have a new application in the development of active tagging for animal tracking.

Piezoelectric actuators and sensors have long been the subject of experimental and analytical study, for actuation, actuator dimension optimization, actuator placement optimization, and sensor placement. During the last decade, a growing segment of researchers has focused on power harvesting, employing experimental and analytical methods.

Among earlier experimental studies was [3] which modeled and tested a piezoelectric stack actuator, concluding: the stack's efficiency peaked at a frequency much lower than the stack's structural resonance, and that due to nonlinearities the system's energy transfer frequency was dependent on amplitude of force input. Due to vibration energy being generally lower in the frequency spectrum, most studies of piezoelectric energy harvesters have focused on cantilevered beams with transverse vibration. Roundy and Wright [4] provided a model and experiment for a piezoelectric bimorph.

There are many papers on piezoelectric bimorph and unimorph modeling, including Roundy and Wright [4], whose model relied on adapting piezoelectric constitutive laws and Euler-Bernoulli strain-bending assumptions to an electronic-analog set of equations. This model was utilized to provide an adequate input to a set of candidate power harvesting circuits. Other single degree of freedom models have been published

[5], but they are not intended to capture a system's response to vibration and electronic coupling over a wider bandwidth. Without this bandwidth both the higher modes of vibration inherent to wide-band excitation and nonlinear forcing from coupling circuitry are ignored.

The Rayleigh-Ritz approach to modeling transverse vibrations is a popular alternative. Hagood and von Flotow [6] derived the basic framework for modeling a general piezoelectric actuator/sensor through discrete modes of electromechanical excitation. As applied in [7] and [8], a generalized Hamiltonian of the coupled electromechanical system is constructed in terms of a finite selection of applicable basis functions. From this, a set of coupled differential equations describing the system, including an arbitrary number of shape functions, can be generated. A second approach eschews the Hamiltonian energy formulations and directly applies the piezoelectric constitutive laws to the Euler-Bernoulli beam deformation equation on both unimorph [9] and bimorph [10] configurations. These have been verified as accurate over varying electrical loads and with varying tip mass.

Researchers have studied alternative beam configurations as well. Erturk et al. [11] studied an L-shaped beam-mass structure with constant cross section.

This paper presents a study of beams with varying cross-sectional area. The motivation is that the strain is not constant along the length of a piezoelectric bimorph. However, the electric field across the piezoelectric layers is proportional to axial strain. By arranging the beam so that there is more piezoelectric material where there is more strain, and removing material from where there is less strain, the overall coupling of the beam can be increased.

This has been previously studied by Goldschmidtboeing and Woias [12] and by Paquin and St-Amant [13]. Those studies looked at rectangular and triangular beams, concluding that there was little improvement in efficiency in triangular beams, but the beams did permit greater excitation amplitude. Our motivation is to optimize over a larger range of shapes and tip masses to further exhaust the possibilities for beam shape to effect greater power output.

These beams are designed as cantilevered bimorph transverse vibrators with tip mass, with a constant layer thickness—the beam's total thickness does not vary. Instead, the beam width is adjusted to affect the strain distribution throughout the length of the beam, to provide increased transduction efficiency at resonance.

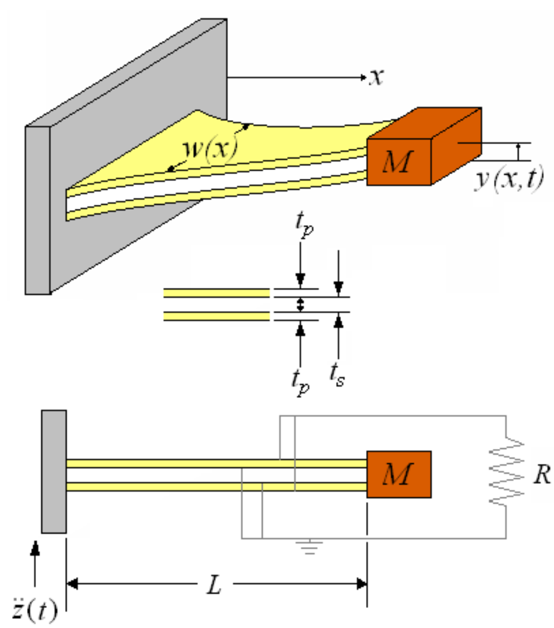

Figure 5.1 - A piezoelectric bimorph schematic.

3. Piezoelectric Cantilever Modeling

The piezoelectric bimorph is modeled as a coupled electromechanical system (Figure 5.1). The beam is composed of a brass substrate (thickness t_s) sandwiched between two layers of piezoelectric ceramic (thickness t_p), polarized in the same direction so that they can be operated in parallel. When a voltage is applied across the beams toward the brass substrate, one layer expands as the other contracts. The alternative configuration, where the beams are polarized for series operation, is not discussed. The width of the beam is allowed to vary along its length, but the piezoelectric and substrate widths are identical.

Each piezoelectric ceramic layer is sandwiched between two electrode surfaces. These provide a uniform voltage along each surface of the ceramic, akin to a parallel plate capacitor. The ceramic layers' electric fields are uniform due to the assumptions that the electrodes are perfect conductors (and thus the voltage at all points along the electrode is the same) and the ceramic has a uniform dielectric constant. Although the strain and electric displacement are functions of the electric field, they adjust themselves according to the material's constitutive laws. The electrodes assumed to be thin enough to have no effect on the mechanical properties of the beam, but only to facilitate electromechanical coupling in the piezoceramic layers.

The two ceramics are wired in parallel with each other and with a load resistor *R*. This resistor provides an electric load, and prevents the high-impedance measuring devices (oscilloscope and dynamic signal analyzer) from affecting the system performance. This simple circuit does not approximate any practical energy harvesting circuitry, but it helps to characterize the electromechanical parts of the complete device. Thus, the model of the mechanical and electrical behavior of the piezoelectric will permit development of the power circuitry, which could be easily coupled to the beam model.

The Euler-Bernoulli model is appropriate for handling transverse vibrations of composite beams that are sufficiently long and slender. Its main assumptions that distinguish it from more sophisticated modeling techniques are that all motions occur in plane (i.e. that mass elements inside the beam are constrained to one dimension), and that shear strain and rotational inertia are neglected.

3.1. Mathematical Model

Hagood et al. [6] provides a good starting point to model piezoelectric cantilevers using Hamilton's principle. This approach is later followed by Sodano et al. [7], but since it assumes a constant beam width *w*, the system matrices must be re-derived for this system. In this Hamiltonian system, the dynamics can be constructed from the integral of action given here:

$$\int_{t_1}^{t_2} \left[\delta \left(T - U + W_e \right) + \delta W + \delta D \right] dt = 0 \quad (1)$$

The terms in the equation are the kinetic energy T and potential energy U of the vibrating beam, the stored energy W_e in the electric field of the piezoelectric device, and the applied work W. The sum: $T - U + W_e$ is called the Lagrangian L_a. There is also a dissipation function D that will account for the energy lost in the resistor. In an elastic body, we must account for the energies at all points within the structure; hence they will take the form of volume integrals.

To apply this to a bimorph piezoelectric bender, we assume that the motion of the beam is constrained to the transverse direction, that only one component of $\mathbf{u}$, $y(x,t)$, is nonzero. Furthermore, strain in the beam can be expressed as a function of the displacement $y(x,t)$ and its spatial partial derivatives. We also assume that the electric field in each piezoceramic layer is equal (but opposite sign due to symmetry) and has a scalar value E. Also, the electric field inside the (conducting) substrate is 0.

3.2. Kinetic Energy

The first integral is the kinetic energy:

$$T = \int_V \frac{1}{2} \rho \dot{\mathbf{u}}^T \dot{\mathbf{u}} dV \tag{2}$$

The equation considers the motions of infinitesimal elements of the elastic structure; each element has density ρ and velocity vector $\dot{\mathbf{u}}$. Applying the assumption of planar motion, there is only one nonzero component of the velocity field, $\frac{\partial y(x,t)}{\partial t}$.

Since, the velocity is applied in this single direction, the y-z sections can be considered as solid elements vibrating uniformly with a single mass and displacement. The mass of an infinitesimal slice of the beam is: $m = w(x)(\rho_s t_s + 2\rho_p t_p)dx$, where ρ_s and ρ_p are the densities of the substrate and piezoelectric layers respectively. The term:

$$\rho_l = (\rho_s t_s + 2\rho_p t_p) \tag{3}$$

will be used as shorthand throughout this exposition.

The tip mass's energy is also considered here. It is a rigid block of mass M_0, and it is constrained to move in one direction. After integrating in the *y* and *z* directions, the kinetic energy of the beam-mass structure simplifies to:

$$T = \frac{1}{2}\int_0^L \rho_l w(x)\left(\frac{\partial y(x,t)}{\partial t}\right)^2 dx + \frac{1}{2}M_0\left(\frac{\partial y(L,t)}{\partial t}\right)^2 . \tag{4}$$

If the tip mass is allowed to rotate however, the kinetic energy term expands to include the additional translational and rotational kinetic energies:

$$T = \frac{1}{2}\int_0^L \rho_l w(x)\left(\frac{\partial y(x,t)}{\partial t}\right)^2 dx + \frac{1}{2}M_0\left[\left(\frac{\partial y(L,t)}{\partial t}\right)^2 + l_m \frac{\partial y(L,t)}{\partial t}\frac{\partial^2 y(L,t)}{\partial t \partial x} + \left(\frac{l_m^{\ 2}}{3} + \frac{h_m^{\ 2}}{12}\right)\left(\frac{\partial^2 y(L,t)}{\partial t \partial x}\right)^2\right] \tag{5}$$

which has an effect on the calculated dynamics when the tip mass to beam mass ratio α is high.

3.3. Potential Energy

Mechanical potential energy *U* is the energy stored in the elastic elements due to deformation. It is the integral of the dot product of the strain vector **S** and the stress vector **T**:

$$U = \int_V \frac{1}{2}\mathbf{S}^T\mathbf{T}dV . \tag{6}$$

Due to the assumption that there is strain in the axial direction (the *x* direction), we represent the strain with the scalar *S*. The axial strain in a beam undergoing bending is proportional to the curvature of the beam, as expressed by the displacement's second spatial derivative. The strain is also a function of position within the material; it is proportional to the distance $\hat{y}$ from the neutral axis:

$$S = -\hat{y}\frac{\partial^2 y(x,t)}{\partial x^2} \quad . \tag{7}$$

This is derived from the Euler-Bernoulli beam model (for instance, see [14]).

To calculate the stress in the beam, we use the material constitutive equations in one dimension. Here is the constitutive law for the center shim:

$$T_s = \frac{1}{s_s} S_s \quad . \tag{8}$$

The stress T_s is equal to the strain divided by the compliance s_s. The piezoceramic's relationships are more complicated, in that the electric field also adds to the material's stress:

$$T_p = \frac{1}{s^E{}_p} S_p - \frac{d}{s^E{}_p} E \quad . \tag{9}$$

Thus, the stress in the piezoelectric element is equal to the sum of the mechanical stress and the stress due to piezoelectric effect. The mechanical stress is identical to that of the non-piezoelectric shim (strain divided by compliance), except for a different compliance coefficient $s^E{}_p$. Here the superscript denotes the value of the compliance measured at a constant electric field. The electrically induced stress is proportional to the electric field with a coefficient of the piezoelectric coupling coefficient d divided by the compliance.

To evaluate the potential energy, it is necessary to subdivide the volume of the beam into the substrate and piezoelectric parts. Fortunately, the additive nature of integration encourages this. Thus the stress at a point in the substrate is (using Equations (7) and (8)):

$$T_s = \frac{1}{s_s} S(x,t,\hat{y}) = -\frac{1}{s_s} \hat{y} \frac{\partial^2 y(x,t)}{\partial x^2} \quad . \tag{10}$$

The stress in the piezoelectric is (using Equations (7) and (9)):

$$T_p = \frac{1}{s^E{}_p} S(x,t,\hat{y}) - \frac{d}{s^E{}_p} E = -\frac{1}{s^E{}_p} \hat{y} \frac{\partial^2 y(x,t)}{\partial x^2} - \frac{d}{s^E{}_p} E \quad . \tag{11}$$

The piezoelectric stress has two terms, one proportional to strain, and one proportional to electric field. These terms will also be separated into manageable integrals.

The potential energy term integrates strain times the stress within the volume of the material:

$$U = U_s + U_{p_S} + U_{p_E} \quad . \tag{12}$$

where we recombine the piezoelectric and shim terms that do not depend on electric field. The resulting integrals can be evaluated over width (*z* direction):

$$\begin{aligned} U_s + U_{p_S} = & \frac{1}{2}\int_0^L \int_{-t_s/2}^{t_s/2} w(x) \frac{\hat{y}^2}{s_s} \left(\frac{\partial^2 y(x,t)}{\partial x^2} \right)^2 d\hat{y}dx + \frac{1}{2}\int_0^L \int_{t_s/2}^{t_p+t_s/2} w(x) \frac{\hat{y}^2}{s^E{}_p} \left(\frac{\partial^2 y(x,t)}{\partial x^2} \right)^2 d\hat{y}dx \ldots \\ & + \frac{1}{2}\int_0^L \int_{-t_s/2-t_p}^{-t_s/2} w(x) \frac{\hat{y}^2}{s^E{}_p} \left(\frac{\partial^2 y(x,t)}{\partial x^2} \right)^2 d\hat{y}dx \end{aligned} \quad . \tag{13}$$

The terms dependant on $\hat{y}$ can be separated:

$$U_s + U_{p_S} = \frac{1}{2}\frac{1}{s^E{}_p}\left[\eta_s \int_{-t_s/2}^{t_s/2} \hat{y}^2 d\hat{y} + \int_{t_s/2}^{t_s/2+t_p} \hat{y}^2 d\hat{y} + \int_{-t_s/2-t_p}^{-t_s/2} \hat{y}^2 d\hat{y}\right]\int_0^L w(x)\left(\frac{\partial^2 y(x,t)}{\partial x^2}\right)^2 dx\,. \qquad (14)$$

The constant η_S equals the shim compliance divided by the piezoelectric compliance. Then the $\hat{y}$ integral can be evaluated, leaving an integral in x multiplied by a group of coefficients independent of the beam shape and motion:

$$U_s + U_{p_S} = \frac{1}{2}\frac{I_{0w}}{s^E{}_p}\int_0^L w(x)\left(\frac{\partial^2 y(x,t)}{\partial x^2}\right)^2 dx\,. \qquad (15)$$

I_{0w}, the term in the square brackets in Equation (14), is a coefficient derived from the composite nature of the beam, equal to the moment of inertia of the beam's cross section divided by the cross section's width:

$$I_{0w} = \eta_s \int_{-t_s/2}^{t_s/2} \hat{y}^2 d\hat{y} + \int_{t_s/2}^{t_s/2+t_p} \hat{y}^2 d\hat{y} + \int_{-t_s/2-t_p}^{-t_s/2} \hat{y}^2 d\hat{y} = \frac{I_{zz}(x)}{w(x)} \qquad (16)$$

This is a constant, dependent only on the layer's thicknesses and compliance.

The potential energy term dependent on the electric field is an integral over the volume, first evaluated in the z direction:

$$U_{p_E} = \frac{1}{2}\int_0^L \frac{\partial^2 y(x,t)}{\partial x^2}\left(\frac{-d}{s^E{}_p}\right)E(t)w(x)\left[\int_{t_s/2}^{t_s/2+t_p} \hat{y}d\hat{y} + \int_{-t_s/2-t_p}^{-t_s/2} -\hat{y}d\hat{y}\right]dx\,. \qquad (17)$$

Again, the terms dependent on $\hat{y}$ can be separated out and integrated independently of the integral in x. This leaves:

$$U_{p_E} = -\frac{1}{2}\left(t_s t_p + t_p{}^2\right)\frac{d}{s^E{}_p}E(t)\int_0^L w(x)\frac{\partial^2 y(x,t)}{\partial x^2}dx\,. \qquad (18)$$

3.4 Electric Potential Energy

The electrical potential energy is the integral of the electric field **E** times the electric displacement **D**:

$$W_e = \int_V \frac{1}{2} \mathbf{E}^T \mathbf{D}\, dV \quad . \tag{19}$$

When an electric field is applied to a dielectric material, the poled molecules in the material deform in response. This electrical deformation is called the electric displacement.

Once again, it is necessary to consider the constitutive equations of the piezoelectric:

$$D_p = \frac{d}{s^E{}_p} S_p + \varepsilon^S E \quad . \tag{20}$$

The equation for electric displacement is similar to that for stress (Equation (9)); all the terms are familiar save for ε^S, the dielectric constant evaluated at constant strain. Also, it is noted that the electric field in the substrate is identically zero, so that there is no electric potential energy to be evaluated there. The expression $\mathbf{E}^{\mathrm{T}}\mathbf{D}$ becomes a scalar and dependent only on $y(x, t)$ and E (Equations (20) and (7)):

$$ED_p = -\hat{y} \frac{\partial^2 y(x,t)}{\partial x^2} \frac{d}{s^E{}_p} E + \varepsilon^S E^2 \tag{21}$$

We can now evaluate Equation (19), but first it is easier to separate the equation into two integrals: one for terms solely dependent on the electrical characteristics, and one with both electrical and mechanical components. Thus:

$$W_e = W_{e_S} + W_{e_E} \quad (22)$$

First, the mechanically dependent integral is identical to Equation (17), with opposite sign:

$$W_{e_S} = \frac{1}{2}\int_0^L \frac{\partial^2 y(x,t)}{\partial x^2}\left(\frac{d}{s^E{}_p}\right)E(t)w(x)\left[\int_{t_s/2}^{t_s/2+t_p} \hat{y}d\hat{y} + \int_{-t_s/2-t_p}^{-t_s/2} -\hat{y}d\hat{y}\right]dx \quad (23)$$

It is simplified as before:

$$W_{e_S} = \frac{1}{2}\left(t_s t_p + t_p{}^2\right)\frac{d}{s^E{}_p}E(t)\int_0^L w(x)\frac{\partial^2 y(x,t)}{\partial x^2}dx \quad (24)$$

The other integral is pure energy storage in an electric field. It resembles the energy stored in a parallel plate capacitor:

$$W_{e_E} = \frac{1}{2}\int_0^L \int_{t_s/2}^{t_s/2+t_p} E(t)^2 w(x)\varepsilon^S d\hat{y} + \int_{-t_s/2-t_p}^{-t_s/2} E(t)^2 w(x)\varepsilon^S d\hat{y}dx \quad (25)$$

By separating out the $\hat{y}$ integral, we arrive at a simpler expression for the energy in the electric field:

$$W_{e_E} = \varepsilon^S t_p E(t)^2 \int_0^L w(x)dx \quad (26)$$

In fact, if we were to measure the capacitance of the beam it would equal to this:

$$C_b = 2\frac{\varepsilon^S}{t_p}\int_0^L w(x)dx \quad (27)$$

3.5 Applied Forces and Charges

Finally, we allow for external forces and charges to be applied to the structure. These are accounted for in this applied work integral:

$$\partial W = \int_V \mathbf{u} \cdot \mathbf{f} dV - \partial I(t) \delta\lambda \quad . \tag{28}$$

There are two terms. The first is the applied mechanical work to the structure, the integral of the displacement field (of the infinitesimal mass elements of the structure) **u** dotted with the force distribution **f**. The second term is the applied electrical work, the current into the capacitor (rate of charge accumulation) times the flux linkage λ on the electrodes.

For this analysis, the applied force on the beam is a base excitation, and the applied charges are the coupling of the piezoelectric electrodes to an RC circuit. The base excitation is given by an applied acceleration $a(t)$ to the mass of the beam:

$$\partial W_f = \int_0^L f(x,t)dx = \left[\int_0^L \rho_l w(x) \partial y(x,t) dx + M_0 \partial y(L,t) \right] a(t) . \tag{29}$$

The base excitation is an acceleration of the root of the beam, constrained to the transverse direction. This manifests itself in the beam equations as a distributed force. If the tip mass is allowed to rotate, then there is a grander expression for the mechanical work input:

$$W_f = \left[\int_0^L \rho_l w(x) \partial y(x,t) dx + M_0 \left\{ \partial y(L,t) + \frac{L_m}{2} \partial \left. \frac{\partial y(x,t)}{\partial x} \right|_{x=L} \right\} \right] a(t) . \tag{30}$$

The extra term accounts for the center of mass of the tip mass being offset from the end of the beam by a distance of ½ L_m.

The electrical work on the beam is:

$$\partial W_Q = -2I(t)\partial\lambda \quad (31)$$

The current, $I(t)$, is determined by the external circuit elements connected to the beam. A dissipation function D is the simplest way to account for the resistor's effect on the system. In this case, the function is:

$$D = \frac{1}{2}\frac{\dot{\lambda}^2}{R} \quad (32)$$

3.6. Rayleigh-Ritz

It is necessary to put the terms of the Hamiltonian into an accessible form. Since the coordinate $y(x, t)$, a function of two independent variables, is unwieldy, the principle of separation of variables used. We set $y(x, t)$ equal to the product of two vector variables, one dependent on space and the other on time. Thus:

$$y(x,t) = \boldsymbol{\varphi}(x)^T \mathbf{q}(t) \quad (33)$$

The space-dependent variable $\boldsymbol{\varphi}(x)$ is a vector of assumed mode shapes. Analytical formulas for the mode shapes of an arbitrary beam are unknown, but the mode shapes for a slender prismatic beam with a tip mass is known (see, for instance, [14]). They are selected to be admissible solutions to the Euler-Bernoulli beam equation for a prismatic beam with the same boundary conditions as our composite beam. The general form for the mode shape of the k^{th} mode is:

$$\phi_k(x) = C_1\left(\sin\beta_k x - \sinh\beta_k x - \frac{\sin\beta_k + \sinh\beta_k}{\cos\beta_k + \cosh\beta_k}(\cos\beta_k x - \cosh\beta_k x)\right) \tag{34}$$

where β_k is a natural frequency of vibration determined from the characteristic equation:

$$\frac{1}{\alpha}(\cos\beta\cosh\beta + 1) + \beta(\cos\beta\sinh\beta - \sin\beta\cosh\beta) = 0 \tag{35}$$

and α is the ratio of the tip mass to the mass of the rest of the beam:

$$\alpha = \frac{M_0}{m_{beam}}. \tag{36}$$

For shorthand, we use the dot symbol ($\dot{}$) for time derivatives, and the prime ($'$) symbol for x derivatives.

We want to use the electric field to compute the voltage V across the piezoelectric beams, so we use the linear assumption:

$$E = \frac{V}{t_p}. \tag{37}$$

Finally, we introduce the flux linkage λ, whose derivative is equal to the voltage:

$$\dot{\lambda} = V. \tag{38}$$

This aids in the resolution of the Hamiltonian into ordinary differential equations for the behavior of the whole electromechanical system [15].

After replacing substituting for $y(x,t)$ and E in Equations (4), (15), (18), (24), (26), (30), (31), and (32) we can assemble the integral of action (for the non-rotating tip mass case):

$$\int_{t_1}^{t_2} \partial\left[T-\left(U_s+U_{pS}\right)-U_{pE}+W_{eS}+W_{eE}\right]+\partial\left(W_f+W_Q\right)+\partial D dt=0 \tag{39}$$

$$\begin{aligned}&\int_{t_1}^{t_2} \partial\left\{\frac{1}{2}\int_0^L \rho_l w(x)\left(\boldsymbol{\varphi}(x)^T\dot{\mathbf{q}}(t)\right)^2 dx+\frac{1}{2}M_0\left(\boldsymbol{\varphi}(L)^T\dot{\mathbf{q}}(t)\right)^2+\frac{\varepsilon^S}{t_p}\dot{\lambda}^2\int_0^L w(x)dx\right.\\&\left.+\frac{1}{2}\frac{I_{0w}}{s^E{}_p}\int_0^L w(x)\left(\boldsymbol{\varphi}''(x)^T\mathbf{q}(t)\right)^2 dx-\left(t_st_p+t_p{}^2\right)\frac{d}{t_ps^E{}_p}\dot{\lambda}\int_0^L w(x)\boldsymbol{\varphi}''(x)^T\mathbf{q}(t)dx\right\}\\&+\partial\left\{\left[\int_0^L \rho_l w(x)\boldsymbol{\varphi}(x)^T\mathbf{q}(t)dx+M_0\boldsymbol{\varphi}(x)^T\mathbf{q}(t)\right]a(t)-2I(t)\partial\dot{\lambda}+\partial\frac{\dot{\lambda}^2}{2R}\right\}dt=0\end{aligned} \tag{40}$$

Lagrange’s equation for the system is:

$$\frac{d}{dt}\frac{\partial L_a}{\partial\dot{\mathbf{q}}}-\frac{\partial L_a}{\partial\mathbf{q}}+\frac{\partial D}{\partial\dot{\mathbf{q}}}=F\,, \tag{41}$$

$$\frac{d}{dt}\frac{\partial L_a}{\partial\dot{\lambda}}-\frac{\partial L_a}{\partial\lambda}+\frac{\partial D}{\partial\dot{\lambda}}=I(t)\,. \tag{42}$$

These are Lagrange’s equations, generalized for an electromechanical system (see, for instance, [16]). After evaluating the derivatives, we are left with two sets of ordinary differential equations that describe the motion of the beam:

$$\mathbf{M}\ddot{\mathbf{q}}(t)+\mathbf{K}\mathbf{q}(t)-\boldsymbol{\Theta}V(t)=\mathbf{u}a(t)\,, \tag{43}$$

and the electronics:

$$C_b \dot{V}(t) + \frac{1}{R} V(t) = \mathbf{\Theta}^T \dot{\mathbf{q}}(t). \tag{44}$$

These are linear, coupled, time-invariant, ordinary differential equations. The coefficient matrices are dependent on the width $w(x)$ and the assumed mode shapes. First, the mass matrix **M**:

$$\begin{aligned}\mathbf{M} = \int_0^L \rho_l w(x) \boldsymbol{\varphi}(x) \boldsymbol{\varphi}(x)^T dx \; + M_0 \Bigg\{ &\boldsymbol{\varphi}(L) \boldsymbol{\varphi}^T(L) + \frac{l_m}{2} \boldsymbol{\varphi}'(L) \boldsymbol{\varphi}^T(L) \cdots \\ &\cdots + \frac{l_m}{2} \boldsymbol{\varphi}(L) \boldsymbol{\varphi}'^T(L) + \left(\frac{l_m^{\,2}}{3} + \frac{h_m^{\,2}}{12} \right) \boldsymbol{\varphi}'(L) \boldsymbol{\varphi}'^T(L) \Bigg\}\end{aligned}. \tag{45}$$

It is equivalent to the mass matrix in a standard (non-electromechanical) beam vibration problem. It has two terms: the first dependent on the beam density and geometry, and the second is dependent on the tip mass. It is a square, symmetric, positive definite matrix with size equal to the number of mode shapes.

Next, the stiffness matrix **K**:

$$\mathbf{K} = \frac{I_{0w}}{s^E{}_p} \left[\int_0^L w(x) \boldsymbol{\varphi}''(x) \boldsymbol{\varphi}''^T(x) dx \right]. \tag{46}$$

This matrix is exactly the same as the equivalent stiffness matrix in an Euler-Bernoulli beam. It is also square, symmetric, and positive definite.

The coupling matrix $\mathbf{\Theta}$ is used in both the electrical and mechanical equations:

$$\mathbf{\Theta} = \left(t_s t_p + t_p^{\,2} \right) \frac{d}{s^E{}_p t_p} \left[\int_0^L w(x) \boldsymbol{\varphi}''(x) dx \right]. \tag{47}$$

It depends on mechanical (s^E_p, $\boldsymbol{\varphi}$), electrical (d), and geometric (w, t_s, t_p) properties of the system.

Finally, the input matrix **u** couples the base excitation to the beam motion:

$$\mathbf{u} = \int_0^L \rho_l w(x) \boldsymbol{\varphi}(x)^T dx + M_0 \left(\boldsymbol{\varphi}(L) + \frac{l_m}{2} \boldsymbol{\varphi}'(L) \right). \tag{48}$$

This matrix is in units of mass to multiply with acceleration and simulate a force on the beam structure.

The beam model developed here is derived from the fundamental properties of piezoelectric and non-piezoelectric materials, and from the standard assumptions of linear mechanics of bending structures. When the constraint that each beam has a constant cross section is applied, the model collapses to that in [7] and [8].

4. Model Verification

To validate the variable-width Euler-Bernoulli model, and to verify the piezoelectric material properties, a series of tests were conducted. Each beam was designed to resonate at 28 *Hz*. These tests are especially needed to determine the model's verisimilitude for non-rectangular beams. The beams were cut from a sheet of piezoelectric bending sensor stock, Piezo Systems, Inc.'s T220-A4-503 (Y) bending sensor.

a. b.

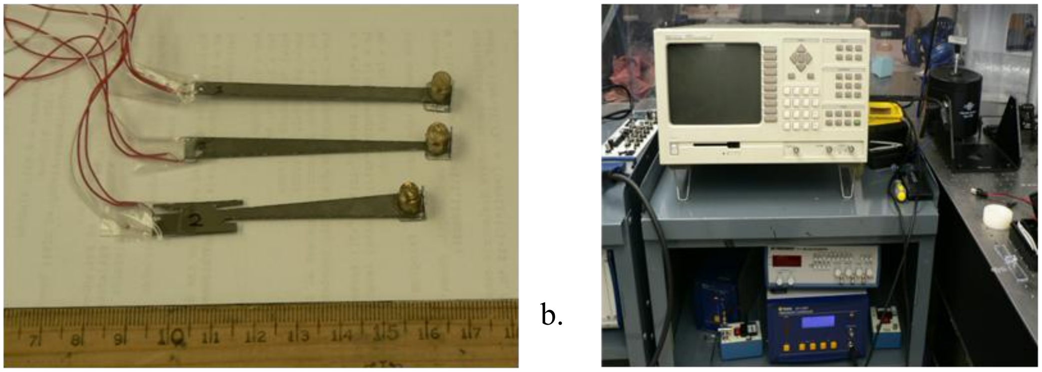

Figure 5.2 - a. Three beams designed and tested. b. The testing rig complete with signal analyzer, shaker table, and conditioning electronics.

Thus, three beam shapes are tested (Figure 5.2a): straight (rectangular), tapered (growing thinner toward the tip), and reverse tapered (growing wider toward the tip). The cantilevered sections of each beam have identical mass 0.8 *g*, and all beams have an identical tip mass of 1.2 *g*. With the basic shapes of the beams selected, each beam's length and width were adjusted so that they would have identical area while resonant (first mode) at 28 *Hz*, (hence, the different lengths of the beams).

For each beam, a parallel resistance is added. The resistance was chosen to match the capacitance of each beam at the chosen excitation frequency [17]:

$$R = \frac{1}{j\omega C}\,. \tag{49}$$

We measure the voltage across the piezoelectric using both the oscilloscope and a Hewlett-Packard 35660A Dynamic Signal Analyzer—the latter is capable of providing simultaneous wide-band excitation and measurement. Additionally, the base acceleration is measured, and thus a frequency response function from the base excitation to the voltage output of the piezoelectric can be constructed. The frequency range of the test is selected to cover the first two modes of excitation.

Each beam is excited by random base excitations by a Brüel & Kjær Type 4809 Shaker Table: the random signal was sent from the Signal Analyzer to the Brüel & Kjær Type 2718 Power Amplifier. The measured outputs are the base acceleration and the voltage output from the piezoceramic through the resistor.

Figure 5.3 shows that the mathematical model of the system is capable of capturing the effects of the beam shape variation, including the frequencies of the first 2 modes and the shape of the curves between modes.

After each beam's frequency response function was measured, the data is utilized to calculate the damping ratios of the three beams, (using a subspace method in MATLAB). This information is unmodeled prior to experiment. Also unmodeled are any torsional modes of vibration, but they appear in experimental data at a frequency between the two transverse vibration resonances. These experiments allow the authors to confidently simulate the beam response to base excitation, and to use such simulations for design and optimization.

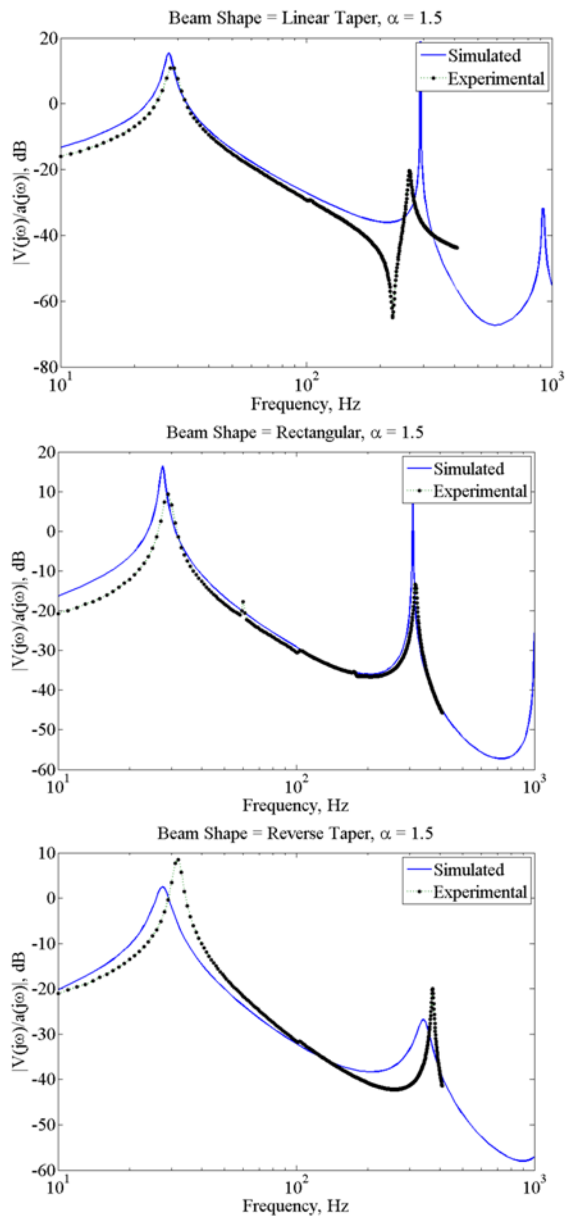

Figure 5.3 - Frequency response functions of the three beams. a. Linear Taper, b. Rectangular, c. Reverse Taper.

5. Simulation

MATLAB is used to simulate the electrical response of a system with a resistive load to a sinusoidal displacement excitation at a given frequency. The equations of motion are linear, and thus the resulting vibratory motions are easily calculable.

5.1. Nondimensionalization of Equations of Motion

For increased numerical stability and smoother optimization, the equations of motion were nondimensionalized. Using appropriate changes in variables, we can produce dimensionless equations to simplify analysis and simulation. Letting:

$$\tilde{x} = \frac{x}{L},\ \tilde{y} = \frac{y}{y_+},\ \tilde{w} = \frac{w}{w_+},\ \tilde{V} = \frac{V}{V_0},\ \tilde{t} = \frac{t}{t_0},\ \tilde{q} = \frac{q}{y_+} \tag{50}$$

where the denominators are selected to be on the order of the variables they reduce. The characteristic time t_0, is the reciprocal of the dimensionless natural frequency of the bending vibration:

$$t_0^{\ 2} = \frac{s^E{}_p L^4 \rho_l}{I_{0w}} \ . \tag{51}$$

The characteristic displacement is the length of the beam:

$$y_+ = L \ . \tag{52}$$

The characteristic voltage V_0 is such that the dimensionless electromechanical coupling matrix (57) is on the same order as the mass and stiffness matrices:

$$V_0 = \frac{\rho_l y_+ L^2 s^E{}_p t_p}{d(t_s + t_p) t_0^{\ 2}} \ . \tag{53}$$

Finally, the characteristic width w_+ is equal to the average width of the beam:

$$w_+ = \frac{1}{L}\int_0^L w(x)dx \quad (54)$$

We can define these matrices, which are normalized dimensionless analogs to the matrices defined in equations (45)-(48):

$$\begin{aligned}\tilde{\mathbf{M}} = \int_0^1 \tilde{w}(\tilde{x})\tilde{\boldsymbol{\varphi}}(\tilde{x})\tilde{\boldsymbol{\varphi}}(\tilde{x})^T d\tilde{x} + \alpha\Bigg\{&\tilde{\boldsymbol{\varphi}}(1)\tilde{\boldsymbol{\varphi}}^T(1) + \frac{l_m}{2L}\tilde{\boldsymbol{\varphi}}'(1)\tilde{\boldsymbol{\varphi}}^T(1)\cdots \\ &\cdots + \frac{l_m}{2L}\tilde{\boldsymbol{\varphi}}(1)\tilde{\boldsymbol{\varphi}}'^T(1) + \left(\frac{l_m{}^2}{3L^2} + \frac{h_m{}^2}{12L^2}\right)\tilde{\boldsymbol{\varphi}}'(1)\tilde{\boldsymbol{\varphi}}'^T(1)\Bigg\}\end{aligned} \quad (55)$$

$$\tilde{\mathbf{K}} = \int_0^1 \tilde{w}(\tilde{x})\tilde{\boldsymbol{\varphi}}''(\tilde{x})\tilde{\boldsymbol{\varphi}}''(\tilde{x})^T d\tilde{x} \quad (56)$$

$$\tilde{\boldsymbol{\Theta}} = \int_0^1 \tilde{w}(\tilde{x})\tilde{\boldsymbol{\varphi}}''(\tilde{x})d\tilde{x} \quad (57)$$

$$\tilde{\mathbf{u}} = \int_0^1 \tilde{w}(\tilde{x})\tilde{\boldsymbol{\varphi}}(\tilde{x})d\tilde{x} + \alpha\left\{\tilde{\boldsymbol{\varphi}}(1) + \frac{l_m}{2L}\tilde{\boldsymbol{\varphi}}'(1)\right\} \quad (58)$$

By further defining some constants, we can remove almost all dimensionality from the equations. This constant $\hat{c}$ characterizes the coupling between the mechanical and electrical elements of the beam system. The smaller its value, the more the mechanics are affected by the electronics:

$$\hat{c} = \frac{d}{C_b V s^E{}_p}\left(t_s + t_p\right)w_+ \frac{y_+}{L}. \quad (59)$$

This constant γ scales the base excitation to the dimensionless scale. It is in units of seconds-squared per meter:

$$\gamma = \frac{{t_0}^2}{y_+}. \tag{60}$$

The resulting differential equations have time derivatives with respect to the dimensionless time defined in Equation (51):

$$\tilde{\mathbf{M}}\ddot{\tilde{\mathbf{q}}} + \tilde{\mathbf{C}}\dot{\tilde{\mathbf{q}}} + \tilde{\mathbf{K}}\tilde{\mathbf{q}} - \tilde{\mathbf{\Theta}}\tilde{E} = \gamma\,\tilde{\mathbf{u}}a\left(\tilde{t}\right) \tag{61}$$

$$\dot{\tilde{V}} + \frac{t_0}{C_p R}\tilde{V} = -\hat{c}\tilde{\mathbf{\Theta}}^T\dot{\tilde{\mathbf{q}}}. \tag{62}$$

They retain the same form, except they are scaled by the input and output constants.

5.2 Strain Distribution as Function of Beam Shape

The different shapes of the beams affect the strain distribution along the length direction. This is the main motivation for these varying cross-section beams to be studied, because the electric field is proportional to strain over the section, it can be increased by careful beam shape design (and power, which is a function of electric field squared). Bending strain is proportional to the curvature of the beam; that is the second spatial derivative of the displacement function, $y(x, t)$. Thus, electric field production is most fruitful when the slope of the beam is monotonic. This occurs only in the first mode of vibration, where the curvature never changes sign. In other work [18] researchers have looked into alternative electrode geometries that can operate in higher modes without electrical cancellation. This, however, is beyond the scope of the current study.

Figure 5.4a shows the first 3 mode shapes for the three tested beams and Figure 5.4b shows the second derivative of the first mode shape for the three beams. Each beam's mode shape resembles the others' mode shapes, but the effect of the shape change is apparent in the second derivative. The tapered beam has a flatter curvature profile than the other two beams, with the reverse-tapered beam's curvature is more biased toward the base. Also note the different lengths of the three beams, as the lengths were selected so that the beams' resonance was at the chosen excitation frequency.

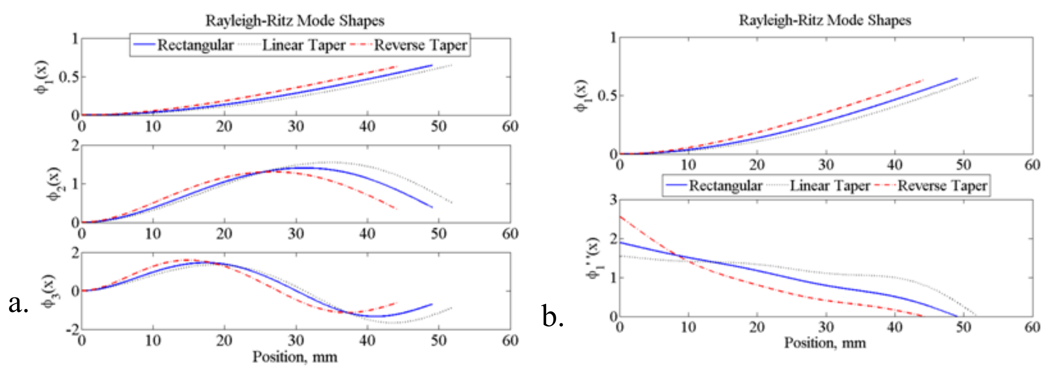

Figure 5.4 - a. Three Fundamental mode shapes of the three beams. b. First mode of the three beams and its second derivative.

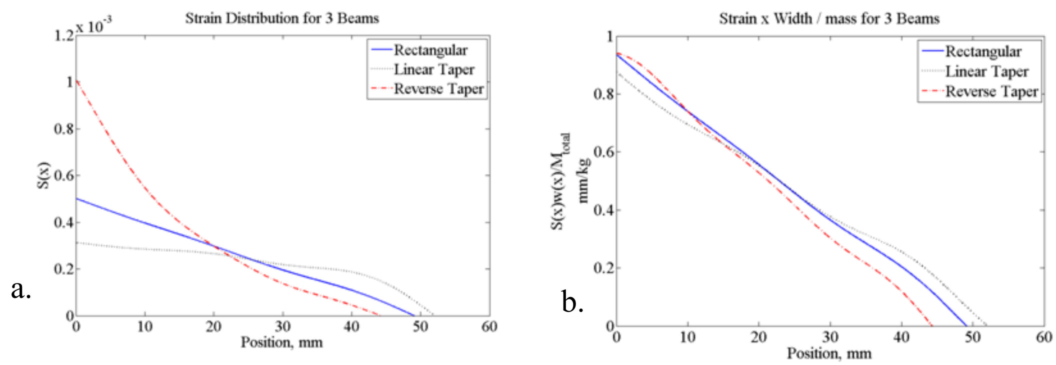

Figure 5.5 - a. Strain in the 3 beams as a function of x position. b. Strain times width as a function of the x position.

The strain of each beam (on the outer surface) can be computed by regarding strain as an output from the dynamic equations. The magnitude of the strain is calculated from the frequency response function of the beam at resonance at each location of interest. Figure 5.5a shows the calculated strain in the beam as a function of position in the *x* direction. All three beams have higher strain at the root than the tip, but the strain distribution of the reverse-tapered beam is skewed much more than the rectangular and tapered beams.

For an effect that applies more to the problem of creating electric field in the piezoceramic, the strain in the beam must be weighted by the width of the section being strained. Figure 5.5b shows this effect. The large strain at the root of the reverse-tapered beam is modulated by its smaller width to produce a similar amount of electric field to the other two beams. The curves are exactly proportional to the amount of electrical energy produced along the length of each beam: the amount of charge carried off the piezo at a point along its length is proportional to the strain there times the width of the section.

5.3 Maximization of Power Output through Shape Change

The next problem is to find an optimal width profile for maximal voltage generation, i.e. to minimize the negative of the average voltage squared:

$$J = -\lim_{T\to\infty}\frac{1}{T}\int_0^T V(t, w(x), L)^2\, dt \tag{63}$$

Other variables are kept constant: shim thickness, piezo thickness, total mass, tip mass, patch configuration, electrode configuration, and total beam area are kept constant. We do allow for a wide variety of beam shapes, however. Beam shapes are defined through the function $\tilde{w}(\tilde{x})$ the width of the beam as a function of position on its length. In this case, the function is a polynomial:

$$\tilde{w}(\tilde{x}) = a_0 + a_1\tilde{x} + a_2\tilde{x}^2 + \ldots \tag{64}$$

The coefficients determine the beam shape. For example, the linearly tapered beam has two terms in this function. It is helpful to limit the number of terms in the polynomial for both computational and mechanical reasons. As the number of terms increases, the computational time increases, but the complexity of the shape increases as well.

In addition to the width profile, the total length of the beam is a variable under investigation in the optimization. With L selected, the constant w_+ is calculated to maintain constant area. A linear constraint is necessary to ensure that the shape has the correct size and has no unrealistic mechanical defects (e.g. zero width, extreme thinness, etc).

Goldschmidtboeing's and Woias's [12] finding that their triangular beam allowed higher excitation amplitude, and therefore was capable of producing more absolute power than the standard rectangular beam is also addressed. Here we introduce a new optimization cost function:

$$J = -\lim_{T\to\infty}\frac{1}{T}\int_0^T V(t, w(x), L, a)^2\, dt \qquad (65)$$

that includes the amplitude of the sinusoidal base excitation $a(t) = a\cos(\omega t)$. With the total mass still constrained, the base excitation is allowed to grow until the root strain reaches a maximum; that is, a new constraint, maximum strain at the root of the beam (where stress concentrations are the greatest), is added.

The optimization is conducted through a constrained MATLAB pattern search algorithm followed by a gradient search to find the local optimum.

Additionally, we perform a study of the effect of the variation of the tip-mass/beam-mass ratio and excitation frequency on the performance of a rectangular beam. This study, more of a parameter space exploration than an optimization, still requires the length of the beam to be optimized so that it would resonate at the given excitation frequency. For this, only the gradient search was required for each combination of given excitation frequency and tip-mass/beam-mass ratio. The terms of (63) were fixed so that the beam remained rectangular.

6. Results

6.1. Shape Optimization at Constant Base Excitation

The first optimization is performed on a beam with a linear profile. Thus only two terms in the polynomial expansion for $\tilde{w}(\tilde{x})$ were nonzero. The pattern search finds a suitable beam with greater power output than the three previously tested beams (Table 5.1). The beam's shape can be seen in Figure 5.6a. With a power output of 0.033354 *watts*, the optimized beam achieves a 0.52% increase in performance over the rectangular beam. Next, we expanded the search to beams with curvature (on a fifth-order polynomial basis). The search algorithm similarly found a shape slightly superior in power output to the rectangular and optimal linear beams (Figure 5.6b). It has no performance increase over the linear beam.

Table 5.1 - Power through the resistor from the three original beams and the optimized beams in simulation.

Beam Shape	Rectangular	Linear Taper	Reverse Taper	Optimal Linear	Optimal Curved
Power (*W*)	0.0331	0.0326	0.0325	0.0334	0.0334

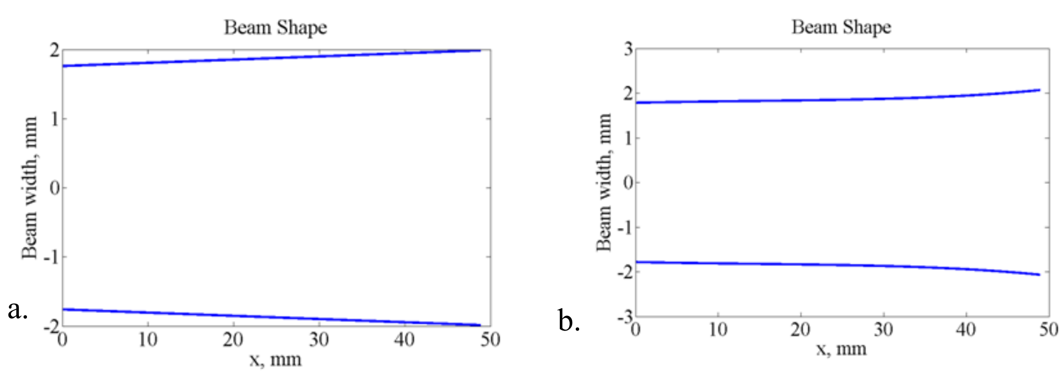

Figure 5.6 - Beam shapes: a. Linear optimal beam. b. Curved optimal beam

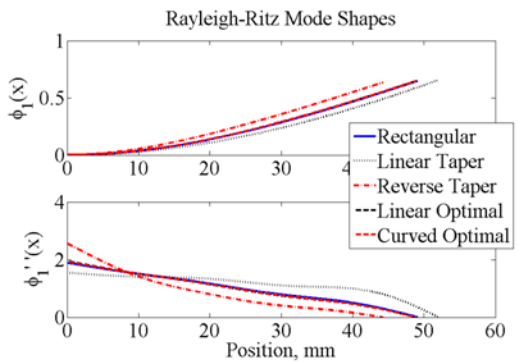

Figure 5.7 - The first mode (above) and second derivative (below) of the first mode for 4 beams.

Figure 5.7 shows the mode shapes for the linear optimal and curved optimal beams. These beams closely match the rectangular beam, except that they are slightly more curved at the root. This is the cause of the increased strain at the root of the beams in Figure 5.8a. Figure 5.8b shows that this increased strain at the root of the beams is not compromised by the decreased width; this explains the increased power output. Additionally, the frequency response of the two optimal beams is not much different from that of the rectangular beam (Figure 5.9). This means that the increased power output has no effect on the bandwidth of the structure, which could possibly have been compromised.

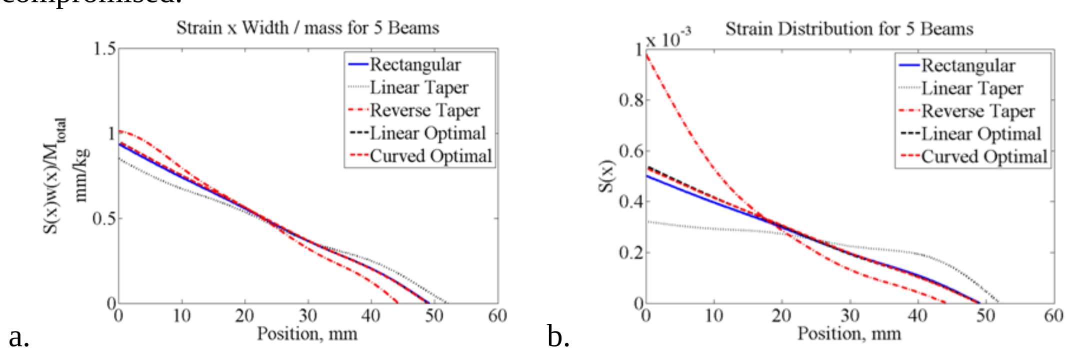

Figure 5.8 - a. The strain distribution in five beams. b. Strain times width for five beams.

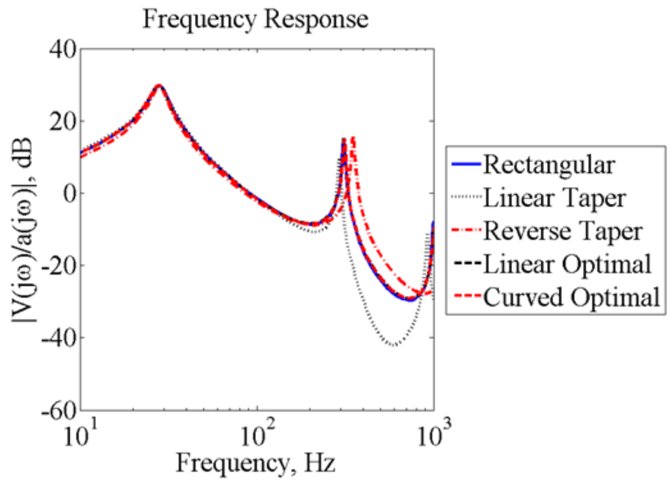

Figure 5.9 - The frequency response of the five beams.

6.2. Shape Optimization with Variable Amplitude Base Excitation

The next issue is whether there is an optimal shape to allow the beam to withstand a maximum base excitation without failing mechanically. A new optimization procedure is used with the power output of the beam still to be maximized but with variable base excitation (66). The resulting beam shape and its frequency response is shown in Figure 5.10. As Goldschmidtboeing and Woias observed [12], the optimal beam has a wider root than tip, but this optimal beam also includes a widening at the tip, perhaps to permit greater bending at that section.

As a mark of comparison, the optimization is run with the shapes of the beams constrained to those of the three tested beams: straight, tapered, and reverse tapered. Their strain and strain by width distributions are shown in Figure 5.11. This shows how the beams compare to the new optimum. Since the magnitude of the output voltage is roughly proportional to the amplitude of the strain times the width, Figure 5.11b shows how the optimized beam outperforms the others. It allows such a greater base excitation that it achieves a greater area under the strain times width curve and produces the most voltage and power.

This result is also invertible; with a given power requirement and base excitation, the mass of the optimal beam is lower than that of the equivalent rectangular beam, while not exceeding the maximum allowable strain.

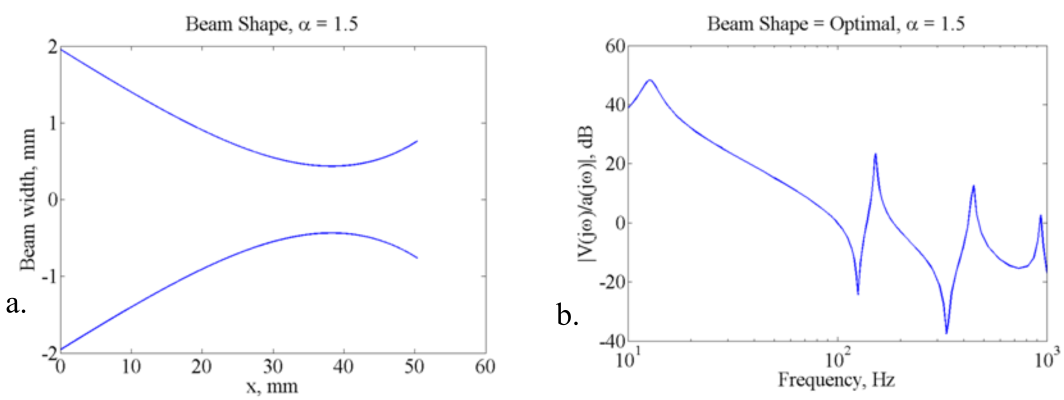

Figure 5.10 - a. The optimal shape for maximal output with varying input amplitude. b. Frequency response of the same beam.

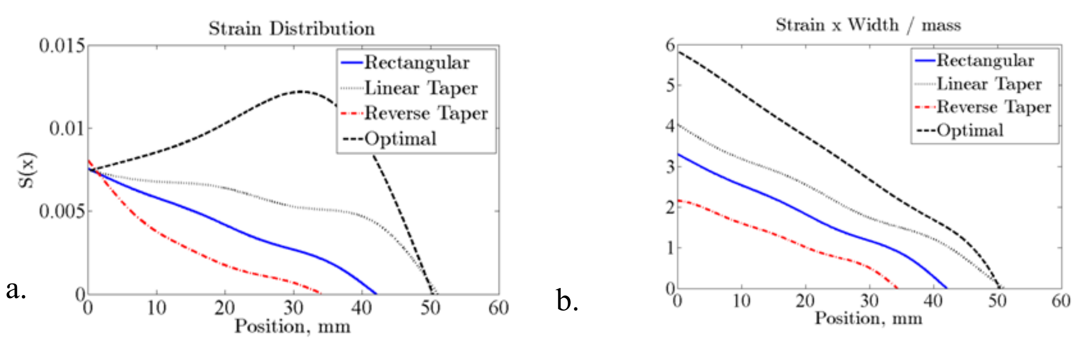

Figure 5.11 - a. Strain distribution for the three original beams with root strain maximized. b. Strain times width distribution for the beams with root strain maximized.

6.3 Tip Mass-to-Beam Mass Ratio Effect

This problem has additional interesting results. As the tip mass is increased, the optimal length of the beam monotonically decreases and approaches an asymptotic value (Figure 5.12a). Similarly, while the power initially decreases as tip mass is increased (albeit by very little), the power begins to increase at a tip-mass/beam-mass ratio of approximately 0.1 (Figure 5.12b). The power approaches a new asymptote approximately 20% higher than the power output with no tip mass.

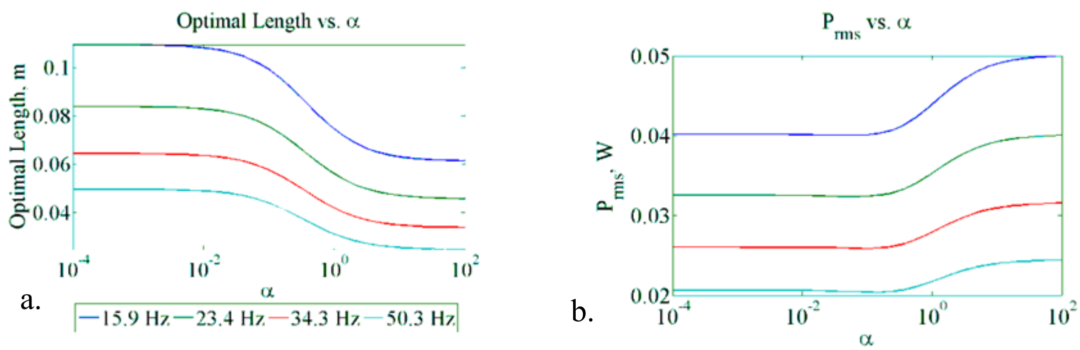

Figure 5.12 - a. The optimal beam length as frequency and tip-mass vary. b. The power output of beams with optimal length as frequency and tip-mass vary.

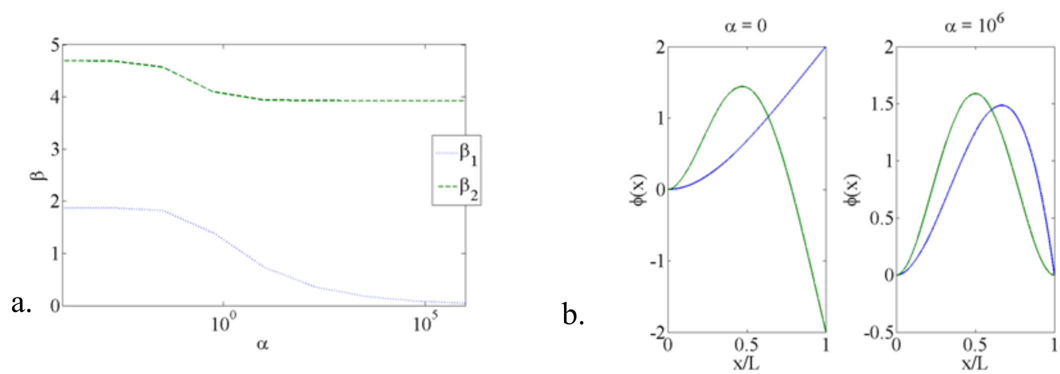

Figure 5.13 - a. Straight-beam eigenvalues as a function of α. b. Eigenfunctions for two cases of α.

This is partially explained by the qualitative change in the beam's behavior as tip mass/beam mass ratio is increased. When α is increased from zero to infinite, the boundary conditions of the beam are effectively changed. A tip mass of zero corresponds to the clamped-free beam, but as the tip mass increases, the end condition begins to resemble a clamped-clamped beam, and the system's eigenvalues reflect this (Figure 5.13). The lowest eigenvalue approaches zero as the tip mass is increased and the first mode is attenuated. The second eigenvalue decreases as well, and this mode becomes the primary mode at extremely high α. This high ratio of α greater than 100, however, is not realistic. In Figure 5.12 the point of diminishing returns occurs around $\alpha = 10$, but the first mode remains active there.

7. Conclusion

Through modeling the vibration of a piezoelectric bimorph, the authors have demonstrated that adjusting the shape of the bimorph can significantly affect piezoelectric transduction. The Euler-Bernoulli/Rayleigh-Ritz model of bending vibration is applied to a series of long, slender beams with tip masses. These beams all exhibit the behavior predicted by the model, accurately matching the first and second modes of vibration. With these results, it can be reasonably assumed that an optimal beam shape can be discovered that produces the maximal voltage output from a given source of base excitation, constrained by mass and piezoelectric geometry (e.g. thickness, maximum length). Additionally, there is perhaps an opportunity to search among configurations where the tip mass-beam mass ratio is variable as well.

Optimal beams are found that improve the power transduction from sinusoidal base excitation to electrical power. This result contributes to the increase in of power output in energy harvesting devices constrained by mass, or to decrease the mass of such devices in power constrained situations.

We have shown that beams with nonuniform width can be manufactured and tested. Although no beams of nonlinear width profile were constructed, we believe these to be within the grasp of current piezoceramic manufacturing technologies and can be an inexpensive method to increase energy harvesting performance.

REFERENCES

[1] Bozkurt, A., Gilmour, R., Sinha, A., Stern, D., Lal A. 2009. "Insect Machine Interface Based Neuro Cybernetics," IEEE Transactions on Biomedical Engineering, 56(6):1727-33.

[2] Reissman, T. and Garcia, E. 2008 "Surgically Implanted Energy Harvesting Devices for Renewable Power Sources in Insect Cyborgs," ASME International Mechanical Engineering Congress and Exposition, October 31 - November 6, Boston, MA. published in: ASME IMECE2008-68136.

[3] Goldfarb, M. and Jones, L. D. 1999. "On the efficiency of electric power generation with piezoelectric ceramic." *ASME Journal of Dynamic Systems, Measurement, and Control*, 121:566–571.

[4] Roundy, S., and Wright, P. K. 2004. "A Piezoelectric Vibration Based Generator for Wireless Electronics," *Smart Materials and Structures* 13:1131-1142.

[5] Liao, Y., and Sodano, H.A. 2008. "Model of a Single Mode energy Harvester and Properties for Optimal Power Generation," *Smart Materials and Structures*, 17:065026(14pp).

[6] Hagood, N. W., Chung, W. H., and von Flotow, A., 1990, "Modeling of Piezoelectric Actuator Dynamics for Active Structural Control," Journal of Intelligent Materials Systems and Structures, 1:327–354.

[7] Sodano, H. A., Park, G., Inman, D. J. 2004. "Estimation of Electric Charge Output for Piezoelectric Energy Harvesting", *Strain*, 40:49-58.

[8] duToit N.E., Wardle, B.L., and Kim, S-G. 2005. "Design Considerations for MEMS-Scale Piezoelectric Mechanical Vibration Energy Harvesters," *Integrated Ferroelectrics*, 71:121-60.

[9] Erturk, A., and Inman, D.J. 2008. "A Distributed Parameter Electromechanical Model for Cantilevered Piezoelectric Energy Harvesters," *Journal of Vibrations and Acoustics*, 130:041002-1 (15pp).

[10] Erturk, A. and Inman, D.J., 2009, An Experimentally Validated Bimorph Cantilever Model for Piezoelectric Energy Harvesting from Base Excitations, Smart Materials and Structures, 18, 025009 (18pp).

[11] Erturk, A., Renno, J.M., and Inman, D.J., 2009, "Modeling of Piezoelectric Energy Harvesting from an L-shaped Beam-Mass Structure with an Application to UAVs," *Journal of Intelligent Material Systems and Structures*, 20, pp. 529-544.

[12] Goldschmidtboeing, F., and Woias, P. 2008. "Characterization of Different Beam Shapes for Piezoelectric Energy Harvesting." *Journal of Micromechanics and Microengineering*. 18:104013 (7pp).

[13] Paquin, S., and St-Amant, Y. 2009. "Electromechanical Performances of Different Shapes of Piezoelectric Energy Harvesters," Proceedings of the Cansmart 2009 International Workshop on Smart Materials and Structures, October 22-23, 2009, Montreal, Quebec, Canada:187-196.

[14] Inman, D.J., 2001. *Engineering Vibration: Second Edition*, Prentice Hall, Upper Saddle River, New Jersey. pp. 458-468.

[15] Crandall, S. H , D C Karnopp, E. F Kurtz, Jr and D C. Pndmore-Brown 1968. *Dynamics of Mechanical and Electromechanical Systems*, Robert E Krieger Publishing Co., Malabar, Florida, pp. 291-326.

[16] Moon, F.C., 1998. *Applied Dynamics With Applications to Multibody and Mechatronic Systems*, John Wiley and Sons, Inc., New York. 401-407.

[17] Rizzoni, G. *Principles and Applications of Electrical Engineering: Fourth Edition*, McGraw Hill, Boston, pp. 360.

[18] Erturk, A., Tarazaga, P.A., Farmer, J.R., and Inman, D.J., 2009, "Effect of Strain Nodes and Electrode Configuration on Piezoelectric Energy Harvesting from Cantilevered Beams," *ASME Journal of Vibration and Acoustics*, 131, 011010 (11pp).

This chapter originally appeared as:

Dietl, J. M., and Garcia, E., "Beam Shape Optimization for Power Harvesting," *Journal of Intelligent Material Systems and Structures*, Vol. 21, April 2010, pp. 633-646.

CHAPTER 6

A TIMOSHENKO BEAM MODEL FOR CANTILEVERED PIEZOELECTRIC ENERGY HARVESTERS[1]

1. Abstract

Piezoelectric bimorph cantilevered beams are often used as energy harvesting devices. These devices are desired for, among other applications, remote sensing and animal tracking due to their potential to eliminate the need for battery replacement. Existing models of piezoelectric bimorph cantilevered beams have proved to describe the dynamics of slender beams at high frequencies accurately. In this paper, a Timoshenko model of transverse piezoelectric beam vibration is developed to address these limitations. Exact expressions for the voltage, current, power, and tip-deflection of the piezoelectric beam are derived. Subsequently, several case studies are presented that examine the frequency response of vibration-based energy harvesters using this model. It is shown that the predicted responses converge towards previously derived Euler-Bernoulli beam models under certain limiting conditions. The Timoshenko model shows that the Euler-Bernoulli model severely over-predicts the tip displacement and consequently the power transduction of a cantilevered piezoelectric bimorph at low length-to-width aspect ratios.

---

[1] From Dietl, J. M., Wickenheiser, A. M., and Garcia. E. "A Timoshenko Beam Model for Cantilevered Piezoelectric Energy Harvesters," *Smart Materials and Structures*, 19, 2010, 055018 (12pp); Reprinted with permission of Institute of Physics, Inc. (http://iopscience.org/sms) © 2010 IOP Publishing Ltd.

2. Introduction

The recent increase in the demand for wireless devices coupled with the decrease in their power requirements has precipitated an explosion in research and development of practical means to provide sufficient energy to meet their application needs. Due to their relatively low energy densities, on-board batteries may be impractical for certain small-scale applications [1, 2]. For distributed sensor networks with a large number of nodes, batteries may be infeasible due to the cost of replacement. A means of making these systems entirely self-sufficient through energy replenishment from their local surroundings may be the key to the proliferation of wireless technology into new environments.

Vibration-based energy harvesting – the conversion of ambient vibrations into useful electrical energy – has received significant attention due to the ubiquity of untapped vibrational energy available in or around most manmade systems[3]. The attention drawn towards this under-utilized energy source has spurred research on several methods of electromechanical transduction [4], including electromagnetic induction (e.g. [5]), electrostatic varactance (e.g. [6]), and the piezoelectric effect (e.g. [7]), the latter being the focus of this study. Although the power harvested is generally small compared to the power required to operate sensors and RF communications continuously, several researchers have demonstrated that, through careful energy budgeting, piezoelectric energy harvesting can provide a viable design solution for maintenance-free, wireless electronics. For example, Kymissis *et al.* [8] have investigated energy harvesting from walking and designed power management circuitry for intermittent RFID transmission. Self-powered, wireless sensors have also been produced for temperature and humidity measurement [9] and machinery acceleration monitoring [10].

The typical piezoelectric energy harvester geometry consists of a cantilevered beam with one or two layers (unimorph or bimorph, respectively) or discrete patches of active material bonded to an inactive substructure. This inherently distributed, infinite-degree-of-freedom (DOF) structure has been successfully modeled as a system with a single mechanical DOF for analysis as part of an energy harvesting circuit [11, 12]. These model reductions are generally quite accurate because the generators are designed to operate near one of its natural frequencies (typically the fundamental frequency) where only one mode is dominant and where there is a local maximum in power harvested [13, 14]. Indeed, these simple models are nevertheless able to predict the electromechanical interaction between the vibrating structure and the circuit to which it is attached. To wit, the shift in natural frequency and the added effective damping due to energy harvesting have been verified experimentally in steady-state [13, 15, 16] and during transient charging of a storage capacitor [17]. Further simplifications have been employed when the electromechanical coupling is weak: in that case, the vibrating mechanical structure may be replaced by an equivalent AC voltage or current source [18] since the mechanical dynamics are virtually unaffected by the electronics [12, 13]. Although the parameters of these simplified models may be identified experimentally (e.g. the method prescribed by [12]), this approach neither offers any insight into the salient physical parameters nor any means of predicting the performance of a candidate design.

Significant effort has been devoted to distributed-parameter modeling of composite piezoelectric structures using Euler-Bernoulli beam theory and modal analysis. These models are generally derived using one of two methodologies: force and moment balance [19, 20, 14] and energy methods [21-23]. These models may be employed to predict the mode shapes and strain distribution in the structure; they also enable the energy harvesting performance to be predicted based on geometry and material properties. These infinite-DOF models may subsequently be truncated to a single mechanical DOF for performance evaluation near a natural frequency [13-15].

The Euler-Bernoulli model of transverse beam vibration is a simplification of a more general beam vibration model derived from a set of first principles. The Euler-Bernoulli model uses a force balance on a differential element in one dimension: shear forces and bending moments are balanced by longitudinal strain in the element and planar transverse vibration. The Timoshenko model of beam vibration includes all the effects of the Euler-Bernoulli model, but also allows for the effect of transverse shear strain (in addition to longitudinal or axial strain) and rotary inertia (in addition to planar inertia). By neglecting the effects of rotary inertia and shear deformation, the Euler-Bernoulli model has been shown to over-predict the natural frequencies of prismatic beams. The additional effects of rotary inertia and shear strain become increasingly important as the beam's cross sectional dimensions are increased relative to the its length. This is apparent at higher modes of vibration when the modal wavelength becomes a fraction of the beam's total length, while the cross sectional dimensions remain constant [24]

In this paper, the electromechanical equations of motion (EOMs) are derived for a piezoelectric energy harvester in transverse and rotational vibrations using Timoshenko beam theory. The beam is assumed to be excited by small (not necessarily sinusoidal) transverse motion of the base. Although only a bimorph configuration is derived herein, the EOMs are couched in terms of effective system parameters whereby only these terms need modification for other configurations (e.g. unimorph or discrete patches). This model can subsequently be solved for the general response of the beam motion and the voltage and current output. An eigenfunction solution procedure is then outlined to produce EOMs for the modal responses to general base excitation.

Subsequently, the case of harmonic base excitation with the energy harvester attached to a resistive load is presented. In this situation, the electromechanical system is linear and, thus, transfer functions are derived between the base motion and the beam response, output voltage, current, and power dissipated by the resistor. The frequency response of the system is analyzed over the full range of resistor values, including short- and open-circuit conditions. The impacts of mechanical damping and electromechanical coupling on the power harvesting performance are discussed in detail. Additionally, a case study is performed to highlight the discrepancies between the present Timoshenko model and previous models based on Euler-Bernoulli beam theory.

3. Electromechanical System Model

The schematic diagram of the piezoelectric, vibration-based energy harvester considered in this study is presented in Figure 6.1. It is a bimorph configuration consisting of a piezoelectric material layer bonded to both surfaces of a supporting, inactive core. Electrodes are assumed to cover the upper and lower surfaces of each layer, and they are wired together in a parallel configuration, as depicted. In this configuration, the voltage across each layer is assumed to be equal, and the charge displaced by each layer is additive. Because each layer experiences opposite strains (i.e. one layer is in tension while the other is in compression), they must be poled in the same direction to avoid charge cancellation. It is assumed that the electrodes and connecting wires have negligible resistance and that the resistivity of the piezoelectric material is significantly higher than that of the external circuitry (i.e. an insulator).

In the following sections, the EOMs for the electromechanical system presented in Figure 6.1 are derived through force, moment, and charge balances adopting the Timoshenko beam assumptions. Subsequently, a solution consisting of a series of assumed modes is presented, and the EOMs are decoupled into modal dynamics equations. The solutions to these equations give the exact response of the energy harvesting system.

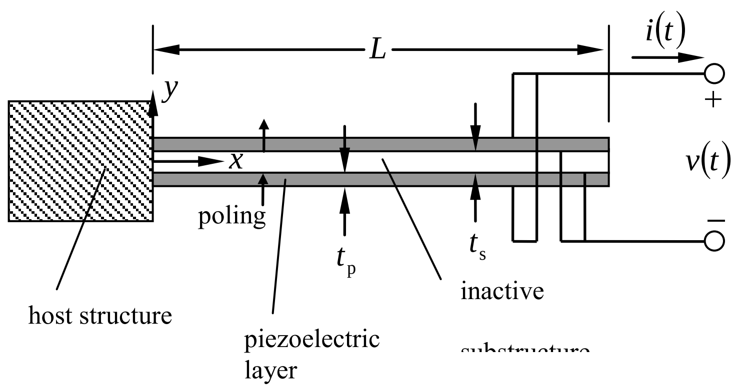

Figure 6.1 - Layout and geometric parameters of cantilevered vibration energy harvester in parallel bimorph configuration

3.1. Derivation of the Electromechanical EOMs.

In the following derivation, the states of the electromechanical system are the following: $w(x,t)$ is the relative transverse deflection of the beam with respect to its base, $\psi(x,t)$ is the rotation angle of the beam cross section, $v(t)$ is the voltage across the energy harvester as seen by the external circuit, and $i(t)$ is the net current flowing through the harvester. The motion, $y(t)$, is the absolute transverse displacement of the base; therefore, $w(x,t)+y(t)$ is the absolute transverse deflection of the beam.

Since it is assumed that both mechanical and electrical perturbations are small, the following linearized constitutive equations for the piezoelectric material are adopted:

$$\begin{aligned} T_1 &= c_{11}^{\mathrm{E}} S_1 - e_{31} E_3 \\ T_5 &= c_{55}^{\mathrm{E}} S_5 \\ D_1 &= e_{31} S_1 + \varepsilon_{33}^{\mathrm{S}} E_3 \end{aligned} \tag{1}$$

where T is stress, S is strain, E is electric field, D is electric displacement, c is Young's Modulus, e is piezoelectric coupling coefficient, and ε is dielectric constant. The subscripts indicate the direction of perturbation; in the cantilever configuration shown in Figure 6.1, 1 corresponds to x, 3 corresponds to y, and 5 corresponds to xy [25]. (Thus, T_5 and S_5 represent shear stress and strain in the xy plane, respectively, and c_{55}^{E} is the shear modulus.) The superscript $(\cdot)^{\mathrm{E}}$ indicates a linearization at constant electric field, and the superscript $(\cdot)^{\mathrm{S}}$ indicates a linearization at constant strain. It is assumed that all piezoelectric material has uniform material properties appearing in (1) as well as uniform density ρ_p. For the inactive substructure, the constitutive equations are

$$\begin{aligned} T_1 &= c_{11,\mathrm{s}} S_1 \\ T_5 &= c_{55,\mathrm{s}} S_5 \end{aligned} \tag{2}$$

where the subscript $(\cdot)_{\cdot,\mathrm{s}}$ indicates a material property of the substructure. It is assumed that all substructure material has uniform material properties appearing in (2) as well as uniform density ρ_{s}.

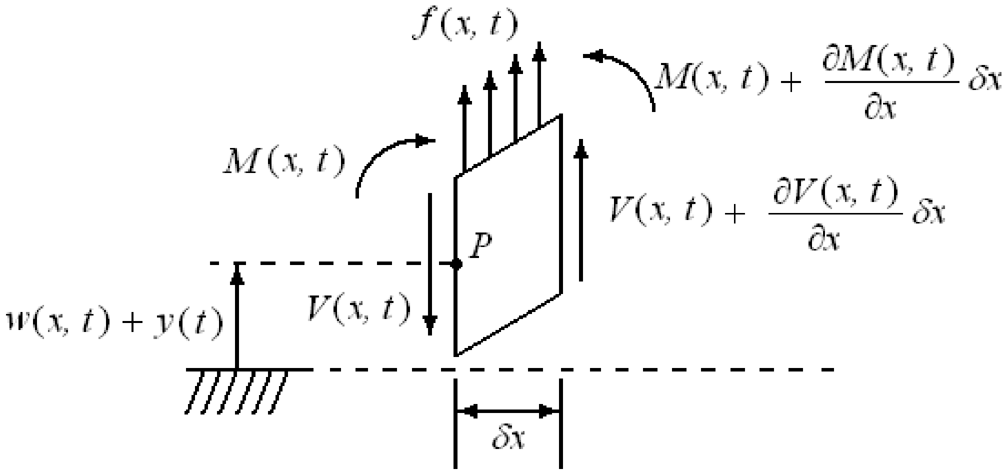

Figure 6.2 - Free body diagram of a differential slice of the piezoelectric beam.

The strain and electric field terms in (1)–(2) must be related to the states of the system. The axial strain is given by $S_1 = y\,\partial\psi/\partial x$ and the shear strain by $S_5 = \psi - \partial w/\partial x$, where the shear angle is simply the difference between the rotation of the cross section and the slope of the beam deflection. The electric field can be written in terms of the voltage across the energy harvester by $E_3 = \chi(y)v$, where

$$\chi(y) = \begin{cases} -1/t_\mathrm{p}\,, & t_\mathrm{s}/2 \le y \le t_\mathrm{s}/2 + t_\mathrm{p} \\ 0, & -t_\mathrm{s}/2 < y < t_\mathrm{s}/2 \\ 1/t_\mathrm{p}\,, & -t_\mathrm{s}/2 - t_\mathrm{p} \le y \le t_\mathrm{s}/2 \end{cases} \tag{3}$$

Thus, it is assumed that the electric field is uniform across the thickness of the piezoelectric layers, and the opposite signs in the top and bottom layers reflect the wiring configuration shown in Figure 6.1.

A balance of forces on a cross-sectional element (Figure 6.2) of the beam with length δx gives:

$$\left(\rho_{\mathrm{s}}t_{\mathrm{s}}+2\rho_{\mathrm{p}}t_{\mathrm{p}}\right)b\delta x\left[\frac{\partial^2 w(x,t)}{\partial t^2}+\frac{\mathrm{d}^2 y(t)}{\mathrm{d}t^2}\right]=-V(x,t)+\left[V(x,t)+\frac{\partial V(x,t)}{\partial x}\delta x\right] \tag{4}$$

where $V(x,t)$ is the internal shear force on the element and b is the width (in the z-direction) of the beam. The shear force is the integral of the shear stress over the cross section A and is given by

$$\begin{aligned} V(x,t) &= -\iint_A T_5 \mathrm{d}A \\ &= -\kappa^2 b\left\{\int_{-t_{\mathrm{s}}/2}^{t_{\mathrm{s}}/2} c_{55,\mathrm{s}}\left[\psi(x,t)-\frac{\partial w(x,t)}{\partial x}\right]\mathrm{d}y+\int_{-t_{\mathrm{s}}/2-t_{\mathrm{p}}}^{-t_{\mathrm{s}}/2} c_{55}^{\mathrm{E}}\left[\psi(x,t)-\frac{\partial w(x,t)}{\partial x}\right]\mathrm{d}y\right. \\ &\quad \left.+\int_{t_{\mathrm{s}}/2}^{t_{\mathrm{s}}/2+t_{\mathrm{p}}} c_{55}^{\mathrm{E}}\left[\psi(x,t)-\frac{\partial w(x,t)}{\partial x}\right]\mathrm{d}y\right\} \\ &= -\kappa^2 b\left(c_{55,\mathrm{s}}t_{\mathrm{s}}+2c_{55}^{\mathrm{E}}t_{\mathrm{p}}\right)\left[\psi(x,t)-\frac{\partial w(x,t)}{\partial x}\right] \end{aligned} \tag{5}$$

Here, the integral of the stress along the thickness of the beam is scaled by a correction term κ^2 to account for the fact that the stress is not uniform across the cross section but depends on its geometry [26]. (For a rectangular cross section, this correction factor takes on the values $0.833 \le \kappa^2 \le 0.870$, depending on the Poisson ratio of the material.) To state the force balance in terms of state variables, we can combine (5) and (4), yielding

$$\begin{aligned} \left(\rho_{\mathrm{s}}t_{\mathrm{s}}+2\rho_{\mathrm{p}}t_{\mathrm{p}}\right)b\frac{\partial^2 w(x,t)}{\partial t^2}+\kappa^2 b\left(c_{55,\mathrm{s}}t_{\mathrm{s}}+2c_{55}^{\mathrm{E}}t_{\mathrm{p}}\right)\left[\frac{\partial\psi(x,t)}{\partial x}-\frac{\partial^2 w(x,t)}{\partial x^2}\right] \\ = -\left(\rho_{\mathrm{s}}t_{\mathrm{s}}+2\rho_{\mathrm{p}}t_{\mathrm{p}}\right)b\frac{\mathrm{d}^2 y(t)}{\mathrm{d}t^2} \end{aligned} \tag{6}$$

Equation (6) can be written more compactly as

$$\hat{m}\frac{\partial^2 w(x,t)}{\partial t^2}+\kappa^2(AG)_{\mathrm{eff}}\left[\frac{\partial\psi(x,t)}{\partial x}-\frac{\partial^2 w(x,t)}{\partial x^2}\right]=-\hat{m}\frac{\mathrm{d}^2 y(t)}{\mathrm{d}t^2} \tag{7}$$

where $\hat{m} = (\rho_{\mathrm{s}} t_{\mathrm{s}} + 2\rho_{\mathrm{p}} t_{\mathrm{p}})b$ is the mass per unit length, and $(AG)_{\mathrm{eff}} = b(c_{55,\mathrm{s}} t_{\mathrm{s}} + 2c_{55}^{\mathrm{E}} t_{\mathrm{p}})$ is the effective shear stiffness. Equation (7) constitutes the first EOM for this electromechanical system.

A balance of moments (around point *P* in Figure 6.2) on a cross-sectional element of the beam with length δx gives:

$$\iiint_{A\delta x} \rho y^2 \mathrm{d}A\mathrm{d}x \frac{\partial^2 \psi(x,t)}{\partial t^2} = \left[M(x,t) + \frac{\partial M(x,t)}{\partial x}\delta x \right] - M(x,t) + \left[V(x,t) + \frac{\partial V(x,t)}{\partial x}\delta x \right]\delta x - \hat{m}\frac{\mathrm{d}^2 y(t)}{\mathrm{d}t^2}\frac{\delta x^2}{2} \tag{8}$$

where $M(x,t)$ is the internal moment on the element. Neglecting terms of order δx^2 reduces (8) to

$$\iiint_{A\delta x} \rho y^2 \mathrm{d}A\mathrm{d}x \frac{\partial^2 \psi(x,t)}{\partial t^2} = \frac{\partial M(x,t)}{\partial x}\delta x + V(x,t)\delta x \tag{9}$$

Evaluating the mass moment of inertia term on the left-hand side yields

$$\iiint_{A\delta x} \rho y^2 dAdx = \rho_{\mathrm{s}} b\delta x \int_{-t_{\mathrm{s}}/2}^{t_{\mathrm{s}}/2} y^2 \mathrm{d}y + \rho_{\mathrm{p}} b\delta x \int_{-t_{\mathrm{s}}/2-t_{\mathrm{p}}}^{-t_{\mathrm{s}}/2} y^2 \mathrm{d}y + \rho_{\mathrm{p}} b\delta x \int_{t_{\mathrm{s}}/2}^{t_{\mathrm{s}}/2+t_{\mathrm{p}}} y^2 \mathrm{d}y = (\rho I)_{\mathrm{eff}}\,\delta x \tag{10}$$

where $(\rho I)_{\mathrm{eff}} = \rho_{\mathrm{s}} b \dfrac{t_{\mathrm{s}}^3}{12} + 2\rho_{\mathrm{p}} b \left[\dfrac{t_{\mathrm{p}}^3}{12} + t_{\mathrm{p}} \left(\dfrac{t_{\mathrm{p}} + t_{\mathrm{s}}}{2} \right)^2 \right]$ is the effective rotary inertia.

The internal moment is the integral of the first moment of the axial stress over the cross section *A* and is given by

$$
\begin{aligned}
M(x,t) &= -\iint_A T_1 y \mathrm{d}A \\
&= -b\left\{\int_{-t_\mathrm{s}/2}^{t_\mathrm{s}/2} - c_{11,\mathrm{s}} y^2 \frac{\partial \psi(x,t)}{\partial x} \mathrm{d}y + \int_{-t_\mathrm{s}/2-t_\mathrm{p}}^{-t_\mathrm{s}/2} \left[- c_{11}^{\mathrm{E}} y^2 \frac{\partial \psi(x,t)}{\partial x} - e_{31} y \chi(y) v(t)\right] \mathrm{d}y \right. \\
&\quad \left. + \int_{t_\mathrm{s}/2}^{t_\mathrm{s}/2+t_\mathrm{p}} \left[- c_{11}^{\mathrm{E}} y^2 \frac{\partial \psi(x,t)}{\partial x} - e_{31} y \chi(y) v(t)\right] \mathrm{d}y \right\} \\
&= (EI)_{\mathrm{eff}} \frac{\partial \psi(x,t)}{\partial x} + \vartheta v(t)\left[H(x) - H(x-L)\right]
\end{aligned} \tag{11}
$$

where $(EI)_{\mathrm{eff}} = c_{11,\mathrm{s}} b \dfrac{t_\mathrm{s}^3}{12} + 2c_{11}^{\mathrm{E}} b \left[\dfrac{t_\mathrm{p}^3}{12} + t_\mathrm{p}\left(\dfrac{t_\mathrm{p}+t_\mathrm{s}}{2}\right)^2\right]$ is the effective transverse stiffness, $\vartheta = -e_{31} b (t_\mathrm{s} + t_\mathrm{p})$ is the electromechanical coupling coefficient, and $H(\cdot)$ is the Heaviside step function. We can rewrite the moment balance in terms of the voltage, axial displacement, and shear displacement by substituting (5), (10), and (11) into (9), yielding

$$
(\rho I)_{\mathrm{eff}} \frac{\partial^2 \psi(x,t)}{\partial t^2} = (EI)_{\mathrm{eff}} \frac{\partial^2 \psi(x,t)}{\partial x^2} + \vartheta v(t)\left[\delta(x) - \delta(x-L)\right] + \kappa^2 (AG)_{\mathrm{eff}} \left[\frac{\partial w(x,t)}{\partial x} - \psi(x,t)\right] \tag{12}
$$

where $\delta(\cdot)$ is the Dirac delta function. Equation (12) constitutes the second EOM for this electromechanical system.

Finally, the net charge displaced by the electric field in the piezoelectric material $q(t)$ is given by the integral of the electric displacement over the electrode area [25]:

$$
\begin{aligned}
q(t) &= \iint_{\mathrm{upper}} D_3 \mathrm{d}A - \iint_{\mathrm{lower}} D_3 \mathrm{d}A \\
&= b\int_0^L \left[- e_{31} \frac{1}{t_\mathrm{p}} \int_{t_\mathrm{s}/2}^{t_\mathrm{s}/2+t_\mathrm{p}} y \mathrm{d}y \frac{\partial \psi(x,t)}{\partial x} + \varepsilon_{33}^{\mathrm{S}} \frac{-1}{t_\mathrm{p}} v(t) \right] \mathrm{d}x \\
&\quad - b\int_0^L \left[- e_{31} \frac{1}{t_\mathrm{p}} \int_{-t_\mathrm{s}/2-t_\mathrm{p}}^{-t_\mathrm{s}/2} y \mathrm{d}y \frac{\partial \psi(x,t)}{\partial x} + \varepsilon_{33}^{\mathrm{S}} \frac{1}{t_\mathrm{p}} v(t) \right] \mathrm{d}x \\
&= \vartheta \psi(L,t) - C_0 v(t)
\end{aligned} \tag{13}
$$

where $C_0 = 2\varepsilon_{33}^{\mathrm{S}} bL / t_{\mathrm{p}}$ is the net clamped (i.e. constant strain) capacitance of the piezoelectric material. In the integration in the *y*-direction, the average transverse strain is used to calculate the electrical displacement at *x*. Equation (13) constitutes the third EOM for this electromechanical system.

In summary, the coupled EOMs for the piezoelectric energy harvester are given by

$$\hat{m}\frac{\partial^2 w(x,t)}{\partial t^2} + \kappa^2 (AG)_{\mathrm{eff}} \left[\frac{\partial \psi(x,t)}{\partial x} - \frac{\partial^2 w(x,t)}{\partial x^2}\right] = -\hat{m}\frac{\mathrm{d}^2 y(t)}{\mathrm{d}t^2} \tag{14a}$$

$$(\rho I)_{\mathrm{eff}} \frac{\partial^2 \psi(x,t)}{\partial t^2} = (EI)_{\mathrm{eff}} \frac{\partial^2 \psi(x,t)}{\partial x^2} + \vartheta v(t)[\delta(x) - \delta(x-L)] + \kappa^2 (AG)_{\mathrm{eff}} \left[\frac{\partial w(x,t)}{\partial x} - \psi(x,t)\right] \tag{14b}$$

$$q(t) = \vartheta \psi(L,t) - C_0 v(t) \tag{14c}$$

The form of (14) is the same for any configuration piezoelectric energy harvester using Timoshenko beam theory – only the coefficients vary. (See [14], for a generalized formulation using Euler-Bernoulli beam theory.) Note that the base excitation only directly contributes to the transverse dynamics of (14a); it does not appear in the rotational dynamics equation (14b). Furthermore, the transverse dynamics are coupled to the rotational dynamics, and the rotational dynamics are coupled to the electrical dynamics, but the electrical dynamics are not directly coupled to the transverse dynamics. This chain of pair-wise coupled equations is in contrast to the Euler-Bernoulli formulation, in which the rotational dynamics equation can be eliminated and the transverse dynamics are directly coupled to the electrical dynamics.

3.2. Modal Analysis

The most common method of solving the system (14) is to assume that the transverse and rotational deflections can be written as a series expansion of eigenfunctions,

$$w(x,t)=\sum_{i=1}^{\infty} L\varphi_i(\xi)r_i(t) \text{ and } \psi(x,t)=\sum_{i=1}^{\infty}\eta_i(\xi)r_i(t) \tag{15}$$

where $\varphi_i(\cdot)$ and $\eta_i(\cdot)$ are the i^{th} transverse and rotational mode shape functions, respectively, and $r_i(t)$ is the i^{th} modal displacement. These eigenfunctions are couched in terms of the dimensionless coordinate $\xi = x/L$ to make them independent of the length of the beam. Since the transverse and rotational dynamics are coupled, each pair of mode shapes (φ_i, η_i) shares a pair of eigenvalues (α_i, β_i) given by [27]

$$\alpha_i^2 = -(A_i + B_i) - \sqrt{(A_i - B_i)^2 + C_i} \text{ and } \beta_i^2 = -(A_i + B_i) + \sqrt{(A_i - B_i)^2 + C_i} \tag{16}$$

$$\text{where } A_i = \frac{(\rho I)_{\text{eff}} L^2 \omega_{\text{SC},i}^2}{2(EI)_{\text{eff}}},\ B_i = \frac{\hat{m}L^2\omega_{\text{SC},i}^2}{2\kappa^2(AG)_{\text{eff}}},\text{ and } C_i = \frac{\hat{m}L^4\omega_{\text{SC},i}^2}{(EI)_{\text{eff}}}$$

Here, $\omega_{\text{SC},i}^2$ is i^{th} modal short-circuit (i.e. $v(t)=0$) natural frequency. Note that for Euler-Bernoulli beams, $(\rho I)_{\text{eff}} \to 0$ and $(AG)_{\text{eff}} \to \infty$, and so

$$\alpha_i^2, \beta_i^2 \to \lambda_i^2 = \sqrt{\frac{\hat{m}L^4\omega_{\text{SC},i}^2}{(EI)_{\text{eff}}}} \tag{17}$$

It is clear that $\alpha_i^2 < 0$; however, the sign of β_i^2 is determined by the physical parameters of the system, i.e. from (16)

$$\beta_i^2 > 0 \Leftrightarrow \frac{\kappa^2(AG)_{\text{eff}}}{(\rho I)_{\text{eff}}\,\omega_{\text{SC},i}^2} > 1 \tag{18}$$

Note that (18) is always true for Euler-Bernoulli beams. Thus, there are three classes of mode shapes and corresponding eigenvalues depending on the sign of β_i^2 [28]. Implementing the boundary conditions of the cantilevered beam yields the following:

Case $\beta_i^2 > 0$:

$$\varphi_i(\xi) = \cos\alpha_i\xi - \cosh\beta_i\xi + \frac{\sin\alpha_i - \dfrac{\alpha_i}{\beta_i}\sinh\beta_i}{\cos\alpha_i + \dfrac{\alpha_i^2 - 2B_i}{2B_i + \beta_i^2}\cosh\beta_i}\left[\sin\alpha_i\xi + \frac{\beta(2B_i - \alpha_i^2)}{\alpha(2B_i + \beta_i^2)}\sinh\beta_i\xi\right] \quad (19)$$

$$\begin{aligned}\eta_i(\xi) = {} & \frac{2B_i - \alpha_i^2}{\alpha_i}\sin\alpha\xi - \frac{\beta_i^2 + 2B_i}{\beta_i}\sinh\beta_i\xi \\ & + \frac{\alpha_i^2 - 2B_i}{\alpha_i}\,\frac{\sin\alpha_i - \dfrac{\alpha_i}{\beta_i}\sinh\beta_i}{\cos\alpha_i + \dfrac{\alpha_i^2 - 2B_i}{2B_i + \beta_i^2}\cosh\beta_i}\left(\cos\alpha_i\xi - \cosh\beta_i\xi\right)\end{aligned} \quad (20)$$

where the eigenvalues are solutions to

$$0 = 2 + \left(\frac{\alpha^2 - 2B}{\beta^2 + 2B} + \frac{\beta^2 + 2B}{\alpha^2 - 2B}\right)\cos\alpha\cosh\beta + \left(\frac{\beta}{\alpha} - \frac{\alpha}{\beta}\right)\sin\alpha\sinh\beta \quad (21)$$

Case $\beta_i^2 = 0$:

$$\varphi_i(\xi) = \cos\alpha_i\xi - 1 + \frac{\sin\alpha_i - \alpha_i}{\cos\alpha_i + \dfrac{\alpha_i^2 - 2B_i}{2B_i}}\sin\alpha_i\xi \quad (22)$$

$$\eta_i(\xi) = \frac{2B_i - \alpha_i^2}{\alpha_i}\sin\alpha\xi - 2B_i\xi + \frac{\alpha_i^2 - 2B_i}{\alpha_i}\,\frac{\sin\alpha_i - \alpha_i}{\cos\alpha_i + \dfrac{\alpha_i^2 - 2B_i}{2B_i}}\left(\cos\alpha_i\xi - 1\right) \quad (23)$$

where the eigenvalues are solutions to

$$0=2+\left(\frac{\alpha^2-2B}{2B}+\frac{2B}{\alpha^2-2B}\right)\cos\alpha-\alpha\sin\alpha \tag{24}$$

Case $\beta_i^2<0$:

$$\varphi_i(\xi)=\cos\alpha_i\xi-\cos\beta_i\xi+\frac{\sin\alpha_i-\dfrac{\alpha_i}{\beta_i}\sin\beta_i}{\cos\alpha_i+\dfrac{\alpha_i^2-2B_i}{2B_i-\beta_i^2}\cos\beta_i}\left[\sin\alpha_i\xi+\frac{\beta\left(2B_i-\alpha_i^2\right)}{\alpha\left(\beta_i^2-2B_i\right)}\sin\beta_i\xi\right] \tag{25}$$

$$\eta_i(\xi)=\frac{2B_i-\alpha_i^2}{\alpha_i}\sin\alpha\xi+\frac{\beta_i^2-2B_i}{\beta_i}\sin\beta_i\xi+\frac{\alpha_i^2-2B_i}{\alpha_i}\frac{\sin\alpha_i-\dfrac{\alpha_i}{\beta_i}\sin\beta_i}{\cos\alpha_i+\dfrac{\alpha_i^2-2B_i}{2B_i-\beta_i^2}\cos\beta_i}\left[\cos\alpha_i\xi-\cos\beta_i\xi\right] \tag{26}$$

where the eigenvalues are solutions to

$$0=2+\left(\frac{2B-\alpha^2}{\beta^2-2B}+\frac{\beta^2-2B}{2B-\alpha^2}\right)\cos\alpha\cos\beta+\left(\frac{\beta}{\alpha}+\frac{\alpha}{\beta}\right)\sin\alpha\sin\beta \tag{27}$$

Note that (19) and (21) reduce to

$$\varphi_i(\xi)=\cos\lambda_i\xi-\cosh\lambda_i\xi+\frac{\sin\lambda_i-\sinh\lambda_i}{\cos\lambda_i+\cosh\lambda_i}\left(\sin\lambda_i\xi-\sinh\lambda_i\xi\right) \tag{28}$$

$$0=2+2\cos\lambda\cosh\lambda \tag{29}$$

respectively, for Euler-Bernoulli beams.

The mode shapes given above may be scaled arbitrarily and still be admissible and are done so in the present case to satisfy the orthogonality condition [29]:

$$\int_0^1\left[\hat{m}L^2\varphi_s(\xi)\varphi_r(\xi)+(\rho I)_{\text{eff}}\,\eta_s(\xi)\eta_r(\xi)\right]\mathrm{d}\xi=\delta_{rs} \tag{30}$$

where δ_{rs} is the Kronecker delta. In order to extract a single dynamics equation for each mode from the coupled transverse and rotational EOMs (14a-b), the following steps are taken: substitute (15) into (14a-b), multiply (14a) by $\varphi_k(\xi)$, multiply (14b) by $\eta_k(\xi)$, add the two resulting equations together, and integrate in ξ from 0 to *1*. The orthogonality condition (30) eliminates all but one term in (15), resulting in

$$\frac{d^2 r_k(t)}{dt^2} + \omega_{\mathrm{SC},k}^2 r_k(t) + \frac{\Theta_k}{L} v(t) = -\hat{m}\gamma_k \frac{\mathrm{d}^2 y(t)}{\mathrm{d}t^2} \tag{31}$$

for all k, where Θ_k is the modal electromechanical coupling coefficient, and γ_k is the modal influence coefficient of the base excitation. These coefficients are given by

$$\Theta_k = \theta\eta_k(1), \quad \gamma_k = \int_0^1 L\varphi_k(\xi)\mathrm{d}\xi \tag{32}$$

At this point, it is common to add in a modal damping term $2\zeta_k\omega_{\mathrm{SC},k}\,\mathrm{d}r_k(t)/\mathrm{d}t$ to the left-hand side of Equation (31) to account for all proportional damping effects, such as viscous and Kelvin-Voight damping as discussed by Banks and Inman [30]. The electrical EOM (14c) can be written in terms of modal coordinates by substituting (15) into (14c), yielding

$$q(t) = \sum_{i=1}^{\infty} \Theta_i r_i(t) - C_0 v(t) \tag{33}$$

which, together with (31), provides a complete system of modal equations for the vibration energy harvester for an arbitrary, twice-differentiable base excitation $y(t)$.

3.3. Axial Strain and Shear Strain Energy

Also of interest is the potential energy stored in the strain of the beam's structure. In Euler-Bernoulli beam models, the axial (or longitudinal normal) strain accounts for all of the mechanical potential energy. (Electrical potential energy is contained in the electric field of the piezoelectric material, which is identical in both electromechanical models). The axial strain energy is defined by the integral of stress times strain throughout the volume of the beam:

$$U_{\mathrm{A}} = \frac{1}{2}\iiint_{V} S_1 T_1 \mathrm{d}V \tag{34}$$

which with application of the analysis from section 2.1, can be simplified to

$$U_{\mathrm{A}}(t) = \frac{1}{2}\int_0^L \left\{ (EI)_{\mathrm{eff}} \left[\frac{\partial \psi(x,t)}{\partial x} \right]^2 + \vartheta v(t) \frac{\partial \psi(x,t)}{\partial x} \right\} \mathrm{d}x \tag{35}$$

and with the modal analysis from section 2.2, further simplified to

$$U_{\mathrm{A}}(t) = \frac{1}{2}\int_0^1 \left\{ \frac{(EI)_{\mathrm{eff}}}{L} \left[\sum_{i=1}^{\infty} \frac{\mathrm{d}\eta_i(\xi)}{\mathrm{d}\xi} r_i(t) \right]^2 + \vartheta v(t) \left[\sum_{i=1}^{\infty} \frac{\mathrm{d}\eta_i(\xi)}{\mathrm{d}\xi} r_i(t) \right] \right\} \mathrm{d}\xi \tag{36}$$

Similarly, the shear strain energy can be computed:

$$U_{\mathrm{S}} = \frac{1}{2}\iiint_{V} S_5 T_5 \mathrm{d}V \tag{37}$$

which can be simplified to

$$U_{\mathrm{S}} = \frac{1}{2}\int_0^L \kappa^2 (AG)_{\mathrm{eff}} \left[\psi(x,t) - \frac{\partial w(x,t)}{\partial x} \right]^2 \mathrm{d}x \tag{38}$$

and with modal analysis from section 2.2, further simplified to

$$U_{\mathrm{S}} = \frac{1}{2}\int_0^1 \kappa^2 (AG)_{\mathrm{eff}}\, L \left[\sum_{i=1}^{\infty} \eta_i(\xi) r_i(t) - L \frac{\mathrm{d}\varphi(\xi)}{\mathrm{d}\xi} r_i(t) \right]^2 \mathrm{d}\xi \tag{39}$$

Eqations. (36) and (39) can be used in conjunction with the steady-state response in the following section to calculate the frequency response of the axial strain and shear strain energies.

4. Steady-State Response to Harmonic Base Excitation

Now the applications of the above electromechanical model for energy harvesting are examined. In a prototypical energy harvesting system, the cantilevered beam is subjected to base excitations in a wide band. In this section, the special case of harmonic base excitation is considered, i.e. $y(t)=Y\mathrm{e}^{\mathrm{j}\omega t}$, where Y is the amplitude of the base motion (assumed real), and ω is the driving frequency. (Note that the phase angle of the base motion is assumed to be 0 for convenience.) Additionally, the electrical load attached to the energy harvester is assumed to be represented by a simple resistor with resistance R. (This impedance R can be real or complex.) For the real case, (33) can be written as

$$\frac{\mathrm{d}v(t)}{\mathrm{d}t}+\frac{1}{RC_0}v(t)=\frac{1}{C_0}\sum_{i=1}^{\infty}\Theta_i r_i(t) \tag{40}$$

Since the system of equations (31,40) (with modal damping) is linear, the output voltage and modal responses are also harmonic at the driving frequency. Thus, $v(t)=V\mathrm{e}^{\mathrm{j}\omega t}$ and $r_k(t)=R_k\mathrm{e}^{\mathrm{j}\omega t}$, for all k, where V and R_k are complex. Substituting these expressions into (31) and solving for modal magnitude R_k gives

$$R_k=\frac{\hat{m}\gamma_k\omega^2 Y-\dfrac{\Theta_k}{L}V}{\omega_{\mathrm{SC},k}^2-\omega^2+\mathrm{j}2\zeta_k\omega_{\mathrm{SC},k}\omega} \tag{41}$$

which may be regarded as a second-order response with an external input due to the base excitation and a feedback term from the voltage dynamics. A second equation relating the mechanical and electrical responses can be found from (40). Again, assuming a harmonic response yields

$$V\left(\mathrm{j}\omega+\frac{1}{RC_0}\right)=\frac{1}{C_0}\sum_{i=1}^{\infty}\Theta_i\,\mathrm{j}\omega R_i \tag{42}$$

In order to solve for R_k and V explicitly, the following definitions can be utilized

$$S_1=\sum_{i=1}^{\infty}\frac{j\hat{m}\omega^3\gamma_i\Theta_i Y}{\omega_{\mathrm{SC},i}^2-\omega^2+\mathrm{j}2\zeta_i\omega_{\mathrm{SC},i}\omega}\ \text{ and }\ S_2=\sum_{i=1}^{\infty}\frac{\mathrm{j}\omega\Theta_i^2}{\omega_{\mathrm{SC},i}^2-\omega^2+\mathrm{j}2\zeta_i\omega_{\mathrm{SC},i}\omega} \tag{43}$$

to solve (41-42), giving the modal response

$$R_k=\frac{\hat{m}\gamma_k\omega^2 Y+\dfrac{\dfrac{\Theta_k\omega^2}{C_0 L}S_1}{\mathrm{j}\omega+\dfrac{1}{RC_0}+\dfrac{S_2}{C_0 L}}}{\omega_{\mathrm{SC},k}^2-\omega^2+\mathrm{j}2\zeta_k\omega_{\mathrm{SC},k}\omega} \tag{44}$$

$$V=\frac{-\dfrac{\omega^2}{C_0}S_1}{\mathrm{j}\omega+\dfrac{1}{RC_0}+\dfrac{S_2}{C_0 L}} \tag{45}$$

If, for example, the driving frequency is close to k^{th} natural frequency (i.e. $\omega\approx\omega_{\mathrm{SC},k}$), then it is reasonable to assume that $R_l\approx 0,\ l\neq k$. Consequently, (43) reduces to

$$S_1=\frac{j\hat{m}\omega^3\gamma_k\Theta_k Y}{\omega_{\mathrm{SC},k}^2-\omega^2+\mathrm{j}2\zeta_k\omega_{\mathrm{SC},k}\omega}\ \text{ and }\ S_2=\frac{\mathrm{j}\omega\Theta_k^2}{\omega_{\mathrm{SC},k}^2-\omega^2+\mathrm{j}2\zeta_k\omega_{\mathrm{SC},k}\omega} \tag{46}$$

It is worth mentioning that if the electromechanical coupling is strong, then the natural frequencies of the system vary with load resistance R, and consequently the one-mode assumption may only be accurate in a small neighborhood in the (ω, R)-plane [14].

5. Parametric Study of Bimorph Timoshenko Beam Response

Here the response of a cantilevered bimorph energy harvester in response to transverse base excitation with the Timoshenko model is analyzed (Figure 6.1). The beam's physical properties are given in table 1. Its electrodes are assumed to coat both the top and bottom of the piezoelectric layers evenly to assure a constantly distributed electric field within the dielectric. Each mode has a unique damping ratio. (The damping ratios are calculated from the equation:

$$\zeta_k = \frac{c_{\mathrm{V}}}{2\omega_{\mathrm{SC},k}} + \frac{c_{\mathrm{S}}}{2}\omega_{\mathrm{SC},k} \tag{47}$$

where c_{V} and c_{S} are constant viscous damping and strain damping terms respectively. It is noted that if strain damping dominates, then the damping ratio increases as the natural frequencies increase. See Table 1.) The beam is excited harmonically by shaking the host structure transversally. Frequencies of excitation range from below the first harmonic mode to above the third resonant mode.

These harmonic excitations will be analyzed for varying resistive loads, since electromechanical coupling is of interest. The resonant frequencies of each mode of the beam change as the resistive load is varied from 0 (a short circuit) to infinite (an open circuit). Furthermore, there will be an analysis of potential energy storage in both the axial deformation (or longitudinal normal deformation) and shear deformation, to illustrate the necessity of considering shear deformation for sufficiently stubby beams.

Table 6.1 - Physical properties of the piezoelectric bimorph.

Beam length, L	50 *mm*
Width, b	20 *mm*
Substrate thickness, t_s	0.5 *mm*
Piezo thickness, t_p	0.4 *mm*
1-stiffness of substrate, c_{1s}	100 *GPa*
5-stiffness of substrate, c_{5s}	40 *GPa*
1-stiffness of piezo, c_{1p}	66 *GPa*
5-stiffness of piezo, c_{5p}	21 *GPa*
Substrate density, ρ_s	7165 kg/m^3
Piezo density, ρ_p	7800 kg/m^3
Piezoelectric constant, d_{31}	-190 *nm/V*
Permittivity, ε_{33}	15.93 *nF/m*
Poisson's Ratio, ν	0.3
Damping Ratio (first mode), ζ_1	0.0086
Damping Ratio (second mode), ζ_2	0.016
Damping Ratio (third mode), ζ_3	0.043

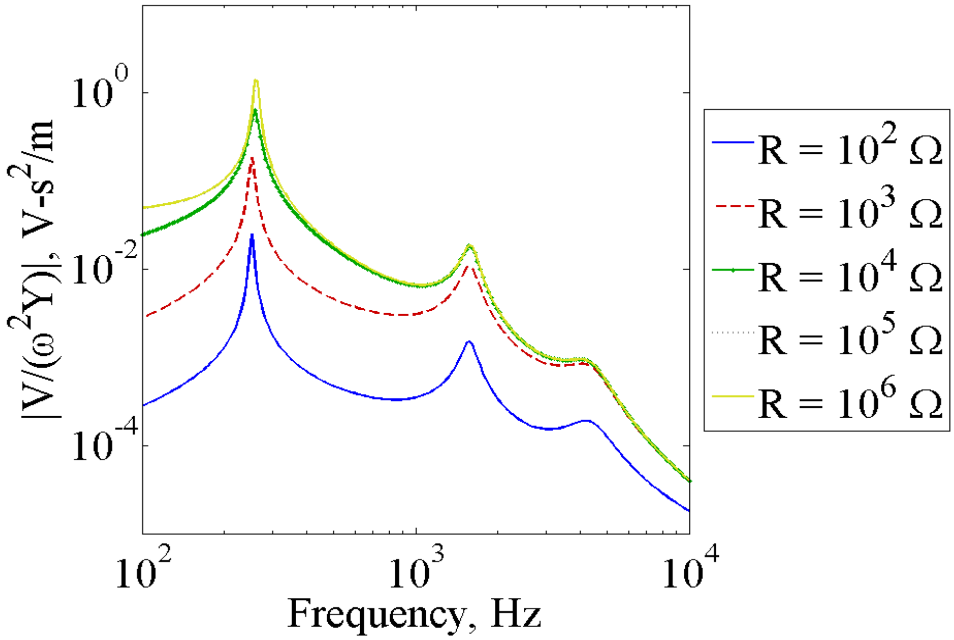

Figure 6.3 - The voltage frequency response to base excitation. (inset) A close-up of the first resonant peak.

5.1. Voltage Frequency Response

The beam's frequency response, as described in (45), is shown in Figure 6.3. This frequency response is defined as the magnitude of the ratio of the voltage on the piezoelectric elements to the acceleration of the host structure. It is noted that there are three natural frequencies present in this frequency range, with the lowest frequency corresponding to the greatest magnitude and the highest corresponding to the lowest magnitude. Additionally, the apparent damping of the modes decreases as the frequency increases, (which was designed into the simulation).

For increasing resistance, the amount of voltage developed across the piezoelectric layers increases. This is because the voltage on the piezo is proportional to its charge. At lower resistances, the beam has a shorter electrical time constant, allowing more charge to drain from the piezoelectric elements during each cycle. At the higher resistances (or at open circuit), the beam achieves its maximum voltage. This maximum voltage occurs at the various open circuit resonant frequencies. At short circuit, the voltage on the piezo is necessarily zero.

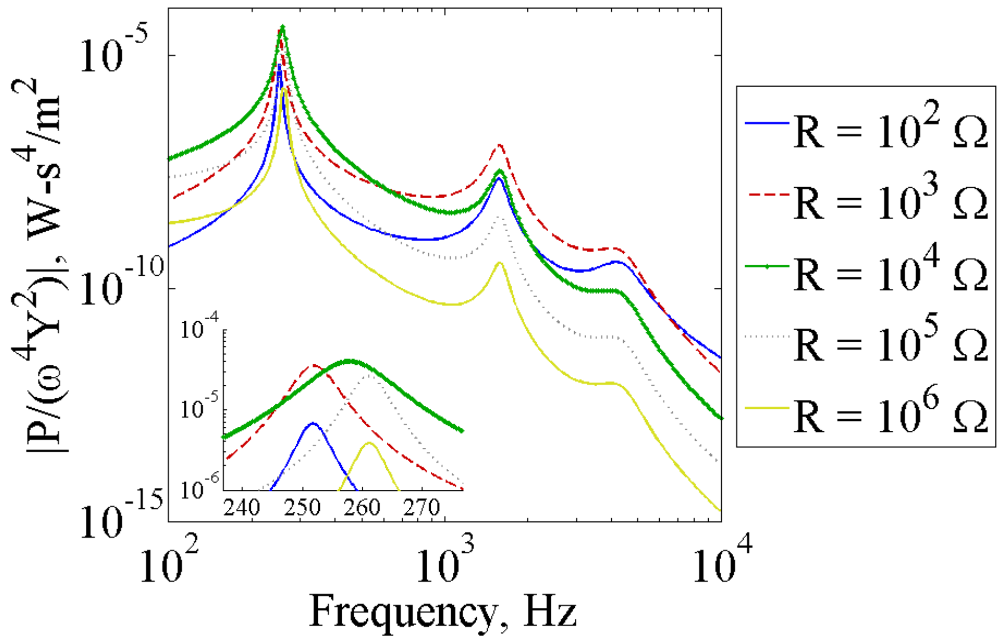

Figure 6.4 - The power frequency response to base excitation. (inset) A close-up of the first resonant peak.

5.2. Power Frequency Response

The beam's power frequency response (Figure 6.4) is the ratio of the magnitude of the power output of the beam to the base acceleration squared; it is the voltage frequency response times the current frequency response, or equivalently the voltage squared divided by the load resistance (45):

$$P = \frac{V^2}{R} \tag{48}$$

It is zero when the voltage is zero (short circuit), and it is zero when the current is zero (open circuit). It achieves a maximum between those extremes of resistances, and this maximum occurs between the open circuit resonant frequency and the short circuit resonant frequency.

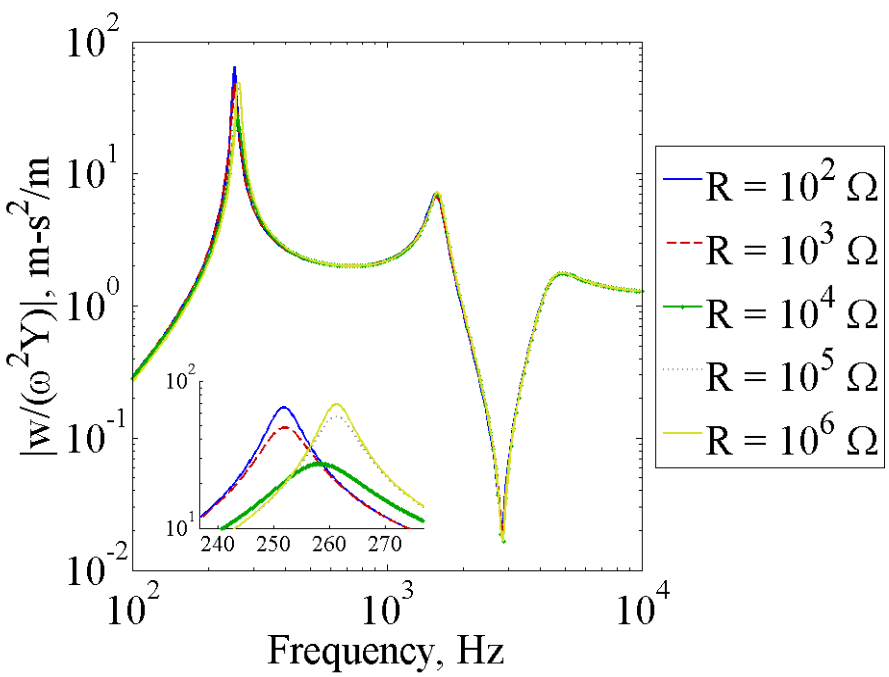

Figure 6.5 - The tip deflection response to base excitation. . (inset) A close-up of the first resonant peak.

As the resistance is increased from zero the resonant frequency of the first mode increases monotonically from the short circuit resonant frequency and approaches the open circuit resonant frequency. During this increase, the first mode's resonant peak increases in magnitude until it reaches a peak value. Further increases in the load resistance cause the magnitude of the first mode to decrease. This happens likewise in the higher modes, except that the peak occurs at different load resistances.

5.3. Tip Deflection Frequency Response

Tip deflection frequency response (Figure 6.5) is the ratio of the magnitude of the tip deflection (15) to the host structure acceleration. This response is also a function of the resistance across the piezoelectric electrodes. When power is dissipated from the beam through the resistive load, less potential energy remains in the beam strain. Thus, at both the short-circuit and open-circuit conditions the deflection achieves a local maximum. The short-circuit and open-circuit conditions can be considered uncoupled conditions because the dynamics of the beam vibration lose a dynamic state, that of the electric field in the piezoelectric. Thus the equations of motion are one order lower.

There is a local minimum resonant peak of the tip deflection between the short-circuit and the open circuit resonances. This is a condition of maximum coupling between the mechanical and electrical elements of the piezoelectric energy harvester.

6. Comparison of Timoshenko Beam to Euler-Bernoulli Beam

The Timoshenko beam model produces a different response from the Euler-Bernoulli beam model, a disparity that is more pronounced at lower beam lengths and at higher modes of vibration. To study this effect, the tip deflection, voltage output, current output, and power output shall be reexamined and compared with results obtained by the Euler-Bernoulli model. The following simulations are carried out at a constant resistance of $R = 10\ k\Omega$. At this value, the beams show a significant coupling effect, and the differences between the Timoshenko model and Euler-Bernoulli model are well pronounced. (For this purpose, the effect of varying the load resistance is ignored. Instead, a constant load resistance is chosen to be great enough to distinguish this system from a non-electromechanically coupled prismatic beam). Four beams have been selected for illustration and noted in table 2.

Table 6.2 - Sizes of four beams.

Beam Number	Length (mm)	Width (mm)	A_{R}
1	6.00	167	0.166
2	15.3	65.2	2.77
3	39.1	25.5	46.1
4	100	10	769

To normalize the voltage and power outputs of the beams by mass, each has the same projected area but a different length and width. Using the length, width, and thickness of the beams, and aspect ratio is defined: $A_{\mathrm{R}} = \dfrac{L^2}{b(2t_{\mathrm{p}} + t_{\mathrm{s}})}$. This, however, is related to the quantities in (18): $\beta_i^2 > 0 \Leftrightarrow \dfrac{\kappa^2 (AG)_{\mathrm{eff}}}{(\rho I)_{\mathrm{eff}}\, \omega_{\mathrm{SC},i}^2} > 1$, in that by increasing L the natural frequency decreases. (The width b has no effect on the ratio of AG to ρI.) The use of this aspect ratio is an alternative to using the quantity in (18) directly, which depends on the natural frequencies which cannot be calculated a priori.

6.1. Tip Deflection Frequency Response

Timoshenko's model was originally developed to account for the effects of shear strain and rotational inertia in short transversally vibrating beams without electromechanical coupling. Thus, of first interest is how the Timoshenko model compares to the Euler-Bernoulli model in tip deflection. Figure 6.6 shows the tip deflection for the four beams. Each beam's frequency response is calculated for both models and the results for each model are plotted on the same axis for each beam.

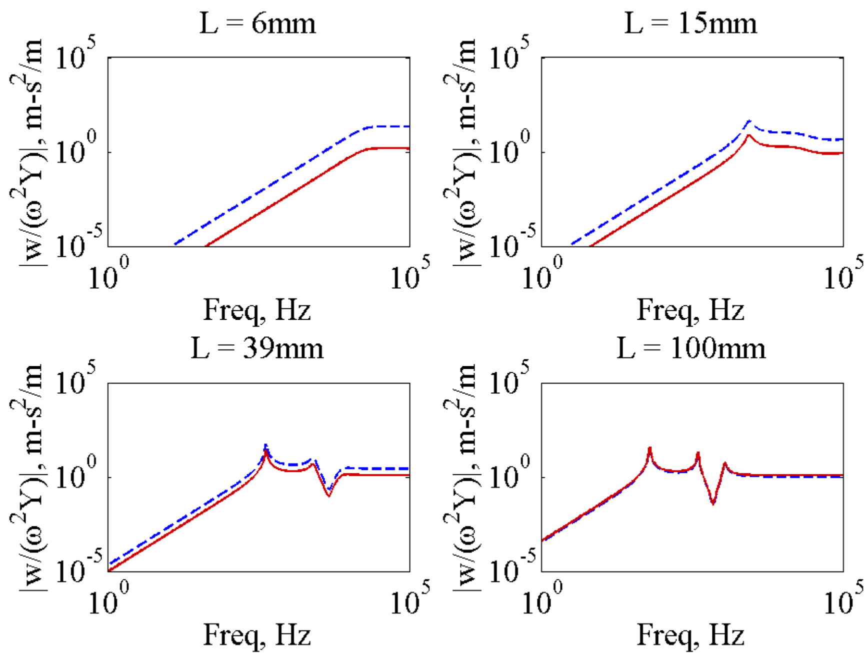

Figure 6.6 - The tip deflection response to base excitation. Euler-Bernoulli – –, Timoshenko —

The shortest beam (in the upper left-hand corner) shows the greatest difference between the Euler-Bernoulli (dashed line) and the Timoshenko (solid line) models. At all of the observed frequencies, the Euler-Bernoulli model predicts a vastly greater tip deflection response than the Timoshenko by a full order of magnitude. Both models predict the same curve shape however, with a small peak. At shorter beam lengths (not shown) the resonant peak disappears entirely.

The remaining beams show the two models converging as the beam length increases. In the lower right graph, the longest studied beam, the amplitude of the two models' resonances is nearly identical. In fact, the Timoshenko model predicts a higher peak than the Euler-Bernoulli model at this length.

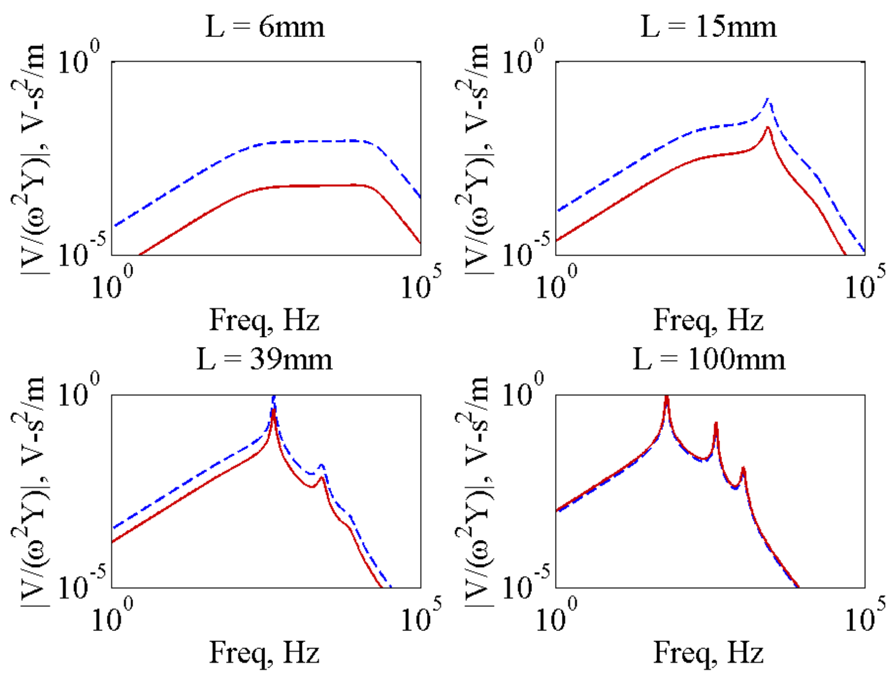

Figure 6.7 - The voltage response to base excitation. Euler-Bernoulli – –, Timoshenko —

6.2. Voltage and Power Frequency Response

The beam's voltage frequency response is directly affected by the beam's deflection response (Figure 6.7). As the beam length increases, the Timoshenko model and Euler-Bernoulli model again converge. In the upper left-hand graph of Figure 6.7, the two models exhibit an order of magnitude discrepancy. As the beam length increases, which can be seen in the other graphs in Figure 6.7, the two models converge. Thus, the Timoshenko model and the Euler-Bernoulli model adequately describe piezoelectric voltage response for slender beams, but there is significant doubt in the Euler-Bernoulli beam model at lower aspect ratios.

The beam's power output, consequently, has similar features. Apropos Figure 6.8, the two beam models converge as the beam lengths converge.

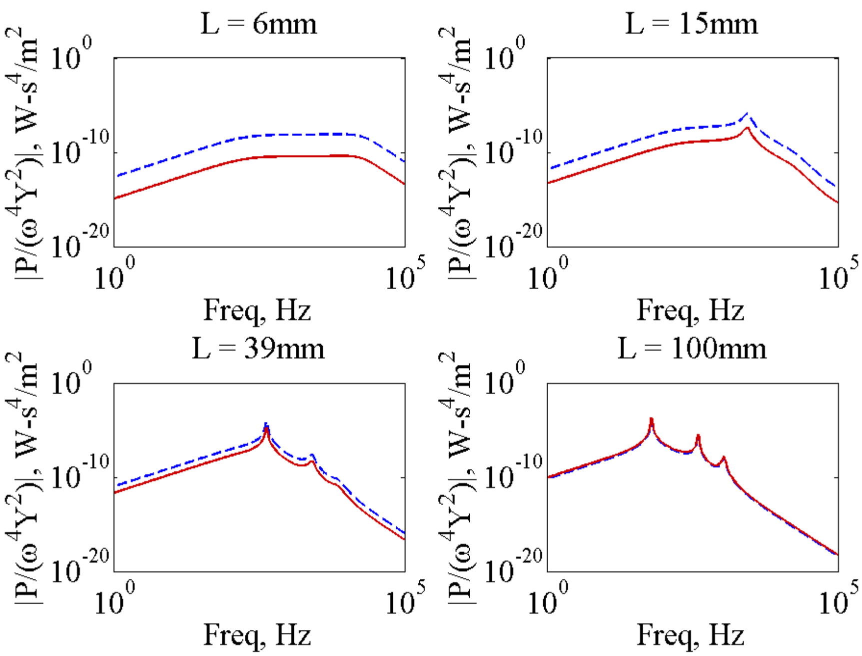

Figure 6.8 - The power response to base excitation. Euler-Bernoulli – –, Timoshenko —

6.3. Axial and Shear Strain Frequency Response

The Timoshenko model accounts for shear strain in addition to axial strain, which is the sole province of the Euler-Bernoulli model. Thus it is fitting to examine the amount of shear and axial strain in the beams predicted in the Timoshenko model. Since the Timoshenko model converges to the Euler-Bernoulli model under certain conditions, then under those conditions the shear energy approaches zero and the bending energy converges to the Euler-Bernoulli prediction.

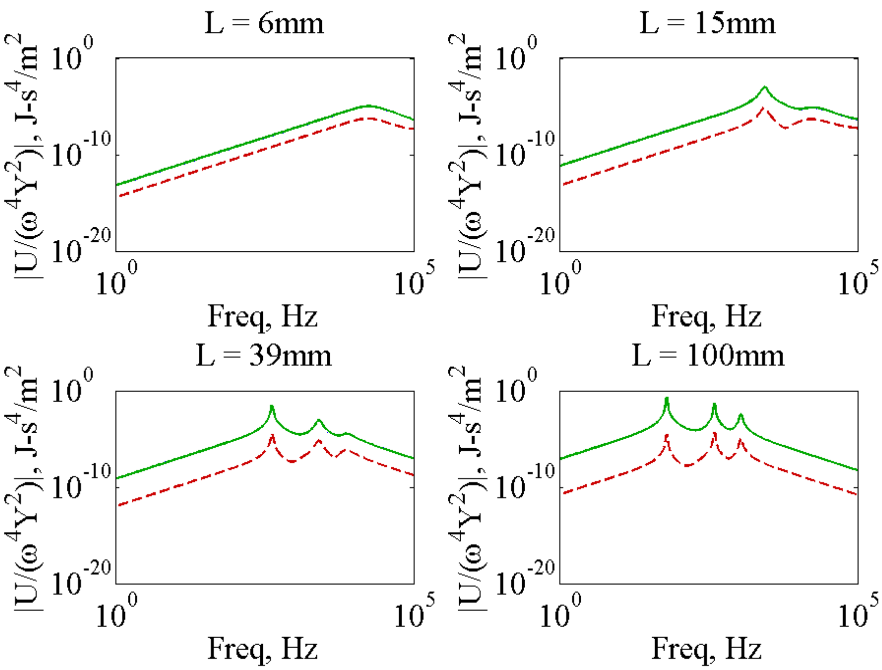

Figure 6.9 - The axial and shear strain energy response to base excitation.
Axial Strain Energy ···, Shear Strain Energy – –, Total Strain Energy —

Figure 6.9 shows a comparison between the magnitude of axial strain energy (36), shear strain energy (39), and the total strain energy in the studied beams. (Since the axial strain energy is typically orders of magnitude greater than the shear strain energy, the axial strain and total strain energy are nearly indistinguishable in Figure 6.9.) It is noted that both the axial and shear strains have the same peaks (in frequency) in all the studied beam lengths. This is more pronounced at longer length-to-width ratios. At the shortest beam length, however, the axial and shear strains exhibit a peculiar shape; especially at higher frequencies, the shear strain energy approaches the axial strain energy.

At those frequencies, it is apparent that shear strain is increasingly important. (Consider, however, that the short beam studied at those frequencies in Figures 6-8 has no interesting resonances in the higher frequencies; in fact, it has no higher resonant frequencies.) Figure 6.10 demonstrates that at shorter beam lengths the shear strain becomes increasingly important in figuring the total strain energy in a transversally vibrating beam. The longest beam, in the lower right-hand corner, has axial strain

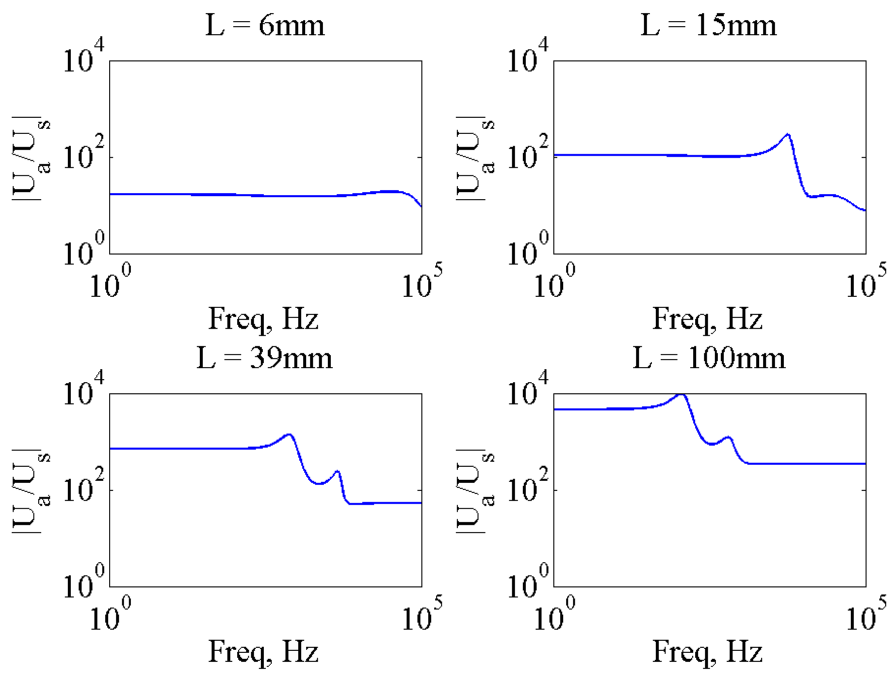

Figure 6.10 - The axial strain energy-shear strain energy ratio response to base excitation.

energy at more than 100 times greater than shear strain energy at the two lowest resonances. The shortest beam, however, has its axial strain energy to shear strain energy ratio approaching unity, especially at higher frequencies.

During the base excitation of a cantilevered piezoelectric bimorph power harvesting system the energy of the base's shaking is transferred to the vibration of the beam, from which energy is transferred through the beam's piezoelectric coupling to the electronic circuitry. As is shown in (1), electrical energy is only generated through strain in the 1-direction, i.e. the axial strain of the beam. Thus, power and voltage output is monotonically related to the axial strain during base excitation. The energy held in the shear strain is energy diverted from energy converted into axial strain energy and electric energy. The significance of this is that beams with high shear strain will necessarily have lower electromechanical coupling. As shown above, this should have the greatest effect on beams with short aspect ratios, higher natural frequencies, and higher excitation frequencies, where the Euler-Bernoulli model will increasingly over-predict the electromechanical coupling.

7. Conclusion

In this paper, an improved model for the electromechanical transduction of a piezoelectric bimorph cantilevered transverse vibrator is developed. This model is based on the assumptions of Timoshenko: that the Euler-Bernoulli assumptions are insufficient for beams vibrated at high frequency or beams of low length squared to cross-section area ratio. Like the Euler-Bernoulli beam vibration model, this model is linear. The electromechanical dynamics are not restricted to harmonic motions, but those dynamics are applied to the general harmonic base excitation. This model is then used to study the behavior of the beam parametrically. The beam's load resistance is swept as the beam's tip deflection, voltage, current, and power are discussed. The Timoshenko beams shows similar behavior to that of the Euler-Bernoulli beam under varying resistance. Since these behaviors are well known, they are little worth discussing. Finally, the Timoshenko model is compared to the Euler-Bernoulli model over several beam sizes, and it is show to diverge from the Euler-Bernoulli model severely at short beam-length squared to cross-section area ratios.

The Euler-Bernoulli model—its lack of accounting for rotational inertia and shear strain—is inadequate at explaining the behavior of such beams. It is also deficient at explaining beam behavior at higher modes of vibration.

REFERENCES

[1] Warneke B, Last M, Liebowitz B and Pister K S J 2001 Smart dust: communicating with a cubic-millimeter computer *Computer* **34**(1) 44–51

[2] Reissman T, Crawford J and Garcia E 2007 Insect cyborgs: a new frontier in flight control systems *Proc. SPIE* **6525** 65250N

[3] Roundy S, Wright P K and Rabaey J 2003 A study of low level vibrations as a power source for wireless sensor nodes *Computer Communications* **26** 1131–44

[4] Beeby S P, Tudor M J and White N M 2006 Energy harvesting vibration sources for microsystems applications *Meas. Sci. Technol.* **13** R175–95

[5] Glynne-Jones P, Tudor M J, Beeby S P and White N M 2004 An electromagnetic, vibration-powered generator for intelligent sensor systems *Sensors Actuators* **110** 344–9

[6] Mitcheson P D, Miao P, Stark B H, Yeatman E M, Holmes A S and Green T C 2004 MEMS electrostatic micro-power generator for low frequency operation *Sensors Actuators* **115** 523–9

[7] Anton S R and Sodano H A 2007 A review of power harvesting using piezoelectric materials (2003–2006) *Smart Mater. Struct.* **16** R1–21

[8] Kymissis J, Kendall C, Paradiso J and Gershenfeld N 1998 Parasitic power harvesting in shoes *Physics and Media Group* MIT Media Laboratory E15-410

[9] Arms S W, Townsend C P, Churchill D L, Galbreath J H and Mundell S W 2005 Power management for energy harvesting wireless sensors *Proc. SPIE* **5763** 267–75

[10] Discenzo F M, Loparo K A, Cassar H and Chung D 2006 Machinery condition monitoring using wireless self-powered sensor nodes *Proc. 24th Int. Modal Analysis Conf.*

[11] Roundy S and Wright P K 2004 A piezoelectric vibration based generator for wireless electronics *Smart. Mater. and Struct.* **13** 1131–42

[12] Lefeuvre E, Badel A, Richard C and Guyomar D 2005 Piezoelectric energy harvesting device optimization by synchronous charge extraction *J. Intell. Mater. Syst. Struct.* **16** 865–76

[13] Shu Y C and Lien I C 2006 Analysis of power output for piezoelectric energy harvesting systems *Smart Mater. and Struct.* **15** 1499–512

[14] Wickenheiser A M and Garcia E 2010 Power optimization of vibration energy harvesters utilizing passive and active circuits *J. Intell. Mater. Syst. Struct.* Published online before print July 5, 2010, doi: 10.1177/1045389X10376678

[15] Liao Y and Sodano H A 2008 Model of a single mode energy harvester and properties for optimal power generation *Smart. Mater. and Struct.* **17** 065026

[16] Erturk A and Inman D J 2009 An experimentally validated bimorph cantilever model for piezoelectric energy harvesting from base excitations *Smart Mater. and Struct.* **18** 025009

[17] Wickenheiser A M, Reissman T, Wu W J and Garcia E 2010 Modeling the effects of electromechanical coupling on energy storage through piezoelectric energy harvesting *IEEE/ASME Trans. Mech.* **15**(3) 400-411.

[18] Wu W J, Wickenheiser A M, Reissman T and Garcia E 2009 Modeling and experimental verification of synchronized discharging techniques for boosting

power harvesting from piezoelectric transducers *Smart Mater. Struct.* **18** 055012

[19] Söderkvist J 1990 Electric equivalent circuit for flexural vibrations in piezoelectric materials *IEEE Trans. Ultra. Ferro. Freq. Control* **27**(6) 577–86

[20] Erturk A and Inman D J 2008 A distributed parameter electromechanical model for cantilevered piezoelectric energy harvesters *J. Vib. Acoustics* **130** 041002

[21] Hagood N W, Chung W H and von Flotow A 1990 Modelling of piezoelectric actuator dynamics for active structural control *J. Intell. Mater. Syst. Struct.* **1** 327–54

[22] Sodano H A, Park G and Inman D J 2004 Estimation of electric charge output for piezoelectric energy harvesting *Strain* **40** 49–58

[23] duToit N E, Wardle B L and Kim S 2005 Design considerations for MEMS-scale piezoelectric mechanical vibration energy harvesters *Integr. Ferroelectr.* **71** 121–60

[24] Timoshanko S, Young D H and Weaver W 1974 *Vibration Problems in Engineering: Fourth Edition*, (New York: John Wiley and Sons), 432-435.

[25] IEEE 1987 *IEEE Standard on Piezoelectricity* (New York: IEEE)

[26] Cowper G R 1966 The shear coefficient in Timoshenko's beam theory *ASME J. Appl. Mech.* **33** 335–40

[27] Huang T C 1961 The effect of rotatory inertia and of shear deformation on the frequency and normal mode equations of uniform beams with simple end conditions *J. Appl. Mech.* **28** 579–84

[28] Salarieh H and Ghorashi M 2006 Free vibration of Timoshenko beam with finite mass rigid tip load and flexural-torsional coupling *Int. J. of Mech. Sci.* **48** 763–79

[29] Reismann H and Pawlik P S 1974 *Elastokinetics: An Introduction to the Dynamics of Elastic Systems* (St. Paul: West Publishing Co.) 420

[30] Banks H T and Inman D J 1991 On damping mechanisms in beams *ASME J. Appl. Mech.* **58** 716–23

This chapter originally appeared as:

Dietl, J. M., Wickenheiser, A. M., and Garcia. E., "A Timoshenko Beam Model for Cantilevered Piezoelectric Energy Harvesters," *Smart Materials and Structures*, Vol. 19, 2010, 055018 (12pp).

CHAPTER 7

SUMMARY

1. Summary and Conclusions

The work presented here is a set of useful additions to the mountain of research in mechanical and aerospace engineering. I predict that these advances will be used by engineers and researchers: the multiple shooting algorithm for detecting ornithopter limit cycles, the discrete-time periodic linear quadratic regulator, the ornithopter optimal control algorithm, the optimal piezoelectric beam design, and the Timoshenko model.

I developed the multiple shooting algorithm for ornithopter limit cycle detection to solve a specific problem in ornithopter flight dynamics: to analyze the stability of flight without any fixed points. Floquet analysis was amenable to this problem, but the difficulty in solving the equations of motion for anything but the simplest dynamical systems prohibits the standard analytical techniques. A numerical method was therefore necessary. In order to apply this to ornithopter flight, it was also necessary to use automatic differentiation to compute the Jacobians of the dynamic equations to compute sufficiently accurate Floquet multipliers. Although this method was specifically used in ornithopter flight, it should be applicable to any periodic systems with complex structure including helicopters, satellites, windmills, and engines.

The discrete-time periodic linear quadratic regulator was also developed to solve a specific problem, to create a controller to stabilize ornithopter flight. This problem required a control law that accounted for the system's time-varying dynamics and a controller with sufficiently high bandwidth to stabilize the highly unstable trajectories. D-PLQR solved both of these problems by having a finite number of control gains, but at a temporal resolution high enough to account for the high frequency unstable modes. This also could find applications in any controllable periodic dynamic systems.

Optimal control of ornithopters does not seem to have much applicability beyond the world of ornithopter flight, but in this field it will be instrumental in designing high speed maneuvers.

The design of piezoelectric energy harvesters has been the focus of intense research for the last decade, and it will probably continue for years. Researchers continue to search for better ways to make self-sufficient systems with lower weight and cost. The optimal piezoelectric bimorph will help engineers to solve these problems.

Finally, the Timoshenko model adds insight to the design of piezoelectric power harvesting and sensor designs. Although it should not have very much use in designing functional energy harvesters—it seems that long slender beams are a better design than the short stubby beams that necessitate a Timoshenko model—it can be used as a reality check on such designs. However, I think that it will find use in the design of high bandwidth piezoelectric sensors, where high precision in predictability is paramount.